THESIS APPROVAL

GRADUATE SCHOOL, KASETSART UNIVERSITY

Doctor of Engineering (Chemical Engineering)
DEGREE

Chemical Engineering   Chemical Engineering
FIELD   **DEPARTMENT**

TITLE: Synthesis of Bimodal Porous Silica from Rice Husk Ash Using Chitosan as
Template and the Application as Catalyst Support for Fischer-Tropsch
Synthesis

NAME: Mr. Thongthai Witoon

THIS THESIS HAS BEEN ACCEPTED BY

_____ **THESIS ADVISOR**

(Associate Professor Metta Chareonpanich, D.Eng.   )

_____ **THESIS CO-ADVISOR**

(Associate Professor Paisan Kongkachuichay, Ph.D.   )

_____ **THESIS CO-ADVISOR**

(Associate Professor Phungphai Phanawadee, D.Sci.   )

_____ **DEPARTMENT HEAD**

(Associate Professor Phungphai Phanawadee, D.Sci.   )

APPROVED BY THE GRADUATE SCHOOL ON _____

_____ **DEAN**

(Associate Professor Gunjana Theeragool, D.Agr.)

THESIS

SYNTHESIS OF BIMODAL POROUS SILICA FROM RICE HUSK ASH USING CHITOSAN AS TEMPLATE AND THE APPLICATION AS CATALYST SUPPORT FOR FISCHER-TROPSCH SYNTHESIS

THONGTHAI WITOON

A Thesis Submitted in Partial Fulfillment of
the Requirements for the Degree of
Doctor of Engineering (Chemical Engineering)
Graduate School, Kasetsart University
2010

Thongthai Witoon 2010: Synthesis of Bimodal Porous Silica from Rice Husk Ash Using Chitosan as Template and the Application as Catalyst Support for Fischer-Tropsch Synthesis. Doctor of Engineering (Chemical Engineering), Major Field: Chemical Engineering, Department of Chemical Engineering. Thesis Advisor: Associate Professor Metta Chareonpanich, D.Eng. 111 pages.

Bimodal porous materials with different pore sizes exhibit several applications including catalysis, adsorption, and selective separation due to the fact that their small pores can interact with reactant molecules whereas large pores provide high-speed pathways for the transport of gas and liquid molecules. In this work, the bimodal porous silicas were synthesized via the sol-gel technique using rice husk ash as a silica source and chitosan as a template. The studied variables were pH of mixture, chitosan/silica ratio, and aging temperature. It was found that the largest amount of chitosan was incorporated into the silica network at pH value of 6 due to the strong interaction between positively charged amino groups of chitosan and negatively charged silica oligomers. The silica cluster size could be controlled by manipulating the chitosan/silica ratio through the silica entrapment within the voids of chitosan networks. After chitosan removal, macropores were formed by the aggregates of small silica cluster size (100-200 nm). The different morphologies of bimodal porous silica products including inter-connected and particle aggregated structures were also observed with the change of aging temperatures. The obtained bimodal porous silicas were used as the support of cobalt catalysts and tested for the performance of Fischer-Tropsch synthesis reaction. The obtained data was compared to those of monomodal porous silica supports. It was found that the cobalt-loaded monomodal porous silica gave higher CO conversion within 8 h on stream. After that, the CO conversion was drastically decreased because of the deposition of heavy hydrocarbons and the oxidation of cobalt active phase (Co^0) to inactive phase (CoO). The coke deposition could be accelerated by the very long pore length of monomodal porous silica supports. For bimodal porous silicas, the pore length of was significantly short, thus the heavy hydrocarbons could be easily penetrated from the catalyst pores. As a result, CO conversion with more stability and higher C_{5+} selectivity were obtained with cobalt-loaded bimodal porous silica supports.

_____	_____	___ / ___ / ___
Student's signature	Thesis Advisor's signature	

ACKNOWLEDGEMENTS

I would like to take this opportunity to acknowledge the people who have helped to make this work possible. My sincere gratitude to my thesis advisor, Associate Professor Dr. Metta Chareonpanich, for her consistent and thoughtful advice, and help during the course of this work, and to my graduate committees; Associate Professor Dr. Paisan Kongkachuichay and Associate Professor Dr. Phungphai Phanawadee for their kindly giving the time to advise, revise and approve my thesis.

I would like to thank Professor Dr. John T. Gleaves and Professor Dr. Gregory Yablonsky who guide me research works during my stay at the Department Energy, Environmental and Chemical Engineering, Washington University in St. Louis (WUSTL), USA and my sincere thank to Xiaolin Zheng for her constant help, encouragement and the nice time during my stay in USA. I also would like to thank staffs at the Department of Chemical Engineering at Kasetsart University and Dr. Chareonpanich's research group for their kind helps and supports.

Finally, I would like to thank my family for their love, support, encouragement, and their understanding during the whole period of my education. My family has been my greatest source of strength and inspiration. My gratefulness devotes to my family who wholeheartedly support me away.

<div align="right">
Thongthai Witoon

February 2010
</div>

TABLE OF CONTENTS

Page

LIST OF TABLES

iii

LIST OF FIGURES

LIST OF FIGURES (Continued)

LIST OF FIGURES (Continued)

LIST OF FIGURES (Continued)

Appendix Figure

SYNTHESIS OF BIMODAL POROUS SILICA FROM RICE HUSK ASH USING CHITOSAN AS TEMPLATE AND THE APPLICATION AS CATALYST SUPPORT FOR FISCHER-TROPSCH SYNTHESIS

INTRODUCTION

Over the past two decades, there has been an increasing interest in the synthesis of various porous silicas by using organic materials as the structure-directing agents in order to entirely control the pore system ranging from micropores to macropores. Among a wide variety of the synthesis process of porous silicas, the modified sol-gel processes are particularly attractive due to the simplicity and versatility of their synthesis conditions; this provides a possibility for organic species to mix with inorganic precursors to tailor-made the unique characteristics of the silica products with tunable porous structure.

The type of organic species used as the structure-directing agents is one of the main factors affecting the microstructure and macroscopic characteristics of porous silica; it is caused by the interactions formed between organic and inorganic species. Several attentions have been recently paid to synthesize the porous silica materials with bimodal pore size distribution (meso-macropore). Such materials can provide high specific surface area and more interaction sites via small pores, whereas the presence of additional macropores can enhance mass transport and accessibility to the active sites through the use of these bimodal porous materials. These features make such materials highly preferable and promising for applications in catalysis and separation technology (Takahashi *et al*., 2007; Kim *et al.*, 2009).

Concerning the preparation methods of bimodal porous silicas, the active raw materials such as tetraethyl orthosilicate (TEOS), colloidal silica, fume silica, and the structure-directing agents such as nonionic, cationic and anionic (i.e., Poly(sodium-4-styrene sulfonate), Poly(acrylic acid), Poly(ethylene oxide), Pluronic, Poly(propylene

oxide), cetyltrimethyl ammonium bromide) surfactants were applied (Nakanishi, 1997; Kim *et al.*, 2009). Due to the fact that these raw material and the structure-directing agents are fairly expensive and/or toxic to environment in some extent, the utilization of low cost and environmentally friendly natural products is therefore a challenging task for cleaner production of bimodal porous silicas. Rice husk, an abundantly available waste in all rice producing countries, can be used as an excellent raw material for the production of the highly reactive amorphous silica under controlled conditions (Mansaray *et al.*, 1999; Kamiya *et al.*, 2000; Della *et al.*, 2002). The amorphous silica with a high specific surface area could be prepared from rice husk by heat treating at 700 $^{\circ}$C in air, and the obtained product was easily dissolved in aqueous sodium hydroxide solution to form sodium silicate solution (Kamath and Proctor 1998; Chareonpanich *et al.*, 2004).

In addition, chitosan produced commercially by deacetylation of chitin, the structural element of the second most abundant organic material which is the main constituent of the shell of crustaceans such as shrimps, crabs and lobsters can be possibly applied as the pore structure-directing materials instead of the groups of surfactants. A better understanding of the formation of composite materials in order to clarify the key physico-chemical principles that can be further led to new synthetic procedures is of significant essential. However, very few researches on the silica-chitosan interactions under acidic condition have been reported and the formation of the hybrid materials is still not well understood. Ayers and Hunt (2001) studied the effect of chitosan to silica ratio on physical properties and biocompatibility screening of hybrid aerogels, whereas Hu *et al.* (2001) observed the effect of chitosan concentration on the structure of porous silica products by using small-angle neutron scattering and transmission electron microscopy techniques. Moreover, Retuert *et al.* (2003) focused on the synthesis of silica-chitosan hybrid materials by using sol-gel process through the solvent evaporation and precipitation in ammonium hydroxide solution, resulting in the flat irregular shaped and porous spherical silica particles.

Recently, the intensive concerns of fossil energy depletion, air pollution and global climate change have encouraged many researchers to focus in the production of

clean alternative energy. In order to deal with the continually massive fuel consumption and the restriction of the emitted pollutants, high quality transportation fuels are needed. One of the promising alternative energy is the synthetic fuels produced by the Fischer-Tropsch process, which have received increasing attention worldwide due to the compatibility with existing petroleum infrastructure and vehicles (Takeshita and Yamaji, 2008).

According to the fact that Fischer Tropsch synthesis reactions can be controlled by a number of factors such as support properties, metal precursor characteristics, calcination temperatures, and so on. Among them, the pore size of the support has a large effect not only on the catalytic activity but also the product selectivity. For example, the catalytic activity is proportional to the amount of active sites on the surface of catalysts. The increase of active sites can be obtained by dispersing the active metal on the catalyst support. The larger surface area of catalyst supports can provide higher active surface. However, the support with the large surface area usually contains small pore, resulting in poor intra-particle diffusion of reactants, intermediates and products which leads the higher CH_4 selectivity and coke deposition. When the support with large pore size is used, the aggregate and low dispersion of metal are often obtained. To overcome this limitation, the support with bimodal porous structure which contains both large pores and small pores is of great interest since its small pores could provide higher metal dispersion, meanwhile it is able to diminish the diffusion resistance by its large pores.

In this thesis, an attempt to reduce the cost of raw materials by the use of environmental safety, renewable resources for bimodal porous silica synthesis has been focused. Rice husk ash was used as the silica source and chitosan was used as the pore-structure directing agent. The effects of the pH value of mixture and the calcination temperature on the formation of the silica/chitosan composites, and structural and physical properties of bimodal porous silica products were investigated by using nitrogen sorption technique, scanning electron microscopy (SEM), transmission electron microscopy (TEM), thermogravimetric analysis (TGA), and zeta potential analyzer. Moreover, the effects of chitosan/silica mass ratios and aging

temperature on the pore structure were investigated. The mechanisms of bimodal porous silica formation were proposed. These results provided an essential information for further development of a simple, low-cost route to synthesize the porous silica products with novel structure and tailored properties. The obtained bimodal porous silica products were then used as the catalyst support; in this case cobalt metal of specific amount was loaded onto the bimodal porous silica by using the wet-impregnation technique. After that, the Fischer-Tropsch synthesis reactions were performed in order to clarify the effect of the bimodal pore structure and the result was compared to those obtained from the monomodal pore structure.

OBJECTIVES

1. To study the bimodal porous silica synthesis using rice husk ash as the silica source and chitosan as the template

2. To study the effect of pH of mixture, chitosan/silica ratio, and aging temperature on the structural and physical properties of bimodal porous silica products

3. To study the effect of bimodal porous silicas on the physicochemical properties of cobalt-loaded bimodal porous silica catalysts

4. To investigate the role of bimodal porous silica supports on Fischer-Tropsch synthesis performances

Benefits

1. Bimodal porous silica can be successfully synthesized by using low-cost and environmentally benign rice husk ash and chitosan as raw materials.

2. Pore sizes of bimodal porous silica can be controlled by varying the pH values of mixture, chitosan/silica ratio, and aging temperature.

3. The influence of bimodal porous silica support on the physicochemical properties of cobalt-loaded bimodal porous silica catalysts has been clarified.

4. High stability and selectivity of long chain hydrocarbon products in the range of gasoline to diesel can be achieved over the catalysts prepared by using bimodal porous silica as the support in Fischer-Tropsch synthesis.

LITERATURE REVIEW

Bimodal Porous Silica Synthesis

Bimodal porous materials are materials having pores of two different sizes including micro-mesopore, micro-macropore and meso-macropore. Among these groups of materials, the active surfaces of small pores can interact with molecules, whereas large pores provide high-speed pathways for the transport of gas and liquid molecules (Takahashi *et al.*, 2007). The bimodal porous materials have several applications including catalysis, adsorption, and selective separation, where both molecular transportation and interaction between solid surface and molecules occur simultaneously.

Because of the wide variety of advantages, many researchers have focused on the synthesis of bimodal porous materials via sol-gel method using organic materials as template for the formation of the larger pores (macropore). The background theories of the bimodal porous silica synthesis consisting of the formation of porous materials via sol gel process, the formation of bimodal porous silica and the possibility for the use of chitosan as template were explained in detail below.

1. Formation of Porous Materials via Sol-Gel Process

1.1 Basic sol-gel chemistry

The sol-gel process is a more useful solution for making porous materials. By using this technique, water and low molecular weight alkoxide are used as material precursors. There are several kinds of low molecular weight alkoxides such as tetraethoxysilane ($Si(OC_2H_5)$: TEOS), aluminum isopropoxide ($C_9H_{21}AlO_3$: AIP) or tetramethoxysilane (TMOS), which can be used as silica and alumina precursors. The alkoxide can be hydrolyzed with water and formed silanol groups ($\equiv Si\text{-}OH$), where either acid or base is used as the catalyst. The reactions of alkoxysilanes can be summarized in three steps including (1) hydrolysis of the

alkoxide, (2) silanol-silanol condensation, and (3) silanol-ester condensation, as shown in Equations 1-3, respectively.

Hydrolysis reaction

$$\equiv Si - OR + H_2O \longleftrightarrow \equiv Si - OH + ROH \qquad (1)$$
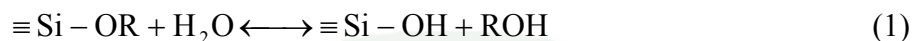
Water condensation (silanol- silanol condensation)

$$\equiv Si - OH + HO - Si \equiv \longleftrightarrow Si - O - Si \equiv + H_2O \qquad (2)$$
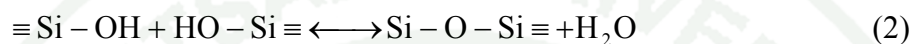
Alcohol condensation (silanol- ester condensation)

$$\equiv Si - OH + RO - Si \equiv \longleftrightarrow Si - O - Si \equiv + ROH \qquad (3)$$
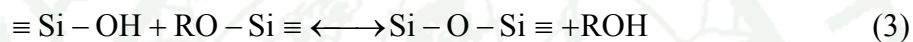
The formation of porous silica can be consecutively taken place in three stages: (1) polymerization of monomer ($Si(OH)_4$) to form particles, (2) growth of particles, and (3) linking of particles together into branched chains, then networks, finally extending throughout the liquid medium, thickening it to a gel. The schematic diagram of these stages is shown in Figure 1.

Monomer

Dimer

Cyclic

Particle

pH < 7 or pH 7-10
with salts
A

B
pH 7-10
without salts

1 nm

5 nm

10 nm

30 nm

100 nm

Three-dimensional gel
networks
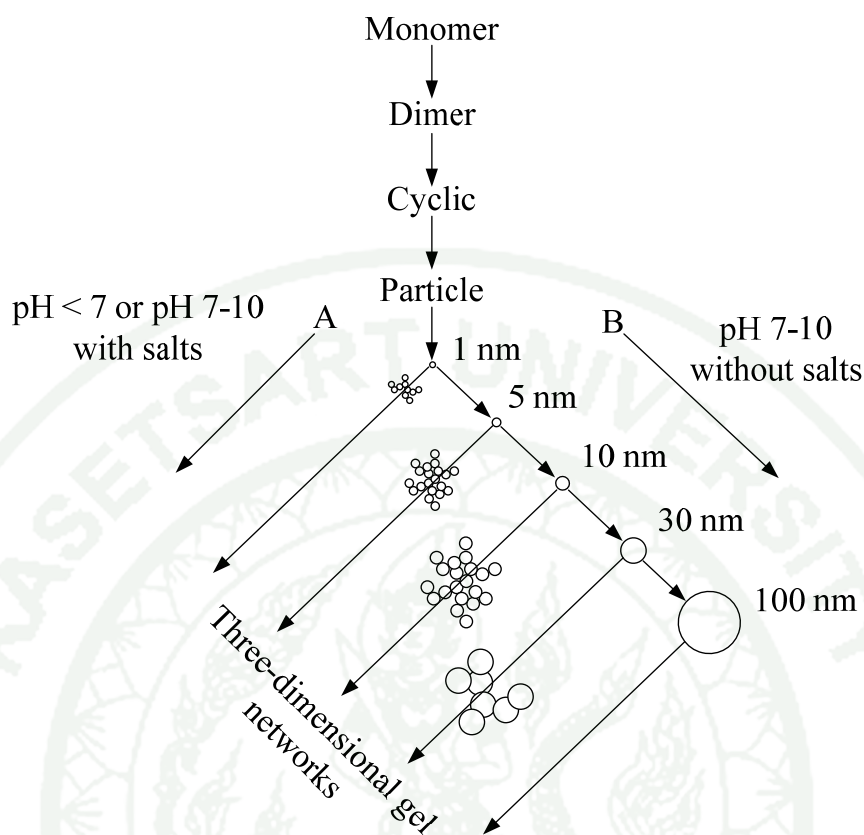
Figure 1 Polymerization behavior of silica: in acid solution or a presence of flocculating salts (A), particles aggregate into three-dimensional networks and form gels; in basic solution (B) particles in sol grow in size with decrease in numbers.

Source: Iler (1979)

  1.2 Factors affecting the sol-gel processes

        The network structures of silica products can be controlled by varying molar ratio of the water and alkoxide, the catalyst type or concentration, by controlling the silica networks via heat treatment or using alkyl-substituted alkoxides or other additives. The effect of these parameters and the relationship between the obtained gels and porous silica products were reviewed as the detail shown below.

1.2.1 The water to alkoxide molar ratio

The water to alkoxide molar ratio (R) has significant effect on the silica microstructure products (Brinker and Scherer, 1990). When the water to alkoxide molar ratio is low, alcohol condensation is dominated and gelation period is longer, leading to more microporous materials. Gels prepared from higher water content (R > 4) have shown coarser microstructure than those prepared from lower water content (R < 4). However, when the water to alkoxide ratio is more than 10, the microstructure was only slightly dependent on water content. The gels prepared from lower water content have more unreacted alkoxy ligands than those of higher water content and therefore form more linear chain-like structures. At higher water concentration, more branched polymers are formed. Fibrous structures are possibly formed from sols prepared at low water/TEOS ratio and low pH.

1.2.2 Effect of pH on sol-gel reaction

Brinker and Scherer (1990) studied the effect of pH on the pore structure and morphology of porous silica products. Varying the pH value of mixture affects the relative rates of hydrolysis and condensation. When increasing the pH values, products can be transformed from branch silica to particulate silica as shown in Figure 1.

Iler *et al*. (1979) classified the pH range of the polymerization process into three ranges including pH < 2, pH 2-7 and pH > 7. At pH = 7, the silica solubility and dissolution rates are maximized. The kinetic mechanisms of the reaction depend on pH value of the mixture. With acidic pH, particle growth stops once the size of the products reach 2 to 4 nm. At pH higher 7, particle growth mainly depends on temperature and the particles of more than 100 nm in diameter can be formed (particulate sols). This is due to the fact that the charge of particles is highly negative and they repel each other, resulting in the segregation of solid particles. At pH near the isoelectric point, the repulsive forces between particles are low and

therefore, particles possibly collide to each other and form continuous networks, leading to gel formation.

1.3 Relationship between structure of gel and porous silica

The porous structure of porous silica products was strongly influenced by the drying of the gel network. It was shown that the surface tension forces created in a gel during solvent removal could cause the network to fold or crumple when the coordination of particles was increased (Iler, 1979). The relationship between the structure of the gel of porous silica is shown schematically in Figures 2-4 along with a TEM micrograph of the corresponding xerogel for three characteristic gel types (Brinker and Scherer (1990)).

The linear polymer system which was formed under conditions where the condensation rate was low (pH 2) tend to be overlapped (Figure 2). Because the structure could freely interpenetrate, the compliant structure can rather freely reduced in size during the solvent removal. As a result, the tiny pores are formed after drying process.

(a)   (b)   (c)
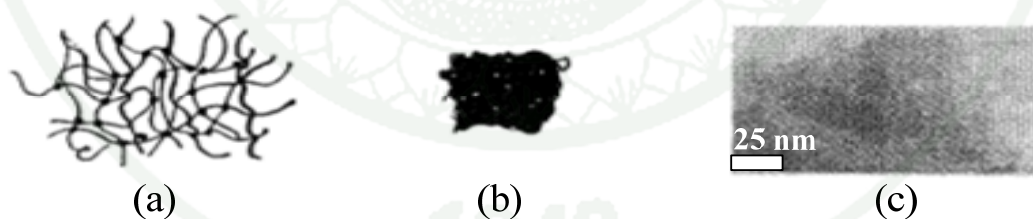
Figure 2 Schematic representation of (a) weakly cross-linked acid–catalyzed gel, (b) dried gel, and (c) TEM micrograph.

Source: Brinker and Scherer (1990)

At the pH range of 3-8 (Figure 3), the more highly branched structures were prevented from interpenetrating due to strong inter-cluster, steric effects. The

shrinkage of the structure was terminated at an earlier stage of drying due to the stiffness of the impinging clusters. Therefore, the porous structure with larger pores compared to the linear chain systems was formed.

(a)   (b)   (c)
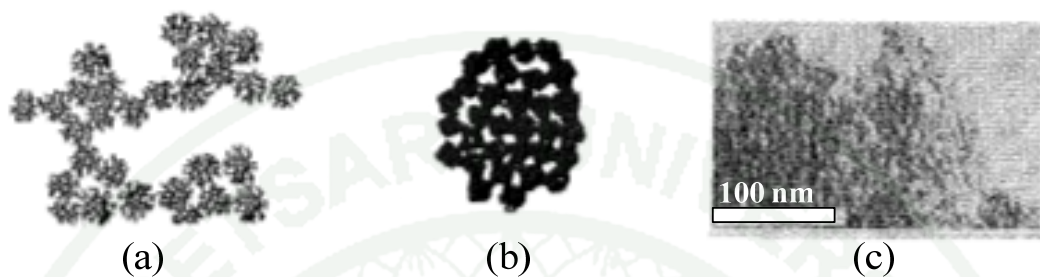
Figure 3 Schematic representation of (a) more branched silica system, (b) dried gel, and (c) TEM micrograph.

Source: Brinker and Scherer (1990)

In the case of base-catalyzed hydrolysis of silicon alkoxide, colloidal particles were formed as a gel phase. The drying process could serve only to rearrange the particle assemblage to achieve higher coordination number because particle interpenetration was not possible. Therefore, the aggregates of uniform particles were mainly obtained.

(a)   (b)   (c)
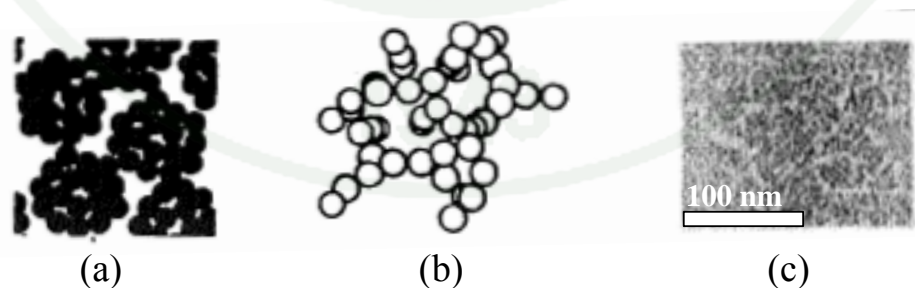
Figure 4 Schematic representation of (a) packing of colloidal particles, (b) random packing of colloidal particles, and (c) TEM micrograph.

Source: Brinker and Scherer (1990)

2. Formation of Bimodal Porous Silica Using Different Organic Materials

As mentioned previously, porous silicas with monomodal porosity of different pore size could be formed in a system of silica-water component by varying the synthesis condition. The addition of suitable organic materials into such system can promote the phase separation, resulting in the formation of silicate/organic rich-phase and water-rich phase. After the removal of organic materials, the macropore structure was left in the porous silica products. Accordingly, the bimodal porous silica was synthesized. In this part, the thermodynamics of binary system, and the synthesis of bimodal porous silica using different organic template materials were reviewed.

2.1 Thermodynamics of binary system

The compatibility in a system containing at least one kind of polymeric species can be estimated by the thermodynamic treatment known as the Flory-Huggins formulation (Flory, 1942; Huggins, 1942). The Gibbs free energy change of mixing for binary system can be expressed as follows:

$$\Delta G \alpha RT\left[\left(\phi_1 / P_1\right)\ln \phi_1 + \left(\phi_2 / P_2\right)\ln \phi_2 + \chi_{12}\phi_1\phi_2\right] \qquad (1)$$

where ϕ_i's and P_i's (i= 1 and 2) are denoted as the volume fraction and the degree of polymerization of each component, respectively, and χ_{12} is the interaction parameter. The former two terms in the bracket reflect the effect of entropy, and the last term is the enthalpy change. The entropic terms are generally negative which promote the mixing of two components. The increase of the degree of polymerization of either component can destabilize the system, making its less compatible. Once the sign of ΔG turns from negative to positive, a driving force of phase separation then increases. The similar evidence can occur if the positive enthalpic contribution increases as the polymerization proceeds.

Stuaffer *et. al.*, (1982) described a model relevant to polymerizing monomers in the presence of solvent molecules. They found that the phase separation process depended on the formation of bonds between adjacent monomers. The model explaining these phenomena was classified into "weak" or reversible gels and "strong" or irreversible gels. The effect of phase separation in different cases was investigated experimentally by Nakanishi (1997).

2.2 Structure evaluation during phase separation

The structure evaluation during phase separation was early described by the linearized theory and the schematic diagram is shown in Figure 5. The structure obtained by phase separation process was varied by the polymer concentration and the reaction temperature. However, the final structure was depended on the competition of between phase separation and freezing process (gelation). Accordingly, the fragmentation of the domain often occurred when the phase separation in the system formed without altering the freezing process.
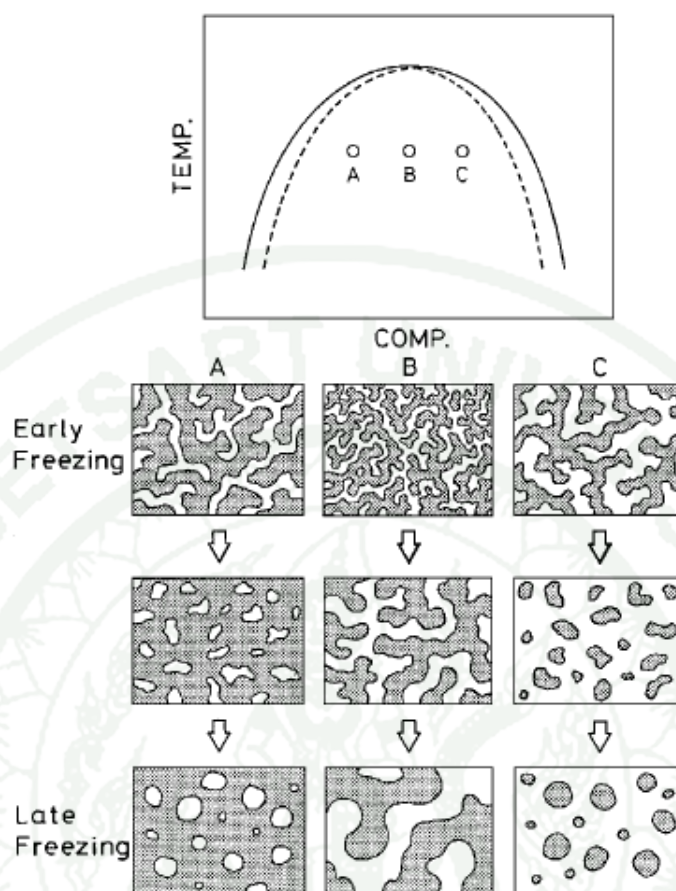
Figure 5 The onset and time evolution of coarsening of phase separating domains which occurs at various locations in the unstable region.

Source: Nakanishi (1997)

2.3 Phase separation by entropy driven systems

Nakanishi (1997) found that two polymers including poly(sodium-4-styrene sulfonate) and poly(acrylic acid) had weak interaction with silicate polymer. The obtained bimodal porous silicas synthesized using each type of polymer as the additive with varying concentrations and reaction temperatures were explained in detail as follows:

2.3.1 Poly(sodium-4-styrene sulfonate)-silicate-solvent system

Poly(sodium-4-styrene sulfonate) or NaPSS, had a strongly ionic bond which could be easily dissolved in water but exhibited a limited solubility in alcohols. The structure of sodium-4-styrene sulfonate is shown in Figure 6.
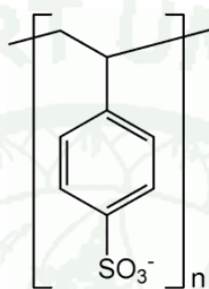
Figure 6 Schematic illustration of the structure of sodium-4-styrene sulfonate.

Source: Wikipedia (2007)

The structural observation using scanning electron microscopy (SEM) of porous silica products using NaPSS as an additive (Figure 7) revealed that the well-defined interconnected structures were obtained only in the limit of NaPSS/silica ratio. At higher ratio, the spherical gel particles of a few micrometers in the macropores were observed accompanied by the isolated pores within the continuous gel skeletons. It was found that temperature mainly affected the size of silica domain which was significantly reduced by increasing the temperature because the gel formation could be accelerated and the solubility was increased.

2.3.2 Poly(acrylic acid)-silicate-solvent system

Poly(acrylic acid), HPAA, is a weakly acidic polymer with appreciable solubility both in water and alcohols. The structure of acrylic acid is shown in Figure 8.

(a)   (b)

(c)   (d)

(e)   (f)
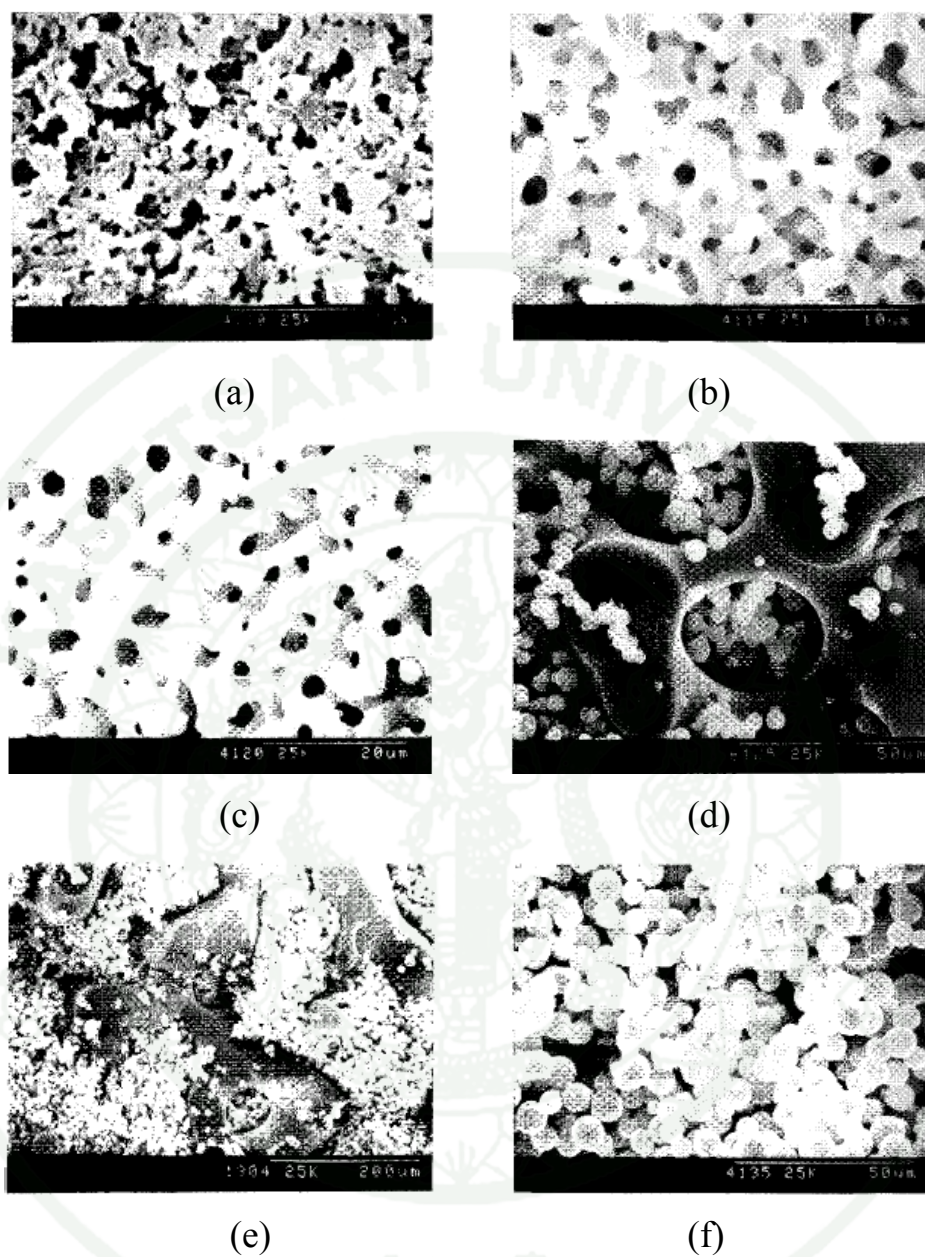
Figure 7 SEM micrographs of resultant gel morphology of NaPSS-TMOS system at
varied molar ratio of NaPSS/silica, C, at 40 ^{o}C; (a) C=0.133, (b)
C=0.156,(c) C=0.163, (d) C=0.170, (e) C=0.176, and (f) C=0.188.

Source: Nakanishi (1997)
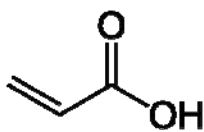
Figure 8 Schematic illustration of the structure of acrylic acid.

Source: Wikipedia (2008)

The effect of molar ratio of HPAA/silica on the structural morphology of silica product is shown in Figure 9. The size of silica domain and the amount of macropores were increased with the increase of the HPAA/silica ratio. The interconnected structures were formed in the limited range of HPAA/silica ratio, where the volume fractions of gel and fluid phases became comparable. The increase of reaction temperature gave the similar result obtained by using NaPSS. The difference between HPAA and NaPSS was that the interconnected structure could be obtained in an extended water/alcohol range using HPAA system.

2.4 Phase separation by enthalpy driven systems

When the organic polymers exhibit strong interaction such as the hydrogen bond with silanol groups, the phase separation is driven by the repulsive interaction between solvent mixtures and silica oligomers. Nakanishi (1997) pointed out that several kinds of polymers such as poly(ethylene oxide), PEO, and poly(acrylamide) could be used as the organic polymers in this type of phase separation. The results for a system of PEO-silicate-water were described below.

2.4.1 Poly(ethylene oxide)-silicate-solvent system

Figure 10 shows the SEM micrographs of gel morphology with different compositions (Nakanishi, 2006). It was clearly seen that the increase of the PEO/silica ratio caused the decrease of the size of silica domain which was in contrast to the HPAA system as mentioned above. The increase of reaction temperature also gave the similar results obtained by using HPAA and NaPSS systems.
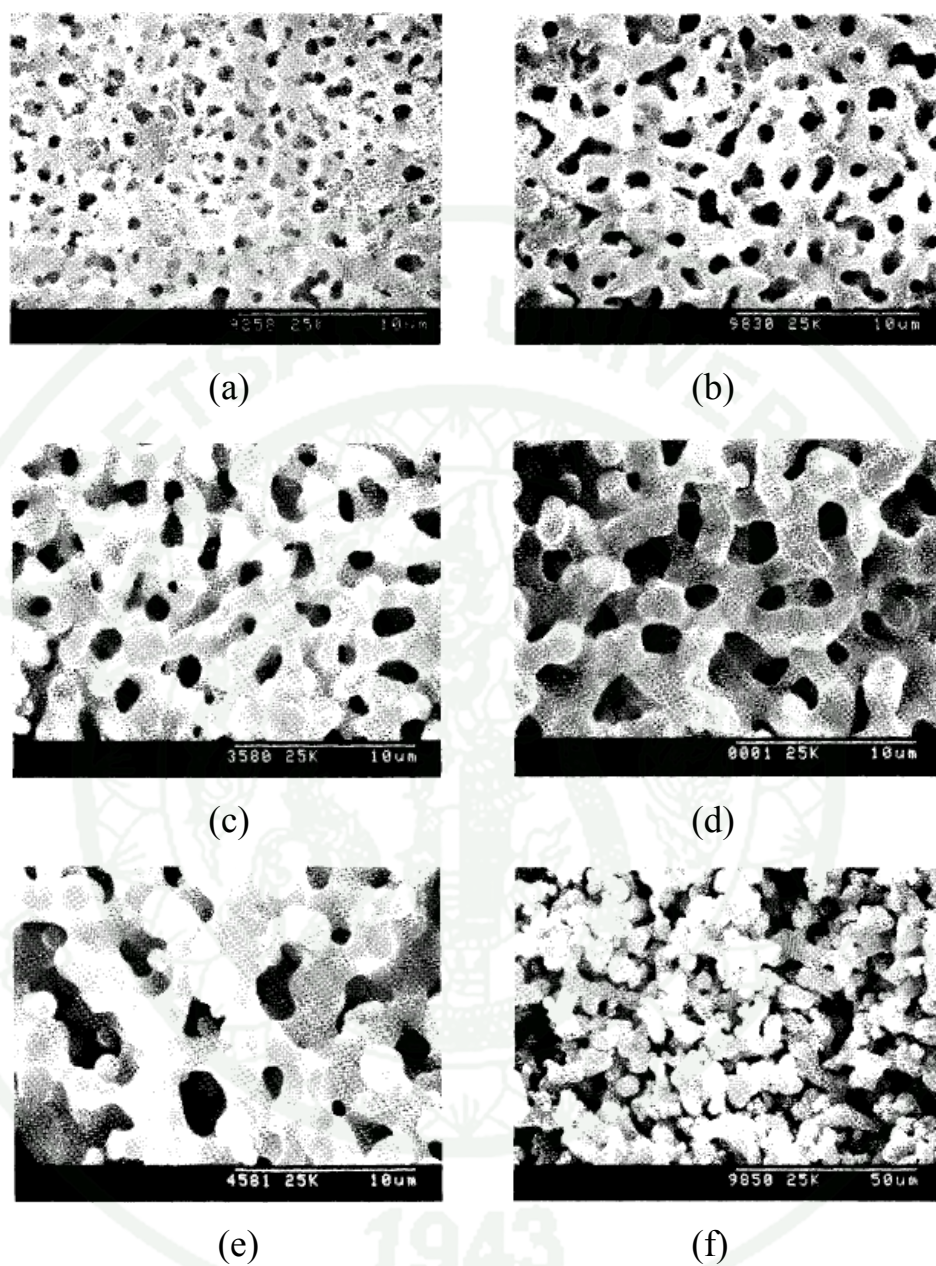
Figure 9 SEM micrographs of resultant gel morphology with varied molar ratio of
HPAA/silica, C, at 80 $^{\circ}$C; (a) C=0.111, (b) C=0.133,(c) C=0.155, (d)
C=0.177, (e) C=0.200, and (f) C=0.222.

Source: Nakanishi (1997)
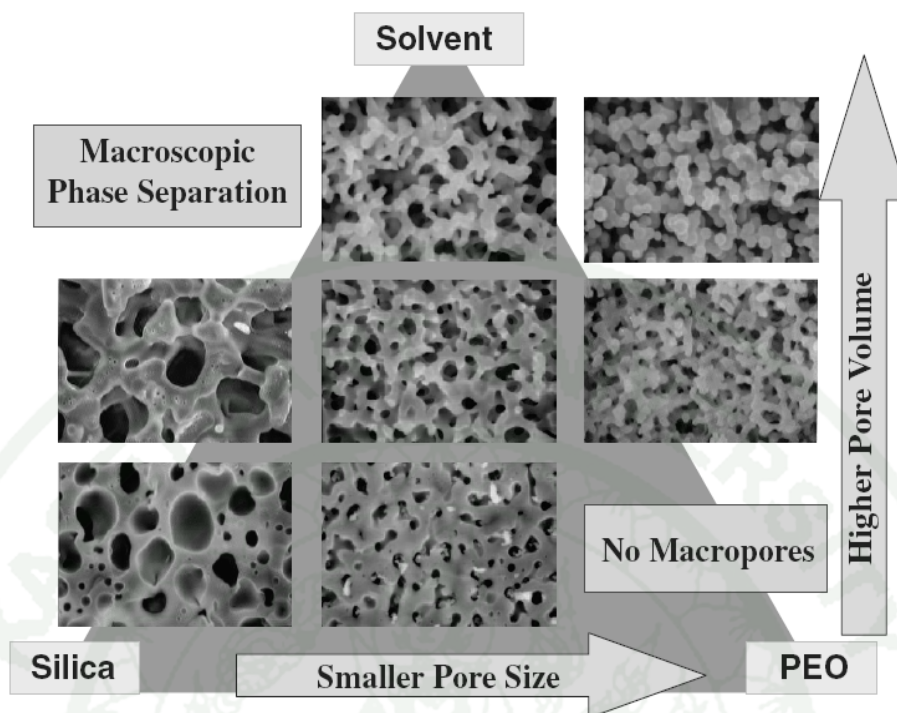
Figure 10 SEM micrographs of resultant gel morphology using different compositions.

Source: Nakanishi (2006)

However, the silica precursors including TEOS and TMOS as silica sources and the template such as NaPSS, HPAA and PEO are expensive and toxic to environment. In order to obtain bimodal porous silica with low-cost and environmentally safety, the renewable raw materials should be concerned. In Thailand, a tremendous quantity of rice husk ash was produced as a by-product from steam power plants. Some of rice husk ash was used as the raw material for light aggregates, cement and concrete productions. From the chemical analysis data, rice husk ash is composed of more than 97% of SiO_2. It was both technically and economically suitable for the use as silica source instead of the commercial silicas such as TEOS, fumed silica and sodium silicate. Chareonpanich *et. al.* (2004, 2007) reported the preparation of sodium silicate from rice husk ash and the use as the silica source for zeolite and SBA-15 synthesis. The results indicated that sodium silicate derived from rice husk ash had significant potential for the use as silica source.

Moreover, chitin, a major component of the shells of crustacean such as crab, shrimp, and crawfish, is the second abundant natural polymer. However, the native chitin does not respond to sol-gel processing due to its poor solubility. Alternatively, chitosan derived from chitin was nontoxic, biodegradable and could be soluble in dilute acid. Chitosan chemistry has been widely investigated due to basic scientific interest as well as for practical applications, such as the uses in food industry, biomedical and agricultural applications. In comparison with the molecule of cellulose, chitosan has more reactive centres in its structure of which depends on the reaction conditions. In an acidic medium or without a catalyst, reactions can take place at the amine group. In alkaline medium, the amine group is more reactive and O-substitution occurs. Due to its excellent properties, chitosan is attractive as the template for the formation of macroporosity.

3. Possibility for the Use of Chitosan as the Template

A molecular illustration of chitosan is shown in Figure 11. The amino and acetamide groups are randomly distributed along the backbone of chitosan. As mentioned above, the phase separation-induced bimodal porous silica formation can occur by the weak and strong interaction between polymer and silica. The chitosan presented the amino groups and oxygen atoms which can form the strong interaction with silanol group through the electrostatic interaction and hydrogen bonds, respectively. These interactions promote the possibility for the use of chitosan as the template for the synthesis of bimodal porous silica.

However, the conformation of chitosan chains in the chitosan-water mixture significantly depends on pH values as shown in Figure 12. At low pH values, strong electric repulsion caused by high protonation of amino groups of chitosan is formed, resulting in a dispersion of the chitosan chains. When the pH of solution is increased, the degree of protonation of amino groups decreases and the repulsion of the amino groups also decreases, resulting in the aggregate of chitosan chains. This evidence implies that the pH of mixture should be primarily studied and then the composition and reaction temperature should be investigated accordingly.

R = H or COCH₃
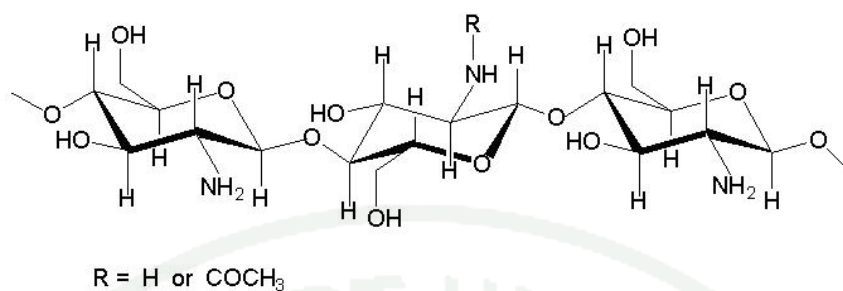
Figure 11 Schematic illustration of the structure of chitosan.

Source: Pedroni *et. al.* (2000)

Dispersion   Aggregation
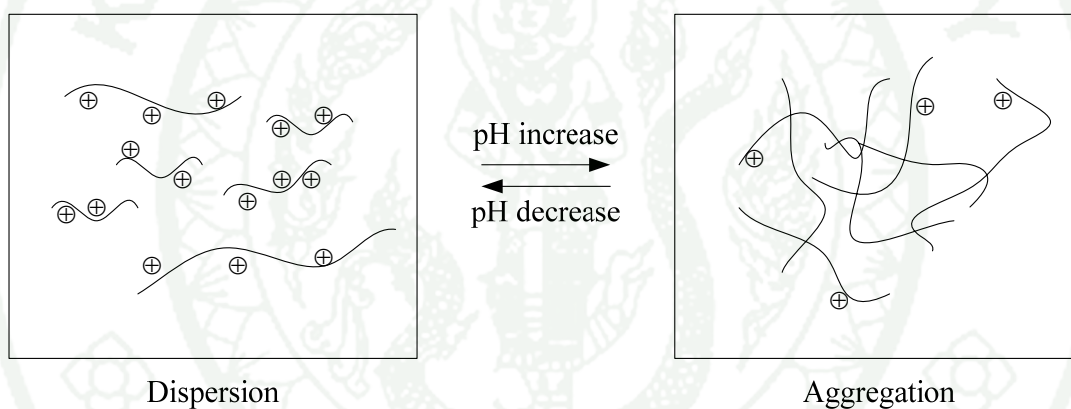
Figure 12 Schematic illustration of effect of pH values of mixture on the structure of
chitosan.

Source: Berger *et. al.* (2004)

Fischer-Tropsch Synthesis

Fischer-Tropsch synthesis (FTS) is one of the major routes for converting coal-based and/or natural gas-derived syngas into high quality chemicals and fuels. The main goal of FTS research is to develop Fischer-Tropsch catalysts with high activity and selectivity by improving the selectivity of C_{5+} hydrocarbons while decreasing the selectivity of methane. In particular, liquid fuels in the range of diesel fuels produced by Fischer-Tropsch process (synthesis of hydrocarbons from CO and H_2) exhibit attractive potential as very clean alternative energy, relative to the conventional fossil petroleum. The products generated from FTS are mainly composed of linear paraffins with high cetane number and are free of sulfur and aromatic pollutants (Van der Laan and Beenacker, 1999). In order to improve the performances of Fischer-Tropsch catalysts and increase the selectivity of the desired hydrocarbon products (C_{10}-C_{20}), informative research understanding is reviewed as the following description.

In the last decades, the interest in FTS has been increased as a result of the decrease in fossil energy reserves, environmental demands and technological developments. Fischer-Tropsch synfuels have become a key alternative fuel regarding the CO_2 policy because of their low transportation cost and compatibility with existing petroleum infrastructure and vehicles (Takeshita and Yamaji, 2008). In addition, Fischer-Tropsch synfuels are virtually interchangeable with conventional diesel fuels and can be blended with diesel at any ratio without or with little modification. Concerning carbon monoxide and particulate matter, Fischer-Tropsch fuels offer important emission benefits compared with diesel.

1. The Fischer-Tropsch Process

Fischer-Tropsch process is a method for the synthesis of hydrocarbons and other aliphatic compounds principally for producing synthetic petroleum substitutes. FT process was discovered by Franz Fischer and Hans Tropsch, the German coal researchers, in 1923. This process was invented in petroleum-poor but coal-rich

Germany to produce alternative fuels during the World War II. The original Fischer-Tropsch synthesis was described by the following chemical equations:

$$CH_4 + 1/2O_2 \longrightarrow 2H_2 + CO \qquad (2)$$

$$(2n+1)H_2 + nCO \longrightarrow C_nH_{2n+2} + nH_2O \qquad (3)$$
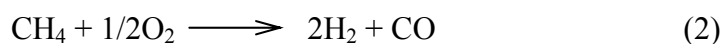
FTS reaction is regarded as a surface catalyzed polymerization process and a lot of heat is involved during reaction. The adsorbed CH_x monomers, formed by hydrogenation of adsorbed CO, react with the surface H atoms and hydrocarbon fragments to produce hydrocarbons with a broad range of chain lengths due to the limitation of the typical Anderson-Schultz-Flory (ASF) distribution (Iglesia, 1997). In this process, synthesis gas (a mixture of hydrogen and carbon monoxide) can be converted to large ranges of petroleum products such as methane, synthetic gasoline, waxes, alcohols, and water over heterogeneous catalysts (Van Der Laan *et al.,* 1999; Davis, 2001; Saib *et al.,* 2002). The mechanism of FTS reaction is quite complex because there are many reactions occurred during the reaction (as shown in Table 1) and the product selectivity typically follows the Anderson-Schultz-Flory (ASF) distribution (Iglesia, 1997; Davis, 2001).

2. Mechanism of the Fischer-Tropsch Synthesis

Although studies over 70 years concerned the mechanism of the FTS, there still was a controversy over the reaction pathway. A mechanism for Fischer-Tropsch synthesis was quite complex and difficult to propose the existent procedures. Unlike many reactions, FTS converts two of the simplest compounds, H_2 and CO, into a complex array of products, consisting predominantly of alkenes and alkanes but also varieties of minor compounds including the range of oxygenate compounds. The major mechanisms and modified forms were reported as follows:

Table 1 Major overall reactions in the Fischer-Tropsch synthesis

Main reactions	Chemical equations
1) Paraffins	$(2n + 1)H_2 + nCO \rightarrow C_nH2_{n+2} + nH_2O$
2) Olefins	$2_nH_2 + nCO \rightarrow C_nH_{2n} + nH_2O$
3) Water gas shift reaction	$CO + H_2O \leftrightarrow CO_2 + H_2$
Side reactions	
4) Alcohols	$2nH_2 + nCO \rightarrow C_nH_{2n+2}O + (n - 1)H_2O$
5) Boudouard reaction	$2CO \rightarrow C + CO_2$
Catalyst modifications	Chemical equations
6) Catalyst oxidation/reduction	$M_xO_y + yH_2 \leftrightarrow yH_2O + xM$
	$M_xO_y + yCO \leftrightarrow yCO_2 + xM$
7) Bulk carbide formation	$yC + xM \leftrightarrow M_xC_y$
Overall reactions	$nCO + (n + 0.5m)H_2 \rightarrow C_nH_m + nH_2O$
	$CO + 2H_2 \rightarrow -CH_2- + H_2O \ (\Delta H° = -165 \text{ kJ/mol})$

Source: Henricus (2001)

In the 1950s, the oxygenate (enol) mechanism was achieved widely acceptance. This mechanism involved the chemisorption of CO which reacted with adsorbed hydrogen to form a unit species such as:
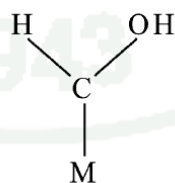
where M is metal active site.

A combination of condensation and water elimination steps by using adjacent groups on the site of active metal resulted in structural growth (Davis, 2001). The enol groups were condensed as depicted in Figure 13.

Figure 13 Schematic illustration of the oxygenate (enol) mechanism.

Source: Davis (2001)

Furthermore, the oxygenate mechanism that involved the reaction between CO and adsorbed hydrogen was proposed. Besides, an insertion mechanism composed of the insertion of CO into a metal-methyl or metal-methylene carbon bond was also proposed. The inserted metal-methyl or metal-methylene was then hydrogenated to produce an alcohol or alkene; oxygen in the alcohol or alcohol precursor can also be eliminated to produce an alkene product. The scheme of this mechanism is shown in Figure 14.

(* rate controlling)

Figure 14 The insertion of CO into a metal-methyl or metal-methylene carbon bond.

Source: Davis (2001)

Davis (2001) also reported the original carbide mechanism for the formation of hydrocarbon and oxygenate products in FTS. The carbide mechanism included the formation of metal carbide followed by the hydrogenation of metal carbide to produce various hydrocarbon products.

With the general availability of surface science instruments, it was found that CO adsorbed on active metal surfaces to produce the surface covered with carbon, and some of oxygen. This phenomenon led to the conclusion that CO was chemisorbed

and dissociated to form adsorbed C and adsorbed O. This step was followed by the rapid hydrogenation of adsorbed O to produce water. The hydrogenation of adsorbed carbon to form CH_2 is much slower. This mechanism was proposed by Maitlis (1989) and is shown in Figure 15.
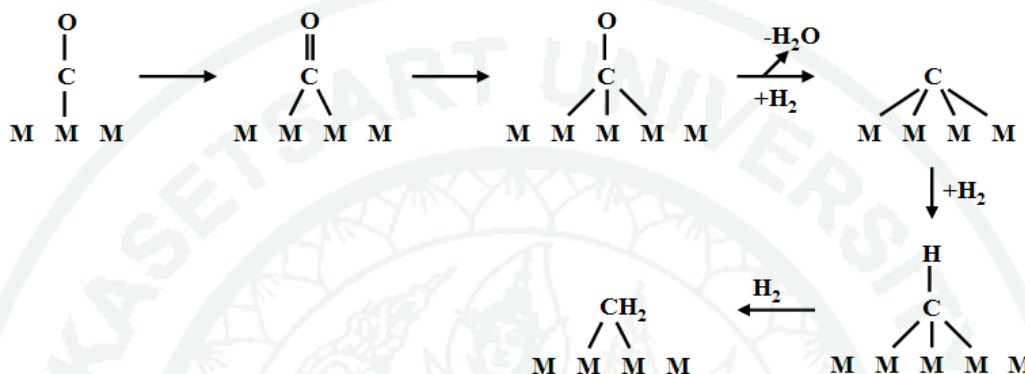
Figure 15 Mechanism for the insertion of CO into a metal-methyl or metal methylene carbon bond.

Source: Davis (2001)

FTS had been typically characterized as a surface polymerization since the monomer units were produced from the syngas (hydrogen and carbon monoxide) on the surface of catalyst. In 1999, Steen and Schulz reported the developed equations describing the rate of CO consumption in FTS. As the FTS reaction yielded aliphatic organic compounds and the by-products water and/or carbon dioxide. Carbon monoxide was consumed for the formation of organic compounds or carbon dioxide. Therefore, the rate of CO consumption equaled the rate of organic compound formation on carbon basis and could be written as:

$$-r_{CO} = r_{C, org} + r_{CO_2} \qquad (4)$$

where $r_{C, org}$ is the rate of consumption of CO for the formation of organic compounds in FT synthesis.

According to the polymerization reaction, the formation of organic compounds in FTS was featured as three classes of reaction including initiation, propagation, and termination. The initiation step could be defined as the formation of a chain starter from CO and H_2. The propagation step was the incorporation of monomer units into growing chain (the chain growth step); the monomer was produced in situ on the catalyst surface during FTS reaction. Finally the termination step was the desorption of growing chains from the catalyst surface. Such that the rate of carbon monoxide for the formation of organic compounds thus equaled the sum of the rate of carbon monoxide consumption in the initiation, propagation and termination steps.

Steen and Schultz also developed the polymerization kinetics of Fischer-Tropsch CO hydrogenation based on an assumption that the rate of reaction in the FTS was controlled by the rate of hydrogenation of surface carbon which was formed through CO dissociation. Surface carbon was hydrogenated and CH_x-surface species was obtained, this reaction was regarded as a chain starter. Figure 16 presents a simplified scheme for the formation of chain starters and incorporation into growing alkyl chains using the polymerization principle.
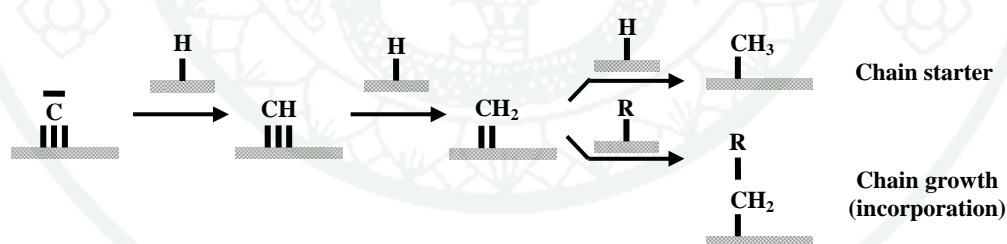
Figure 16 Simplified kinetic scheme of the successive hydrogenation of surface
carbon yielding chain starters and incorporation into growing chains.

Source: Steen and Schulz (1999)

The FTS produced different olefins and paraffins of different chain lengths. This process was basically a chain-building mechanism, where the chain either gained

length by adsorbing another CO group, or terminated and left the catalyst as either paraffin or olefin. This proposed mechanism is graphically shown in Figure 17.

$$
\begin{array}{ccc}
CH & \xrightarrow{+H} & CH_4 \\
\alpha \downarrow +CH_2 & & \\
C_2H_4 \longleftarrow C_2H_4 & \xrightarrow{+H} & C_2H_6 \\
\alpha \downarrow +CH_2 & & \\
C_3H_6 \longleftarrow C_3H_6 & \xrightarrow{+H} & C_3H_8 \\
\alpha \downarrow +CH_2 & & \\
\vdots & & \\
C_nH_{2n} & &
\end{array}
$$
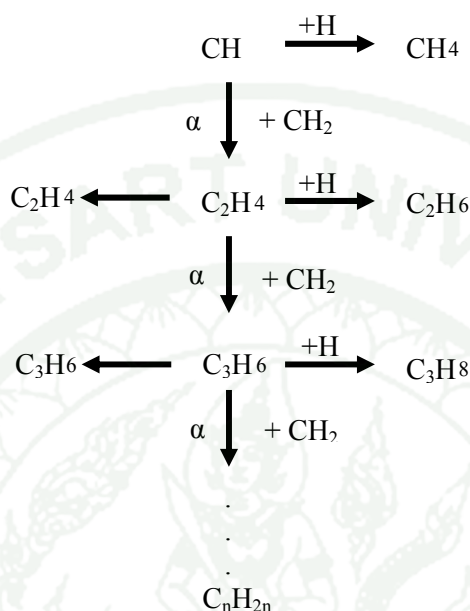
Where α is a chain growth probability

Figure 17 Two possibilities of termination; to a paraffin (right side) or a olefin (arrow to the left), or to grow further with the absorption of CO and H_2 as CH_2.

Source: Iglesia (1997)

Recently, many researchers specified the CH_2 insertion as a dominant mechanism for the FTS. However, the formation of oxygenate compounds were hardly possible via the CH_2 insertion mechanism so that oxygenate compounds were assumed to be formed via the CO insertion mechanism. In order to explain both of the formation of hydrocarbons and oxygenates, the formation of CH_2 monomers was proposed and carbide mechanism involving C-O bond dissociation was firstly introduced to react with H_2 to form methylene (CH_2). In 2008, Gaube and Klein proposed a new mechanism of the FTS on iron and cobalt catalysts based on the

hypothesis that two incompatible mechanisms were involved on CH_2 insertion and on CO insertion, respectively. The development of the novel mechanism was based on experimental studies of many researchers who employed various types of iron and cobalt catalysts.

3. Fischer-Tropsch Catalysts

Fischer-Tropsch synthesis process was shown to be catalyzed by certain transition metals, with cobalt (Co), iron (Fe) and ruthenium (Ru) presenting the noticeably high activity (Vannice, 1977). Cobalt and iron based catalysts were typically applied to FTS process. Moreover, ruthenium and nickel based catalysts also had good activity for FTS, however the availability of ruthenium was limited, thus it was not economically possible. The nickel based catalyst had high activity but methane selectivity was very high, and moreover the performance at high pressure was poor, due to production of volatile carbonyls. Consequently, the FTS reaction was catalyzed focusing on cobalt (Iglesia, 1997 and schultz, 1999) and iron (Luo and Davis, 2003 and Zhang *et al.,* 2006) as practical catalysts.

Nevertheless, the supported Co-based catalysts have been widely used for the synthesis of long chain paraffins (Dry, 1990; Chanenchuk *et al.,* 1991; Iglesia,1997) according to their high activity for syngas conversion and high yields of linear hydrocarbons in FTS reaction at medium reaction temperature and pressure (Iglesia, 1997; Ernst *et al,* 1999). Moreover, Co-based catalysts were more stable toward deactivation by water (by-product of the FTS reaction), less active for the competing water-gas-shift (WGS) reaction and produced less oxygenates than the Fe-based systems. In order to achieve high amount of surface-active sites (Co^0), cobalt precursors were dispersed on porous carriers such as SiO_2, Al_3O_4 and TiO_2.

4. Support Effect on Cobalt-based Fischer Tropsch Catalysts

The different kinds of supports revealed different influences on structure, dispersion and reducibility of cobalt particles. The advantage and disadvantage of various supports are summarized in detail as follows:

4.1 Silica-supported catalysts

Interaction between support and cobalt was relatively weak in silica-supported catalysts and this usually led to better cobalt reducibility. However, cobalt dispersion was much lower in silica-supported catalysts than in alumina-supported catalysts. Thus, increasing the cobalt dispersion is the major challenge in the design of silica-based Fischer-Tropsch catalysts. Ernst *et al.* (1999) studied the Fischer-Tropsch activity and selectivity of Co/SiO_2 prepared by the sol-gel technique in acidic and basic media. It was found that the activity in FTS was increased with the increasing specific surface area, and the selectivity for higher molecular weight hydrocarbons was favored in the case of the catalyst with support pore diameter of less than 4 nm. Song and Li (2006) reported the results of cobalt catalysts supported on porous silica with different pore sizes. They found that the large cobalt particles could provide large flat metallic surface, favoring bridge-type adsorbed CO and induced the formation of long chain hydrocarbons. In contrast, small cobalt particles could provide more edges and corners, favoring the CO adsorption in linear geometry of which led to the methane selectivity.

4.2 Alumina-supported catalysts

Alumina is one of the frequently used supports for cobalt FT catalysts. However, a major problem due to the use of alumina support is that the cobalt reducibility because cobalt oxide strongly interacts with alumina support and forms relatively small cobalt crystallites. Chemical reaction of small cobalt particles with the support might result in the formation of cobalt aluminate spinels which decrease the activity and product selectivity in FTS (Chin *et. al*., 1982).

4.3 Carbon-supported catalysts

A drawback of oxide support (silica or alumina) is their reactivity towards cobalt, which can lead to mixed oxides (silicate or aluminate). These mixed oxides are not active in FTS and are reducible only at high temperature. In order to avoid these problems, the use of carbon as a support has been explored. Tavasoli *et al.* (2008) prepared carbon nanofibers as catalyst supports. They found that the strong metal-support interactions were reduced to a large extent and the reducibility of the catalysts was significantly improved. However, the carbon supports caused a slight decrease in the FTS product distribution to lower molecular weight hydrocarbons.

4.4 Bimodal pore-supported catalysts

High cobalt dispersion can be obtained by the deposition of a cobalt salt on the supports such as silica and alumina. Conventional monomodal support with a large surface area usually contains small pores, resulting in poor intra-pellet diffusion of reactants and products, especially in multiphase reactors. Slow transportation of reactants and products to and from catalytic sites often controls the rate of primary and secondary reactions. The bimodal porous material supports contain large pores and small pores simultaneously. The small pores provide the sites for supporting small cobalt particles, while the large pores provide a network for fast diffusion of reacting molecules and products. The typical pore size distribution in bimodal porous silica is shown in Figure 18. The catalytic performance in FTS of cobalt loaded on the bimodal and monomodal porous silica support was reported by Tsubaki *et. al.* (2001). They found that the cobalt loaded bimodal support gave higher CO conversion and lower CH_4 selectivity.

As mentioned above, it is clearly seen that the bimodal porous silica is a promising support for cobalt-based Fischer Tropsch catalyst. In this research, the novel bimodal porous silica synthesized using chitosan template was employed as the cobalt support. The monomodal porous silica was also used to distinguish the effect of bimodal porous silica support. The physical and chemical properties of catalysts,

and their catalytic performances were investigated. Moreover, the cobalt phases and the amount of carbon deposition were investigated in order to clarify the effect of the existence of bimodal pore structure.
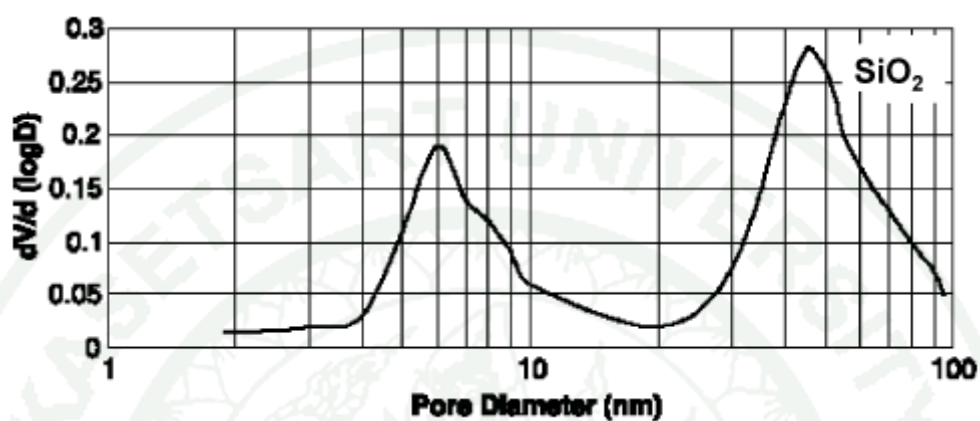
Figure 18 Pore size distribution of bimodal catalyst support.

Source: Tsubaki *et. al.* (2001)

MATERIALS AND METHODS

In this present work, a simple, low-cost route to synthesize the porous silica products with novel structure and tailored properties through the sol-gel modified process using sodium silicate as the silica source and chitosan as the template were investigated. The effects of essential factors including pH of mixture, chitosan concentration (chitosan/silica ratio), and aging temperature on textural properties and porosity of bimodal porous silica products were clarified. The obtained bimodal porous silica products were after that examined for their potential application in the synthesis of gasoline via the Fischer-Tropsch (FTS) reaction. The detail of equipments, materials and methods for the synthesis of porous silica products and the test for the catalytic performance on FTS reaction are shown as follows.

Synthesis of Bimodal Porous Silica

1. Equipments of Bimodal Porous Silica Synthesis

    1.1   Digital hot plate and stirrer (Schott, SLR)

    1.2   Magnetic hot plate and stirrer (Schott, SLR)

    1.3   Furnace (Carbolite, ELF10/6)

    1.4   Balance (Metler Toledo, AT 400)

    1.5   Hot air oven (Binder, ED53)

    1.6   Autoclave (in house made)

2. Materials of Bimodal Porous Silica Synthesis

    2.1   Rice husk ash

    2.2   Chitosan (Eland Corporation, 90.0 % deacetylation)

    2.3   Sodium hydroxide (NaOH: Merck; Purity, 99.0 %)

    2.4   Hydrochloric acid (HCl: J.T. Baker; Purity, 36.5 -38.0 wt. %)

    2.5   Acetic acid (CH_3COOH: BDH; Purity, 100%)

    2.6   Distilled water

3. Methods of Bimodal Porous Silica Synthesis

In order to synthesize the bimodal mesoporous silica from rice husk ash, prior to the mesoporous silica synthesis, rice husk ash-derived sodium silicate solution was firstly prepared (Chareonpanich *et al.,* 2004) and used as the silica source for bimodal porous silica synthesis. The detailed procedures were as follows:

3.1   Preparation of sodium silicate from rice husk ash

First, 100 g of dried rice husk was refluxed with 1 L of 1 M HCl for 2.5 h. The acid-treated rice husk was washed thoroughly with distilled water, dried at 120 ^{o}C and burned in oxygen atmosphere at 600 ^{o}C for 1 h. The residual ash was composed of 99.7 wt. % silica (examined by X-ray Fluorescence Spectroscopy).

Sodium silicate solution ($Na_2Si_3O_7$: 4 wt.% NaOH; 27 wt.% SiO_2) was prepared from rice husk ash (based on 99.7 wt.% silica). In this stage, 1 g of rice husk ash was dissolved in 7.40 mL of 1 M NaOH solution. The obtained mixture was stirred at approximately 80°C until rice husk ash was completely dissolved and the clear solution of sodium silicate was obtained. The volume of mixture was one half reduced in order to obtain the desired composition of sodium silicate solution by simple evaporation (Chareonpanich *et al.,* 2004). Sodium silicate synthesis scheme is summarized as shown in Figure 19.
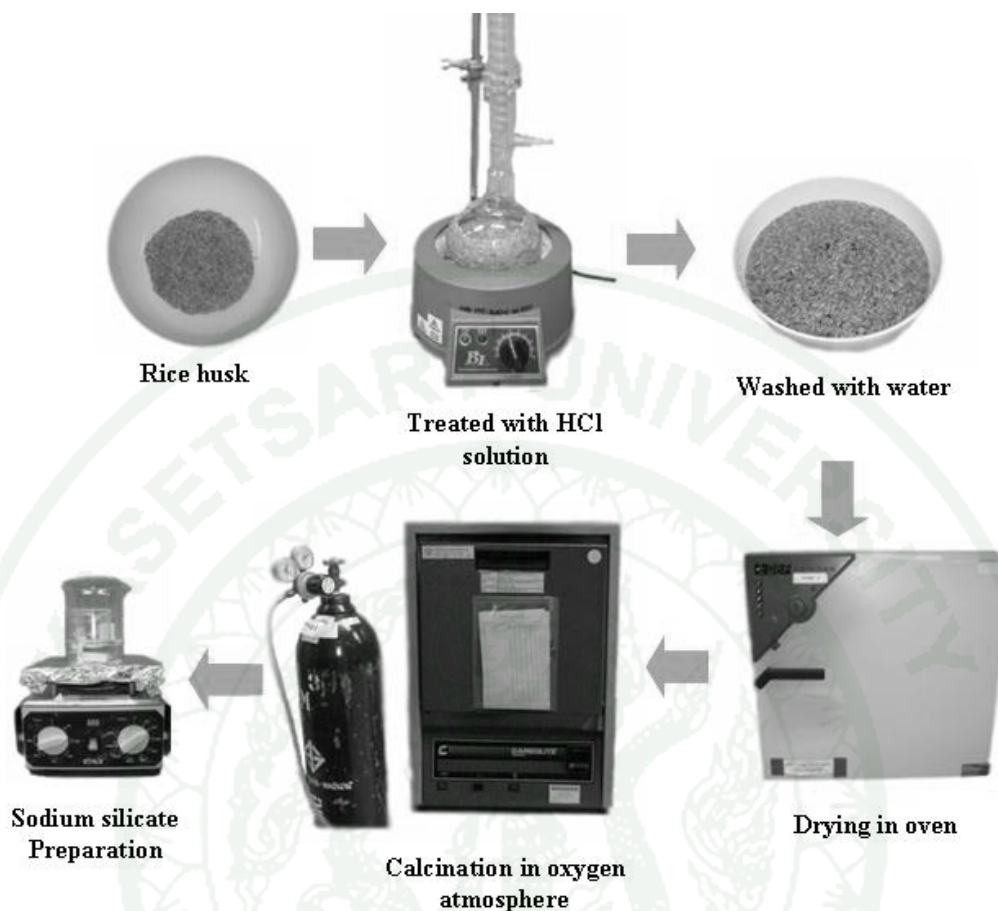
Figure 19 Schematic diagram of sodium silicate synthesis process.

3.2 Preparation of bimodal porous silica

First, chitosan was dissolved in 60 ml of 2% v/v acetic acid in deionized water at room temperature. Then, sodium silicate solution was primarily diluted with 10 ml of deionized water and slowly added to the chitosan solution with vigorous stirring. The pH of solution was adjusted. After that, the hydrolysis-condensation reaction was carried out at 40 $^{\circ}$C for 24 h, and then the resultant solution was aged in the Teflon-lined autoclave at different temperatures for 24 h. The solid products were filtrated, washed several times with distilled water, dried at 120 $^{\circ}$C for 24 h and calcined at 550 $^{\circ}$C for 4 h with the heating rate of 2 $^{\circ}$C/min. The schematic detail of this series of experiment is shown in Figure 20.
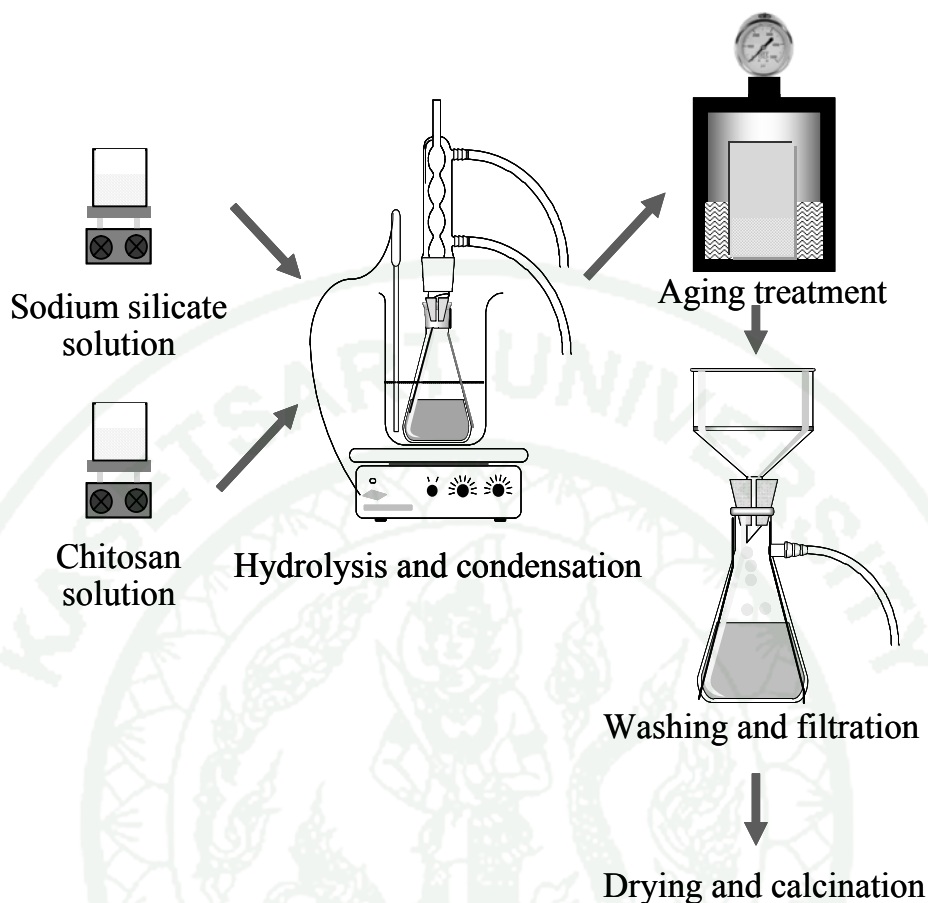
Figure 20 Schematic diagram of bimodal porous silica synthesis.

Due to the fact that the conformation of chitosan molecules strongly depends on the pH of solution, therefore, the effect of pH of solution on the formation of chitosan/silica composites and bimodal porous silica products were preliminary investigated. In order to clarify the effect of pH of solution and the existence of chitosan, the similar conditions were repeated without the use of chitosan and the detail of synthesis condition is shown in Table 2. After the effect of pH of solution was elucidated, the effect of chitosan/silica ratio and aging temperature were consecutively investigated as the detail of experimental conditions shown in Table 3 in order to obtain the suitable characteristics of bimodal porous silicas as the catalyst support for FTS reaction.

Table 2 Synthesis conditions for the study of effect of pH of mixture on textural properties of bimodal porous silica products.

Sample ID [a]	Synthesis Conditions [b]	
	pH of solution	Chitosan/silica (g/g)
P-2	2	0
P-3	3	0
P-4	4	0
P-5	5	0
P-6	6	0
C-2	2	0.8
C-3	3	0.8
C-4	4	0.8
C-5	5	0.8
C-6	6	0.8

[a] Porous silica products were prepared without (P) and with (C) chitosan template, designated as P-x and C-x, where x is the pH of mixture.

[b] The aging temperature and calcined temperature were fixed at 100 ^{o}C and 600 °C, respectively throughout this series of experiment.

Table 3 Synthesis conditions for the study of effects of chitosan/silica ratio and aging temperature on textural properties of bimodal porous silica products.

Sample ID [a]	Synthesis Conditions [b]	
	Chitosan/silica (g/g)	Aging temperature (^{o}C)
CS0-40	0	40
CS0-60	0	60
CS0-80	0	80
CS0.1-40	0.1	40
CS0.1-60	0.1	60
CS0.1-80	0.1	80
CS0.4-40	0.4	40
CS0.4-60	0.4	60
CS0.4-80	0.4	80
CS0.8-40	0.8	40
CS0.8-60	0.8	60
CS0.8-80	0.8	80
CS1.6-40	1.6	40
CS1.6-60	1.6	60
CS1.6-80	1.6	80

[a] Porous silica products were prepared with (C) chitosan template, designated as CSx-y, where CS is chitosan-silica composite, x is chitosan/silica mass ratio, and y is aging temperature.

[b] The pH of solution was fixed at pH 6 and products were calcined at 550 °C throughout this series of experiment.

4. Characterization of Bimodal Porous Silica

A number of analytical techniques including thermogravimetric analysis-differential thermal analysis (TG-DTA), zeta potential measurement, N_2 sorption measurement, scanning electron microscopy (SEM), and transmission electron microscopy (TEM) were applied in order to investigate the textural characteristics of chitosan/silica composites and porous silica products. Each technique was itself unique and provided important information for understanding the phenomena of the metastable gel creating from sodium silicate by using chitosan as the organic template. The growth of gel composites, the formation of stable composites, and the textural properties of bimodal porous silica products were investigated and deduced by using those multi-analytical information obtained from the above techniques. Moreover, the formation mechanism of bimodal porous silica products was proposed. The details of major investigation obtained using each instrument including the analysis conditions are shown below.

4.1 Thermogravimetric analysis (TG-DTA)

The amount of chitosan incorporation in the silica/chitosan composites and temperature of chitosan degradation were determined by using Thermogravimetric analyzer (TG-DTA: TA instrument, SDT2960 Simultaneous DSC-TGA Universal 2000). In the analysis process, the sample was heated in air atmosphere from room temperature to 1,000 ^{o}C at the heating rate of 5°C/min.

4.2 Zeta potential measurement

Zeta potentials of chitosan/silica composites were determined by using Zetasizer Nano ZS from Malvern instrument. Zeta potential provided the near-surface charge of colloidal particles. The results enable us to understand the interaction between chitosan macromolecules and silicate species.

4.3 N_2-sorption measurement

BET surface area, sorption isotherms, pore size distribution, and pore volume of porous silica products were analyzed by using N_2-sorption equipment of Quantachrome Corporation (Model: Autosorb1). Prior to each measurement, samples were degassed at 200 ^{o}C under vacuum and followed by flowing helium gas to remove adsorbed water and other volatile matters from the surface of solid samples. The measurement was done at high vacuum level (10^{-4} Torr) at the temperature of liquid N_2 (-196°C) using the total N_2 adsorption/desorption points of 55 points.

4.4   Scanning electron microscopy (SEM)

Surface morphology and silica cluster size of porous silica products were observed by using JEOL JSM6301-F. The powder sample was spread on a carbon tape over alumina specimen mount, and coated with gold (Au) using the sputtering technique.

4.5   Transmission electron microscopy (TEM)

Transmission electron microscopy (JEOL JEM-2010: Figure xx) is a powerful characterization tool that provides information regarding the porous structures including size and shape of silica nanoparticles. By using this technique, the sample was dispersed in ethanol (99.9%, Sigma-Aldrich), dropped onto the copper grid and dried at room temperature.

Synthesis of Gasoline via Fischer-Tropsch Synthesis Reaction

The bimodal porous silica obtained from the synthesis process mentioned previously was applied as the catalyst support and tested for the performance of Fischer-Tropsch synthesis reaction. The obtained data was compared to those obtained from monomodal porous silicas; in this case monomodal porous silica and bimodal porous silica with the mesopore diameters of approximately 4.3, 7.7, and 12.1, respectively were used. The detail of equipments, materials and methods used in this series of experiment are provided below.

1. Equipments of Fischer-Tropsch Synthesis Reaction

    1.1   Catalytic reaction testing unit

- Pressure regulator
- Mass flow controller (GFC117, Aalborg)
- Mass flow controller (8300 Series, KOFLOG)
- Thermocouple (K-type)
- Temperature controller (120-R/E, Shino)
- Temperature indicator (RI, Shino)
- Tube furnace (CFW 1300, Carbolite)
- Flexible heating tape (100 volt)
- Voltage transformer (SB-5, SLIDEUP)
- Bubble flow meter

    1.2   Gas analysis unit

- Gas chromatograph equipped with thermal conductivity detector (TCD) and chromatopac data processor (GC-2014, Shimadzu) was used to quantitatively analyze the amounts of H_2O, H_2, CO, CO_2, CH_4 gases.

- Gas chromatograph equipped with flame ionization detector (FID) and Chromatopac data processor (GC-8A, Shimadzu) was used to quantitatively analyze the amounts of hydrocarbon gases (C_1-C_4) and liquids (C_5-C_{15}).

- Gas-tight syringes (1002LTN gastight syringe, Hamilton; and A-2 type gas tight syringe, PS)

- Liquid syringe (80377 Microliter, Hamilton)

2. Materials for Catalyst Preparation and the Performance Test of Fischer-Tropsch Synthesis Reaction

2.1 Materials for catalyst preparation

- Cobalt nitrate ($Co(NO_3)_2 \cdot 6H_2O$: 99.0 % purity, UNIVAR)
- Distilled water

2.2 Materials for Fischer-Tropsch synthesis reaction

2.2.1 Reactant gases

- Carbon monoxide (CO: 99.2 % purity, TIG)

- Hydrogen (H_2: 99.99 % purity, TIG)

- Nitrogen (N_2: 99.99 % purity, TIG)

- Oxygen (O_2: 99.5 % purity, TIG)

2.2.2 Standard gases

Mixture of 5% carbon monoxide (CO), 5% carbon dioxide (CO_2), 5% methane (CH_4), 5% ethylene (C_2H_4), 5% ethane (C_2H_6), 5% propylene (C_3H_6), 5% propane (C_3H_8), 5% i-butane (C_4H_8), 5% n-butane (C_4H_{10}) in helium (He balance): SOXAL.

2.2.3 Standard liquid hydrocarbons

- n-Pentane (n-C_5H_{12}: 99.64 % purity, Fischer chemicals)

- n-Hexane (n-C_6H_{14}: 99 % purity, Merck)

- n-Heptane (n-C_7H_{16}: 99.5 % purity, Fluka)

- n-Octane (n-C_8H_{18}: 99 % purity, Merck)

- n-Nonane (n-C_9H_{20}: 99 % purity, Merck)

- n-Decane (n-$C_{10}H_{22}$: 99 % purity, Merck)

- n-Undecane (n-$C_{11}H_{24}$: 97 % purity, Fluka)

- n-Dodecane (n-$C_{12}H_{26}$: 99 % purity, Merck)

- n-Tridecane (n-$C_{13}H_{28}$: 99 % purity, Fluka)

- n-Tetradecane (n-$C_{14}H_{30}$: 99 % purity, Fluka)

- n-Pentadecane (n-$C_{15}H_{32}$: 99 % purity, Fluka)

- Toluene (C_7H_8: 99.64 % purity, Fischer chemicals)

- Octanol (C_8H_{17}: 99.5 % purity, Unilab)

2.2.4   Quartz wool as the catalyst bed support (Alltech)

3. Methods of Cobalt-Loaded Bimodal Porous Silica Preparation

Cobalt-loaded bimodal porous silica catalysts (based on 20 wt. % loading) were prepared by the wetness impregnation technique. The bimodal porous silica used as the catalyst support in this series of experiment was prepared by the process mentioned previously. First, the certain amount of cobalt nitrate was dissolved in distilled water and then the cobalt nitrate solution was slowly added into 1 g of bimodal porous silica powder. The mixture was then consecutively dried at room temperature for 24 h and 120 ^{o}C for 12 h. The obtained solid product was calcined in air at 550 ^{o}C for 4 h. In order to clarify the effect of bimodal porous silica support, the results were compared with those obtained from cobalt-loaded monomodal porous silicas. The details of different types of catalysts are listed in Table 4.

Table 4 Physical properties of porous silica and cobalt-loaded porous silica catalysts

Catalysts [a, b]	Surface area [c] (m^2/g)	BJH pore [d] diameter (nm)	Mesopore volume (cm^3/g)	Macropore volume (cm^3/g)
MS-1	630	4.3	0.51	0.01
MS-2	611	7.7	0.80	0.02
MS-3	400	12.2	0.96	0.05
BS-1	602	4.3	0.64	0.30
BS-2	489	7.7	0.78	0.36
BS-3	303	12.2	0.72	0.56
Co/MS-1	376	2.8	0.30	0.01
Co/MS-2	371	7.4	0.49	0.03
Co/MS-3	274	12.1	0.61	0.13
Co/BS-1	360	2.8	0.44	0.23
Co/BS-2	327	7.4	0.53	0.27
Co/BS-3	168	12.1	0.44	0.38

[a] Monomodal and bimodal porous silica products were denoted as MS-X and BS-X, respectively.

[b] Cobalt-loaded monomodal and bimodal porous silica catalysts were denoted as Co/MS-X and Co/BS-X catalysts, respectively.

[c] Specific surface area calculated by BET method.

[d] Pore diameter measured by BJH desorption method.

4. Catalysts Characterization

4.1 Specific surface area, pore size distribution and pore volume

The specific surface area, pore volume, BJH pore diameter, and pore size distribution of the catalysts were determined by N$_2$ physisorption using a Quantachrome Autosorb-1C instrument at -196 ^{o}C. Prior to each measurement,

samples were degassed at 200 ^{o}C for 12 h. The pore size distribution and pore volume were determined by BJH method and the specific surface area was estimated by BET method.

4.2 Thermal gravimetric analysis and differential scanning calorimetry

The amount of weight loss and the temperature of cobalt precursor decomposition were investigated using the simultaneous TGA-DTA analyzer in air at a heating rate of 10 ^{o}C/min. The samples weight used in each analysis was between 20 and 25 mg.

4.3 X-ray powder diffraction (XRD)

X-ray powder diffraction measurement was performed at room temperature using a Phillips powder diffractometer with monochromatized Cu-Kα radiation. Cobalt phases were detected by comparing the diffraction patterns with those of the standard powder XRD file compiled by the Joint Committee on Powder Diffraction Standards (JCPDS) published by the International Center for Diffraction Data. The Co_3O_4 crystallite diameters were calculated by using Scherrer equation (as shown below) from the most intense Co_3O_4 peak at 2θ of 36.9.

$$d = \frac{0.89\lambda}{B\cos\theta} \times \frac{180^o}{\pi}$$

where d is the mean crystallite diameter

      λ is the X-ray wave length (1.54 Å)

      B is the full width half maximum (FWHM) of the Co_3O_4 diffraction peak.

4.4   Transmission electron microscopy (TEM)

The structures of cobalt particles on monomodal and bimodal supports were revealed by transmission electron microscopy (JEOL JEM-2010 microscope with the acceleration voltage of 200 kV). The samples were prepared by suspending in ethanol and followed by thermal evaporation of ethanol on a copper grid coated with a carbon film.

4.5   Hydrogen chemisorption

Hydrogen adsorption isotherms were recorded by using Autosorb 1-C, (Quantachrome) at 100 ^{o}C following the method presented by Reuel and Bartholomew (1984). The samples were evacuated at 120 ^{o}C for 3 h, and then reduced in situ in hydrogen at 400 ^{o}C for 6 h. After reduction, the samples were evacuated at 400 ^{o}C for 2 hr to remove the residual H_2, and then cooled to 100 ^{o}C for analyses. The adsorption isotherm was recorded in the pressure interval ranging from 40 to 500 mm Hg. The number of exposed metal atoms on the surface was calculated by extrapolating the total adsorption isotherm to zero pressure. In order to calculate the dispersion, it was assumed that every two adjacent surface atoms of cobalt metal are covered by one hydrogen molecule.

5. **Performance Testing of Fischer-Tropsch Synthesis Reaction**

The catalytic testing unit for the Fischer-Tropsch synthesis reaction is shown in Figure 21. This experiment unit consists of a feed flow measuring and controlling system, a furnace equipped with stainless steel tube reactor and a sampling system. The catalytic reaction testing unit was designed to operate under high temperature and pressure conditions. The details of particular system are explained below.
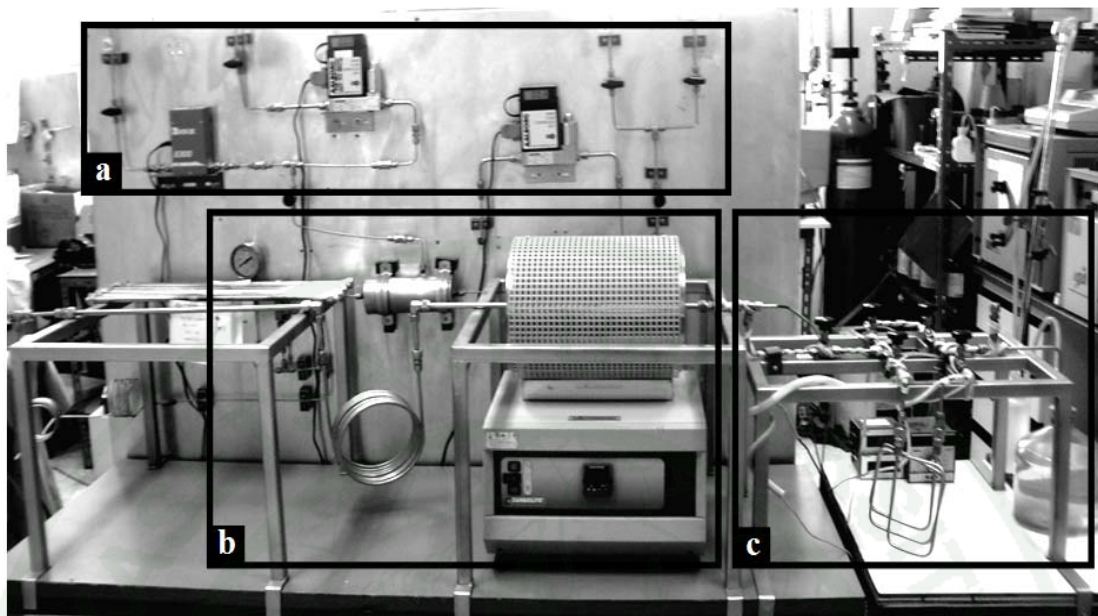
Figure 21 Catalytic reaction testing unit: (a) a feed flow measuring and controlling
system, (b) a furnace-equipped stainless steel tube reactor and (c) a
sampling system.

5.1   The feed flow measuring and controlling system

In this system, mass flow controllers were used to finely indicate and
control the flow rate of feed gases including carbon monoxide, hydrogen, oxygen and
nitrogen. Carbon monoxide and hydrogen were used as reactant gases, hydrogen was
also used for the catalyst reduction, and oxygen was used for calcination process. In
order to monitor the system leakage, nitrogen gas was applied. Flow rates of
hydrogen, oxygen and nitrogen were measured and controlled by Aalborg mass flow
controller (Figure 22a) and KOFLOC mass flow controller (Figure 22b) was used to
control the flow rate of carbon monoxide.
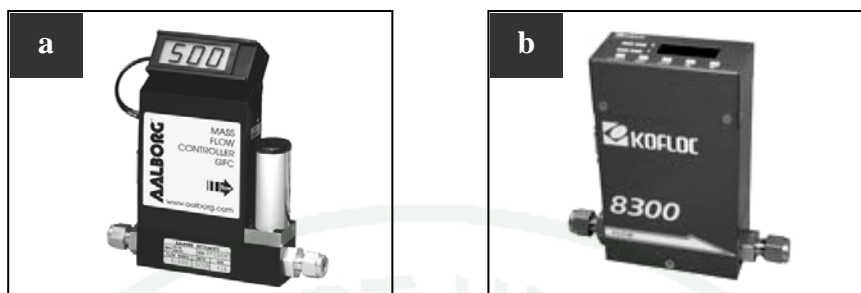
Figure 22 Mass flow controller: (a) Aalborg GFC thermal mass flow controller and
(b) KOFLOC mass flow controller and mass flow meter with indicator.

5.2   The pack bed reactor

The stainless steel (SUS-316, O.D. 3/8") tube was used as the fixed-bed reactor. During the reaction stage, the tube reactor was heated with an electric heater (Figure 23) controlled by the temperature controller. The K-type thermocouple connecting to a temperature controller unit was inserted inside the tube reactor in order to measure and accurately control the temperature of the catalyst bed. The catalyst powder was packed in the isothermal zone of the tube reactor and fixed between quartz wool layers as the scheme shown in Figure 24.

Figure 23 The Fischer-Tropsch synthesis reactor equipped with the electric heater
(Carbolite tube furnace).
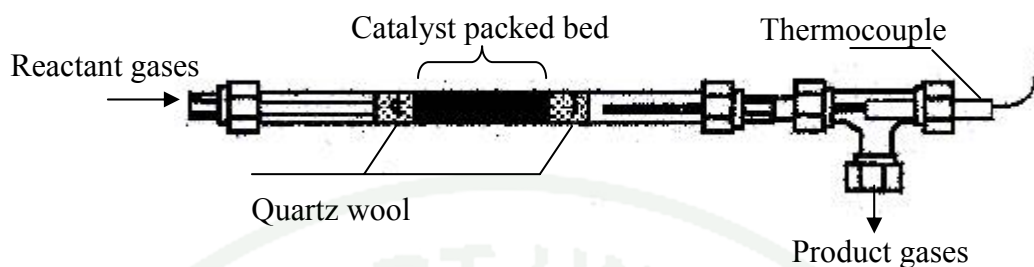
Figure 24 Schematic setup of the stage of Fischer-Tropsch reactor.

5.3   The sampling system

The product gases were immediately sampled using a gas-tight syringe from a heated sampling port connected to the quick release valves as shown in Figure 25. In the sampling unit, the sampling port, tube reactor and metering valves were heated by heating tape to prevent gas condensation. Gas samples were analyzed by 2 gas chromatographs. The mixture of tail gas was trapped by water before venting to atmosphere and the exit flow rate was measured by a bubble flow meter.
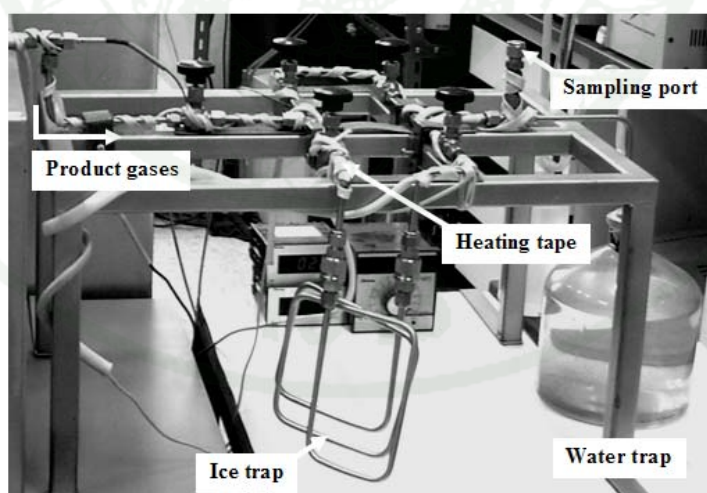
Figure 25 The sampling system consists of release valves, cooling trap, and sampling port heated by heating tapes and connected to bubble flow meter.

5.4   The gas analysis unit

Two types of gas chromatographs were applied to analyze the product gases. For the first gas analysis unit (Figure 26), it consists of Shimadzu gas chromatograph and Chromatopac data processor (GC-2014) equipped with thermal conductivity detector (TCD). The amounts of CO and CO_2 were analyzed using Unibead-C packed column by using helium (99.995 % purity) as the carrier gas and the standard CO and CO_2 gases for TCD products calibration.

The conditions for analysis of CO and CO_2 were:
- Initial carrier gas (He) flow rate: 35   ml/min
- Final carrier gas (He) flow rate: 60   ml/min
- Injector temperature: 180 ^{o}C
- Initial column temperature: 120 ^{o}C
- Final column temperature: 200 ^{o}C
- Detector temperature (Pre):   200 ^{o}C
- Detector temperature: 200 ^{o}C
- Current: 80   mA

Figure 26 Shimadzu gas chromatograph (GC-2014) equipped with thermal
conductivity detector (TCD) and Chromatopac data processor.

The amount of hydrocarbon products (C_1-C_{15}) were analyzed by gas chromatograph (GC-8A, Shimadzu) with flame ionization detector (FID) as shown in Figure 27. A Porapak-Q packed column (Shimadzu) and an OV-1 Uniport HP packed column (Shimadzu) were used to analyze C_1-C_4 hydrocarbons and C_5-C_{15} hydrocarbons, respectively. Helium (99.995% purity) was used as the carrier gas, while hydrogen and air were used as the combustion gas for the flame ionization detector.
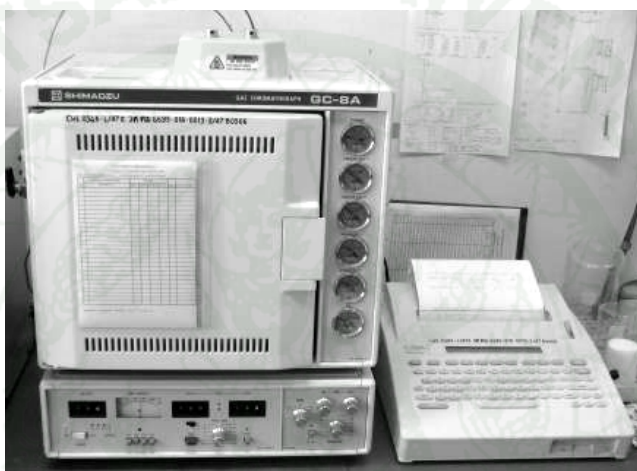
Figure 27 Shimadzu gas chromatograph (GC-8A) equipped with flame ionization
detector (FID) and Chromatopac data processor.

The conditions for analysis of C_1-C_4 hydrocarbons were:

- Primary gas pressure: 200   kPa (2 kg/cm^2)
- He carrier gas 1 pressure: 50   kPa (1 kg/cm^2)
- H_2 gas 1 pressure: 60   kPa (0.6 kg/cm^2)
- Air pressure: 50   kPa (0.5 kg/cm^2)
- Injector/Detector temperature: 230 ^{o}C
- Column temperature: 130 ^{o}C
- Range: 100
- Attenuation: 512
- Analysis time: 15   min

The conditions for analysis of C_5-C_{15} hydrocarbons were:

-	Primary gas pressure:	200	kPa (2 kg/cm^2)
-	He carrier gas 2 pressure:	100	kPa (1 kg/cm^2)
-	H$_2$ gas 1 pressure:	60	kPa (0.6 kg/cm^2)
-	Air pressure:	50	kPa (0.5 kg/cm^2)
-	Injector/Detector temperature:	230	^{o}C
-	Initial column temperature:	30	^{o}C
-	Final column temperature:	230	^{o}C
-	Temperature program rate:	10	^{o}C/min
-	Range:	100	
-	Attenuation:	512	
-	Holding time	5	min
-	Analysis time	50	min

5.5 Testing for the catalytic performance

Before testing the catalytic performance, 1 g of cobalt catalyst was packed in the stainless steel (SUS-316) tube reactor (7.75 mm inner diameter, 0.89 mm wall thickness). Prior to each experiment, the catalyst was activated by reduction in H$_2$ atmosphere at 400 ^{o}C for 12 h at the H$_2$ flow rate of 60 ml/min (NTP) and then flushed and cooled down to room temperature with nitrogen gas. After pretreatment, the catalyst was ready for the catalytic performance test.

During the reaction, CO and H$_2$ were converted to wide ranges of hydrocarbon products over the catalyst at the constant reaction temperature of 230 ^{o}C with the CO/H$_2$ molar ratio of 0.5, total gas pressure of 10 atm and total gas flow rate of 50 ml/min. Light and heavy hydrocarbon products were analyzed by gas chromatographs.

The details of qualitative and quantitative analysis results from gas chromatographs are reported in Appendix A. The results of conversion and selectivity calculated from gas chromatographs data and the detail of calculation are shown in Appendix B.

RESULTS AND DISCUSSION

Bimodal Porous Silica Synthesis

1. Effect of pH of Mixture

The pH of mixture strongly affects solubility and change behavior of chitosan. Chitosan can be easily dissolved in aqueous acidic solutions where the protonation of the amino groups promotes electrostatic repulsion between charged chains. Indeed, at pH higher than 6.2, chitosan in acidic solution carries small amount of positive charges along its backbone. At pH values below 4, nearly all of amino groups ($-NH_2$) of chitosan are expected to be protonated, leading to enhance solubility. Neutralization of chitosan in aqueous solutions to a pH exceeding 6.2, which is close to the pK_a of the amino group, leads to a phase separation or the formation of hydrated gel-like precipitates. Moreover, the pH of solution also affects the electrostatic charge of silicate species. The electrostatic interaction between positively charged NH_3^+ along chitosan chains and negatively charged silicate species can promote the formation of silica-chitosan composites. In this series of experiment, the information of interaction between chitosan and silicate species at various pH values of mixture was obtained from the results of zeta potentials and thermal gravimetric analysis. The removal of the chitosan-rich phase could create the porosity (macropore) as evidenced by N_2-sorption analysis, SEM and TEM spectroscopy.
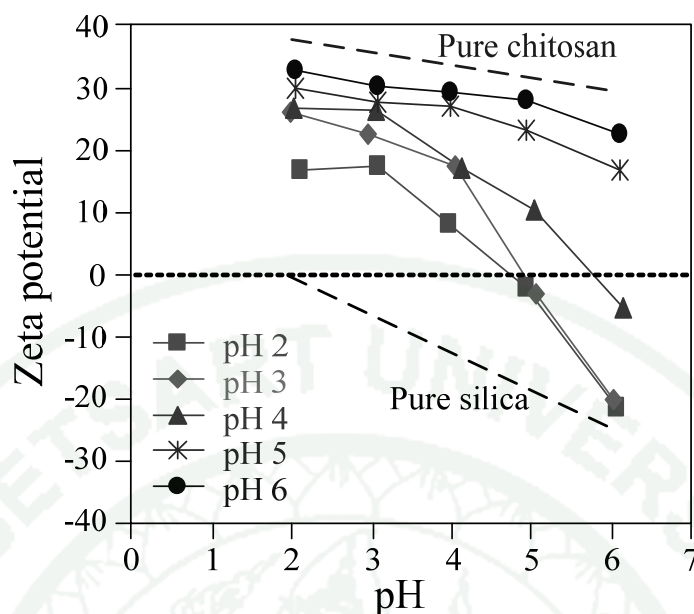
Figure 28 Zeta potentials of silica-chitosan composite at different pH values of
mixture.

The zeta potential analysis was performed to clarify the interaction between
chitosan and silicate species at different pH values (Figure 28). It is known that the
zeta potentials of pure silica are zero (isoelectric point) at pH 2, and negative at pH
higher than 2 (Iler, 1979), while the zeta potential of pure chitosan is positive at pH
lower than 6.5 due to the protonation of amino groups (Anal *et al*., 2008). The
isoelectric points of silica–chitosan hybrid materials synthesized at pH 2, 3, and 4
were 4.74, 4.90, and 5.76, respectively. This observation indicated that both chitosan
and silicate species existed on the surface of silica–chitosan hybrid materials; and the
amount of chitosan molecules on the surface was increased with increasing pH values.
At pH 5 and 6, the zeta potentials were positive throughout the analysis pH range,
indicating that the surface of silica–chitosan hybrid materials was fully adsorbed by
chitosan molecules. It could be suggested that the core-shell structure of the fully
encapsulated silicas by chitosan molecules were formed with the products synthesized
at pH 5 and 6. The illustration of the silica/chitosan composite at different pH values
is shown in Figure 29.

pH 2

pH 3

Chitosan molecules

pH 4

pH 5

Silica cluster

pH 6

pH of solution   Silica/chitosan composites
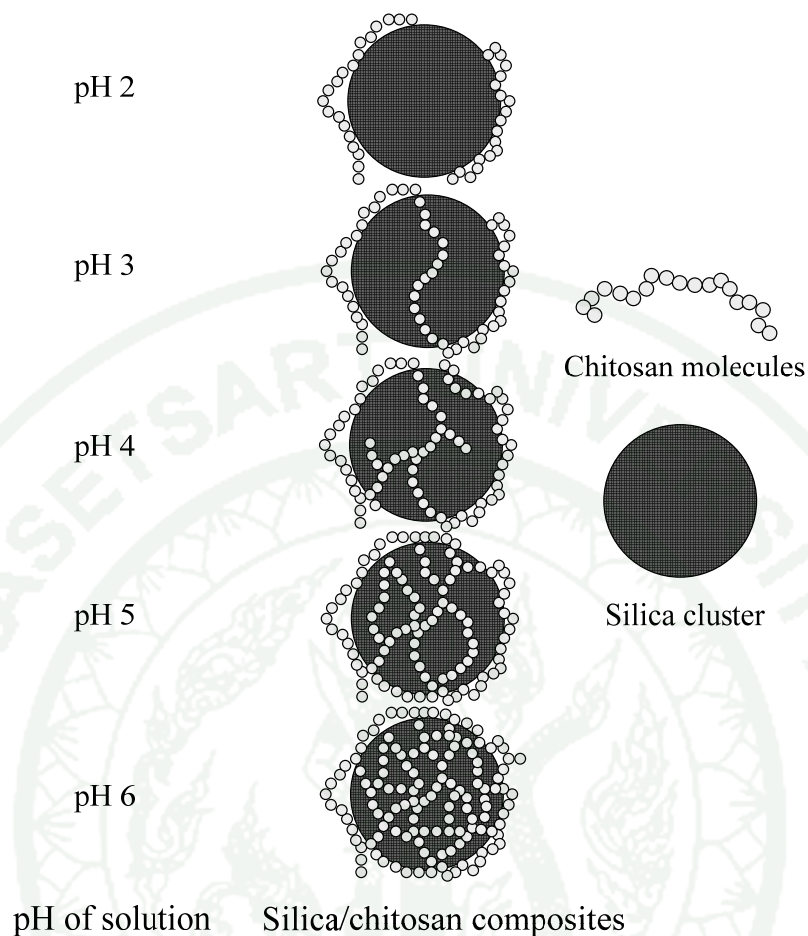
Figure 29 Illustration of the silica-chitosan composite synthesized at pH 2-6.

The TGA analysis was performed to investigate the amount of chitosan incorporated in the silica matrix. Generally, the silica surface consists of silanol groups as a result of the condensation–polymerization reaction of $Si(OH)_4$ (Iler, 1979). These silanol groups can easily adsorb water and are readily removed by heating at 120 ^oC. Further heating gives a weight loss which has been ascribed to the loss of water by the condensation of single, geminal, and vicinal silanols (Iler, 1979). In order to identify the amount of weight losses occurred from the condensation of silanol groups or the decomposition of chitosan, porous silica products (silica xerogel) were also synthesized without chitosan addition at different pH values and used as the reference information.

TGA pattern of silica–chitosan composites and silica xerogels are shown in Figure 30. The TGA patterns of silica xerogels consisted of three steps of weight losses at the temperature below 100 ^{o}C, between 100 and 200 ^{o}C, and above 200 ^{o}C. The first and the second steps were attributed to physically adsorbed and chemically adsorbed water, respectively. The last step (above 200 ^{o}C) was attributed to the condensation of silanol groups. The weight loss during the condensation of silanol groups was decreased from 4.8 to 3.1% when the pH value was increased from pH 2 to 6. At the higher pH value, the silicate condensation reaction was dominant (Brinker and Scherer, 1990), resulting in the decrease of the amount of silanol groups. The TGA patterns of silica–chitosan composites showed three steps of weight losses for the products synthesized at pH 2–4 and four steps of weight losses for the products synthesized at pH 5 and 6. The first and second steps were similar to those of silica xerogel. The weight loss above 200 ^{o}C was increased from 6.7 to 34.5% with increasing the pH value of mixture. As a result, the amount of chitosan degradation in the composite materials could be roughly estimated from the different in weight loss between silica–chitosan composite and silica xerogel.

Although the same amount of chitosan-silica ratio was used in the preparation stage, the amount of chitosan degradation was increased with increasing the pH of solution. This phenomenon could be explained through the interaction between positively charged NH_3^+ and negatively charged silica oligomers. At pH 2, positive charges of chitosan were dominant whereas the charge of silicate was close to zero, resulting in a high degree of chitosan swelling and low crosslinking between chitosan and silicate. Therefore, the chitosan template was mainly removed during the washing stage. On the other hand, with increasing the pH of mixture, the protonation of chitosan was decreased; meanwhile the charge of silicate was negative. Therefore, the stronger interactions between silicate species and chitosan were formed. As a result, greater amounts of chitosan remained in the silica/chitosan composites and were removed during the calcination process.
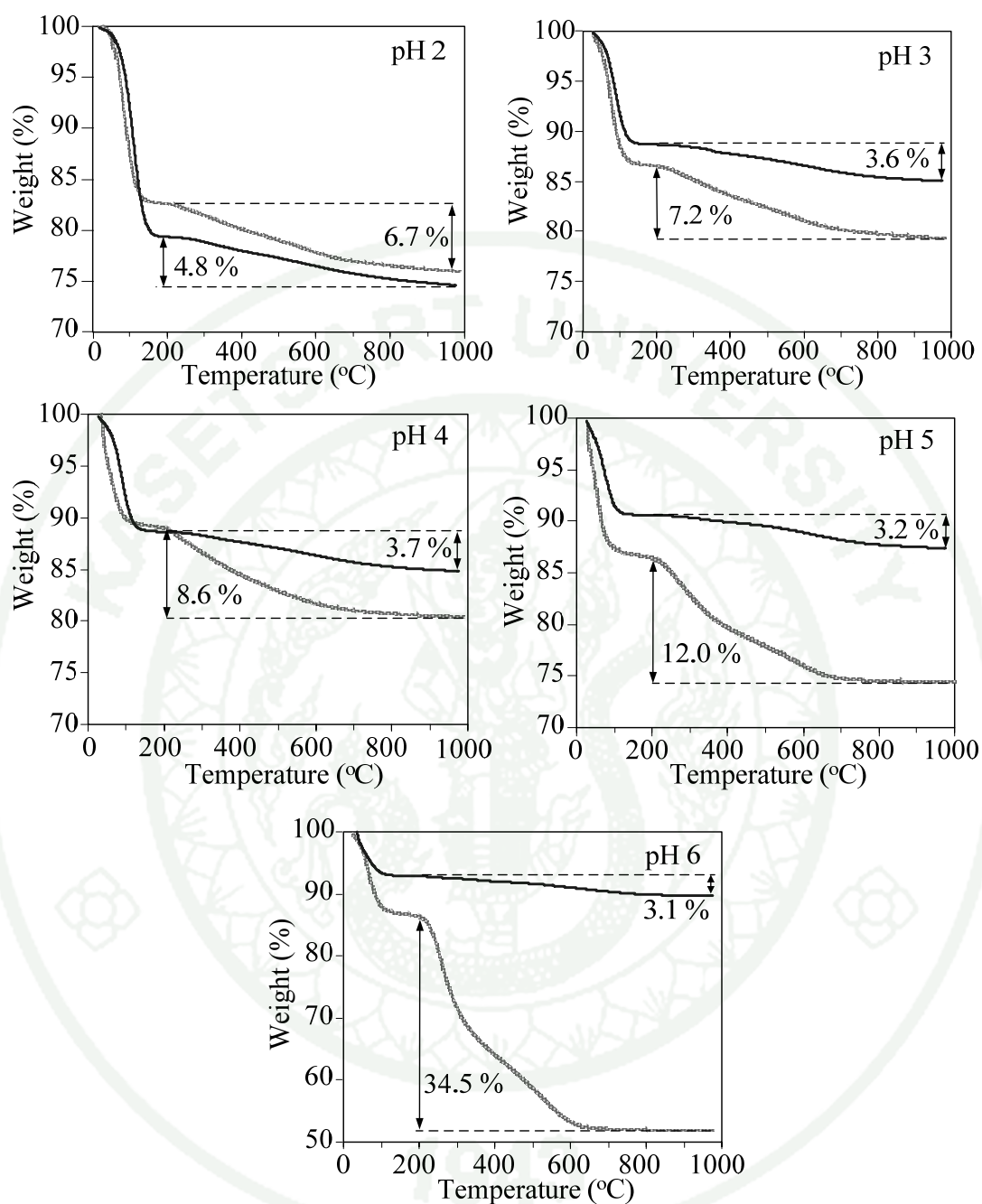
Figure 30 TGA patterns of the silica-chitosan composite (dot line) and silica
xerogels (solid line) synthesized at pH 2-6.

After calcination process, the physical properties including pore size distribution, BET surface area, pore volume, surface morphology and aggregates of silica nanoparticles of porous silica products synthesized without and with chitosan at pH 2-6 were examined.

The N_2-sorption isotherms of the porous silica products synthesized without and with chitosan template at various pH values are shown in Figure 31. Without chitosan template, the microporous silica of type I isotherm was observed at pH 2 (P-2). The sorption isotherm changed to type IV with H2 hysteresis loop for the products synthesized at pH 3-6 (P-3, P-4, P-5 and P-6), indicating the existence of mesoporous structure. Moreover, it can be clearly observed that the capillary condensation steps shifted to higher relative pressures when increasing the pH values due to the increase in the mean pore size of silica products.

Figure 31 N_2-sorption isotherm of porous silica products synthesized (a) without and (b) with chitosan at pH 2-6, designated as P-x and C-x where x is the pH value.

Comparing to the products synthesized without chitosan template, the type I-IV composite isotherms were found for the silica product synthesized with chitosan at pH 2 (C-2), indicating the characteristics of microporous-mesoporous materials. For the products synthesized at pH values of 3-6 (C-3, C-4, C-5 and C-6), the isotherms exhibited two well-defined adsorption steps. The first adsorption step at the intermediate relative pressure (0.5 > P/P0 > 0.9) was the characteristics of type IV isotherm, representing the existence of the capillary condensation of nitrogen gas inside the inter-particle mesopores. Similar to the products synthesized without the chitosan template, the capillary condensation steps also shifted to a higher relative pressure when increasing the pH values. The second adsorption step at a high relative pressure (P/P0 > 0.9) was the characteristics of type II isotherm, corresponding to the adsorption of liquid nitrogen on the large inter-particle voids or macropores.
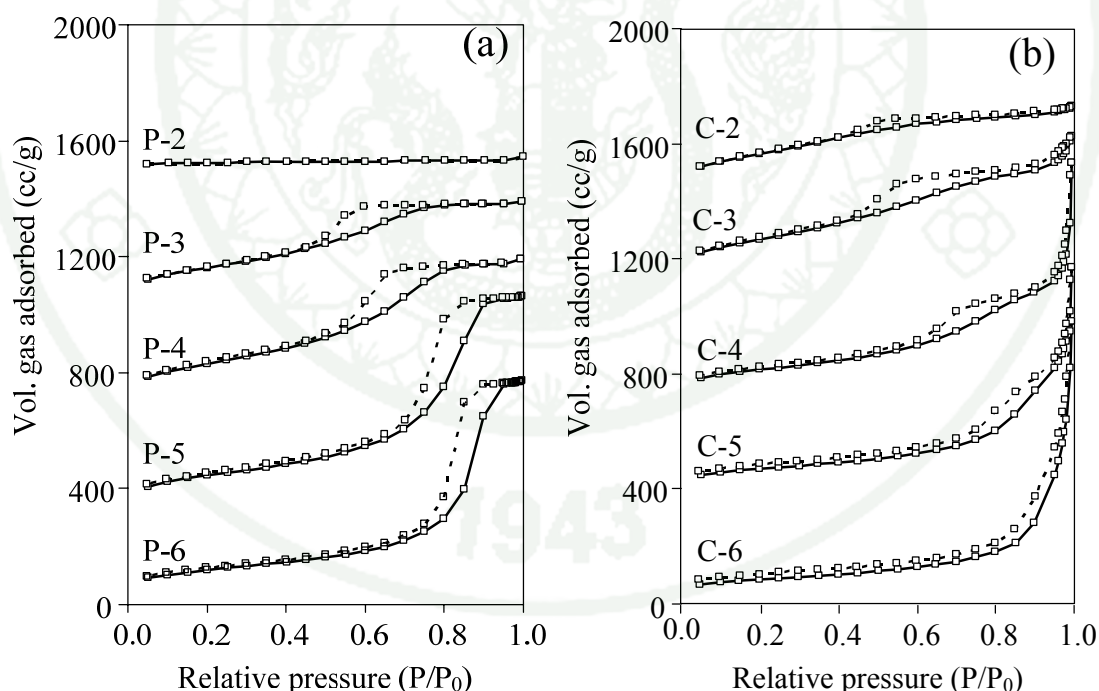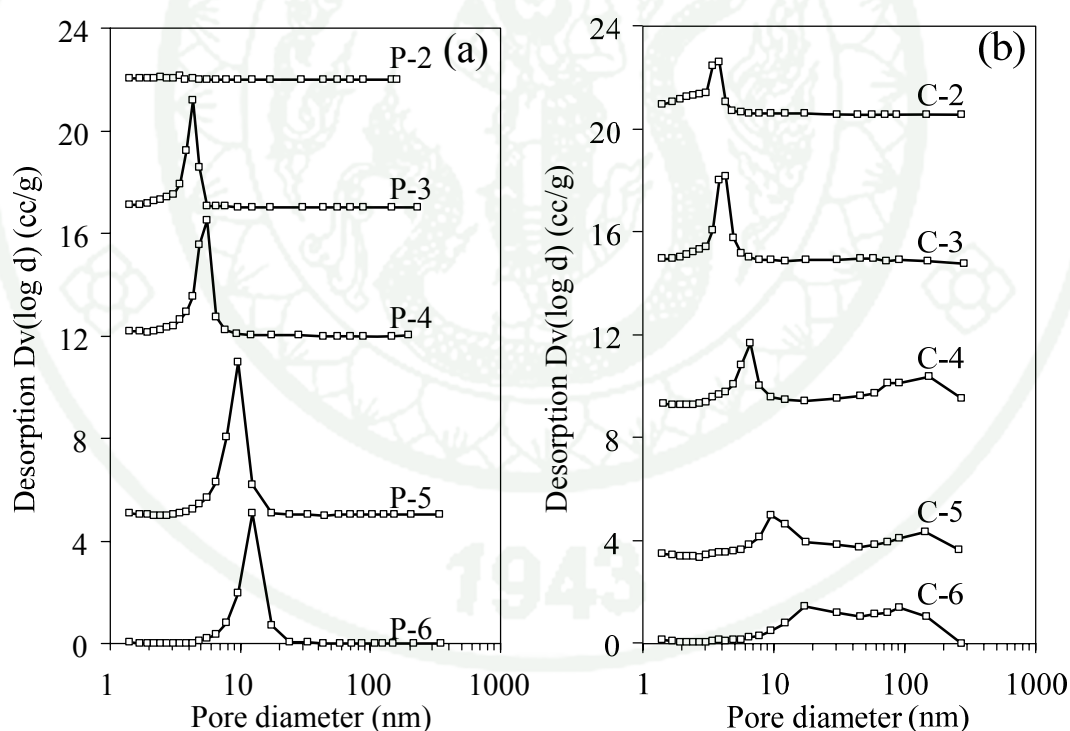

Figure 32 Pore size distribution of porous silica products synthesized (a) without and (b) with chitosan at pH 2-6, designated as P-x and C-x where x is the pH value.

As shown in Figure 32, the template-free porous silicas exhibited the monomodal pore size distribution of which became broader as the pH value was increased. The mean pore sizes gradually shifted from 3.4 to 12.4 nm when the pH value was increased from 2 to 6. On the contrary, the porous silicas synthesized with the chitosan template showed the bimodal pore size distribution (mesopore-macropore) at pH values higher than 2.

The BET surface area, BJH pore diameter and pore volume of the porous silica products prepared without and with the chitosan template at various pH values are shown in Table 5. Without chitosan template, the BJH pore diameter and pore volume of the porous silica products were increased with increasing pH values while the BET surface area was gradually decreased, except that of pH 2. With chitosan template, the similar trend of the BET surface area was observed, however the markedly higher total pore volume compared to those prepared without chitosan template were obtained (approximately 21-40% and 74-80%, respectively at pH 5-6).

In order to examine the thermal stability, the porous silica products were calcined at 800 $^{\circ}$C, the results of their physical properties are also given in Table 5. The BET surface area and total pore volume of all porous silica products were decreased with increasing the calcination temperature especially porous silica synthesized without chitosan at pH 2 (P-2). The BET surface area and the total pore volume of P-2 decreased from 620 to 43 m^2/g and 0.47 to 0.05 cm^3/g, respectively. The isotherm of P-2 (Figure 31) indicated that the structure of P-2 mainly composed of micropores occurred by the linear chains of silica oligomers (Brinker and Scherer, 1990). Therefore, the sintering and the collapsing of their structure can easily occurred during the calcination at 800 $^{\circ}$C. On the other hand, the isotherm of C-2 (Figure 31) was composite isotherms between micropores and mesopores. The mesopore channels would provide the longer distance between the silica nanoparticles which could reduce the sintering effect. The greater thermal stability of chitosan-templated porous silica synthesized at other pH values can be explained similarly.

Table 5 Physical properties of porous silica products prepared without and with the chitosan template at various pH values of mixture.

Sample [a]	BET surface area (m²/g)		Mean pore diameter (nm)		Total pore volume (cm³/g)	
	A	B	A	B	A	B
P-2	620	43	3.4	3.4	0.47	0.05
P-3	630	467	4.3	4.3	0.58	0.54
P-4	611	410	5.6	5.6	0.82	0.65
P-5	400	325	7.8	7.8	1.01	0.78
P-6	-	235	-	12.4	-	0.95
C-2	668	588	3.8	3.8	0.58	0.65
C-3	602	489	4.3	4.3	1.08	0.98
C-4	489	421	6.5	6.5	1.29	1.09
C-5	350	330	9.5	9.5	1.36	1.23
C-6	-	220	-	17.5	-	1.56

[a] The samples were calcined at 600 °C (A) and 800 °C (B).

SEM micrographs of the products prepared without chitosan template at pH 2, 3 and 5 are shown in Figures 33 (a-c), respectively. The silica xerogels with dense surface caused by an agglomeration of fine silica nanoparticles were formed, and these nanoparticles became larger when the pH value of solution was increased. The porous silica products with different surface morphologies were obtained when synthesized with chitosan template at various pH values (Figure 33(d)). At pH 2, two different structures including the densely-packed (circle) and the loosely-packed aggregates of silica nanoparticles were found. At pH 3, the macroporosity was slightly formed as the inter-particle voids of silica clusters (Figure 33(e)). The bimodal pores of interconnected nanoparticles clusters and macropores were entirely formed in the pH range of 4-6 (Figures 33(f-h)). The silica cluster size (smaller than 1 micron) was constantly decreased with increasing the pH values.

Figure 33 SEM micrographs of porous silica products synthesized without (P) and
with chitosan template (C) at various pH values. (a) P-2, (b) P-3, (c) P-5,
(d) C-2, (e) C-3, (f) C-4, (g) C-5, and (h) C-6.

This observation corresponds to the amount of chitosan degradation observed by TGA analysis. The chitosan molecules could incorporate into the silica framework and controlled the growth of silica clusters. The larger amount of incorporated chitosan template led to the formation of porous silica product with smaller cluster size.

TEM images of the porous silica products synthesized without and with chitosan template are shown in Figure 34. Similar to the results of the pore size distribution (Figure 32), the mean pore size of the porous silica products was increased with increasing the pH values. Without the chitosan template, the interparticle, connected wormhole-like mesoporous structures formed by an agglomeration of silica nanoparticles were observed (Figures 34(a-c)). With chitosan template, the uniform wormhole-like, monomodal mesoporous silica was synthesized at pH 2 (Figure 34(d)), while the bimodal porous silicas consisted of the wormhole-like mesopores formed by the primary agglomeration of silica nanoparticles, and the macropores resulting from the cluster-cluster aggregation were synthesized at pH 3-6 (Figures 34(e-h)). It should be noted that the silica cluster size decreased while the amount of macropores increased when increasing the pH values from 3-6.
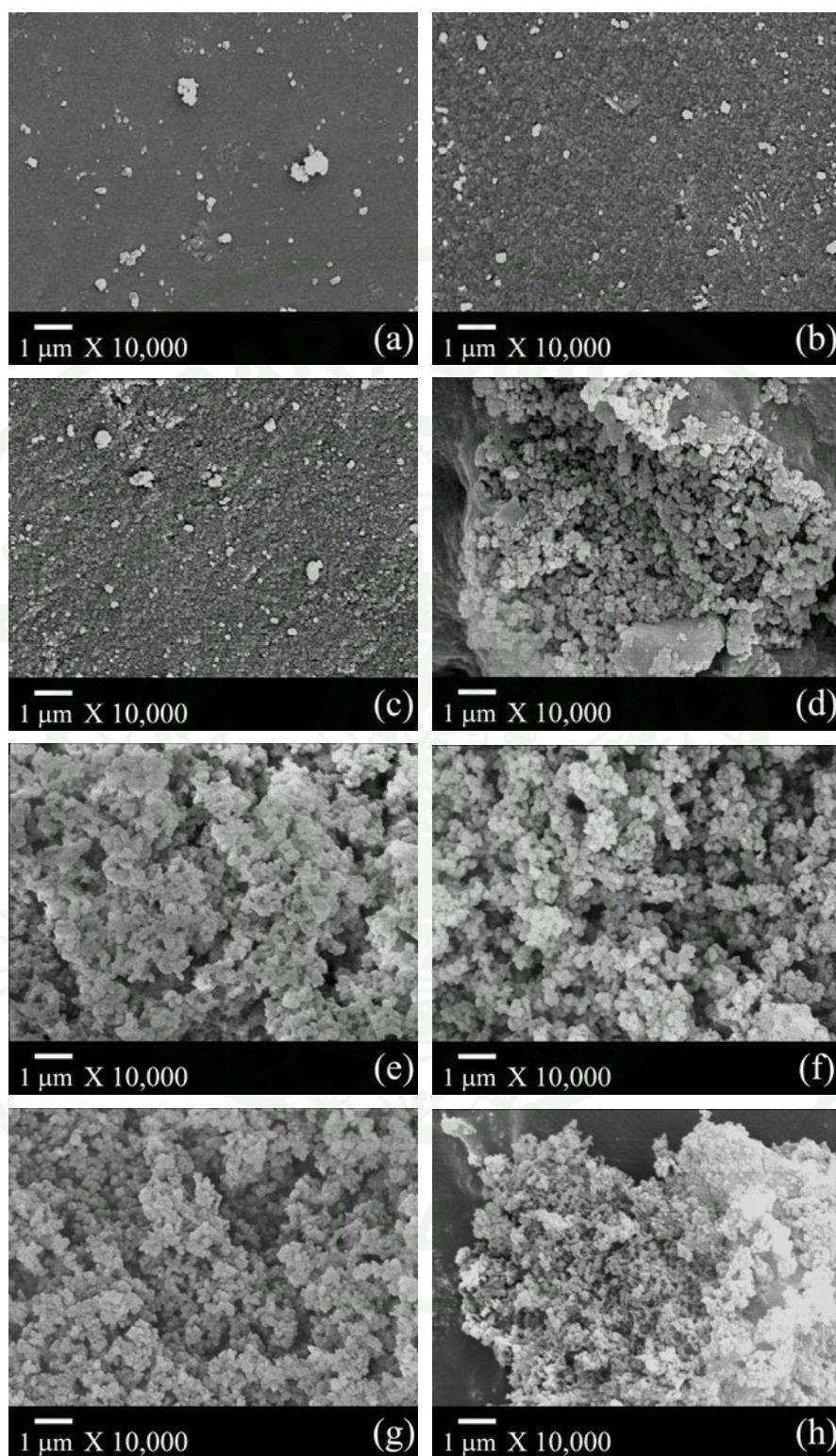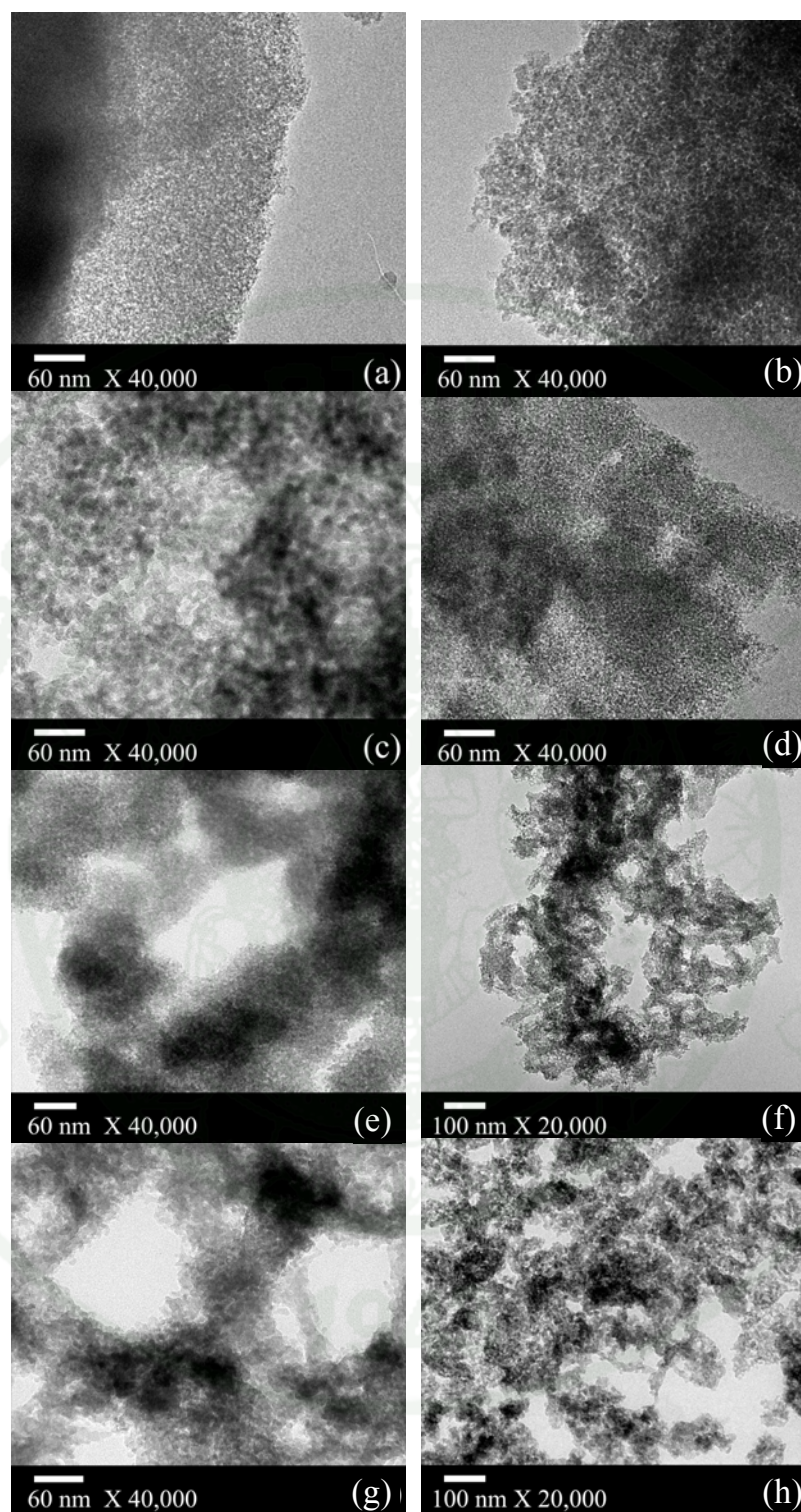
Figure 34 TEM micrographs of porous silica products synthesized without (P) and
with chitosan template (C) at various pH values. (a) P-3, (b) P-4, (c) P-6,
(d) C-2, (e) C-3, (f) C-4, (g) C-5 and (h) C-6.

The proposed formation mechanisms of the porous silica products synthesized without and with chitosan template are shown in Figure 35. Without chitosan template, silica sols are formed as the result of the hydrolysis-condensation reaction of sodium silicate solution. After that, these sols are stick together in such a way as to form a framework of silica gels when the attractive dispersion forces are greater than the repulsive forces. During the drying process, pore liquids are removed, resulting in the shrinkage of the gel framework and silica xerogel is formed. The particle size, which depended on the pH of mixture, and packing geometry greatly affects the porous structure of silica products. The aggregate silica particles of very small size are obtained at pH 2 due to the relatively low solubility and condensation rate of silica precursors (Brinker and Scherer, 1990). The wormhole-like micropores of silica products are formed as the interparticle channels between each nonporous silica particles. When the pH of mixture is increased, the solubility and condensation rate are gradually increased, whereas the hydrolysis rate approaches a minimum at an approximately neutral pH. Under this condition, the larger silica particles are formed and therefore, the larger interparticle channels than those of the porous silica synthesized at pH 2 are obtained, resulting in the mesoporosity of silica products.

With chitosan template, the conformation of chitosan chains in the aqueous solution strongly depends on the pH of mixture (Berger *et al*., 2004). At low pH, chitosan chains are dispersed by an electric repulsion according to the high protonation of their amino groups. After adding the sodium silicate solution into the chitosan solution, similar to that of the template-free porous silica preparation, silica sols and then silica gels are formed in sequence. Under this condition, the weak interactions between chitosan and silica species are observed due to high positive charges of chitosan and nearly zero charges of silicate species. As a result, chitosan chains were mainly excluded from silica nanoparticles rather than incorporating into the silica framework. Therefore, chitosan template is easily removed during the washing stage; accordingly the chitosan-templated porous silica products consisted of micropores and mesopores are formed.

When the pH of mixture is increased, the protonation of chitosan is decreased meanwhile the charge of silicate is negative. The chitosan structure becomes aggregate and stronger interactions between chitosan and silica species are formed, resulting in the more chitosan incorporating into the silica framework and remaining after the washing stage. After the calcination process, the chitosan-templated porous silica products consisted of mesopores caused by the agglomeration of the silica nanoparticles and macropores caused by the template removal are formed.
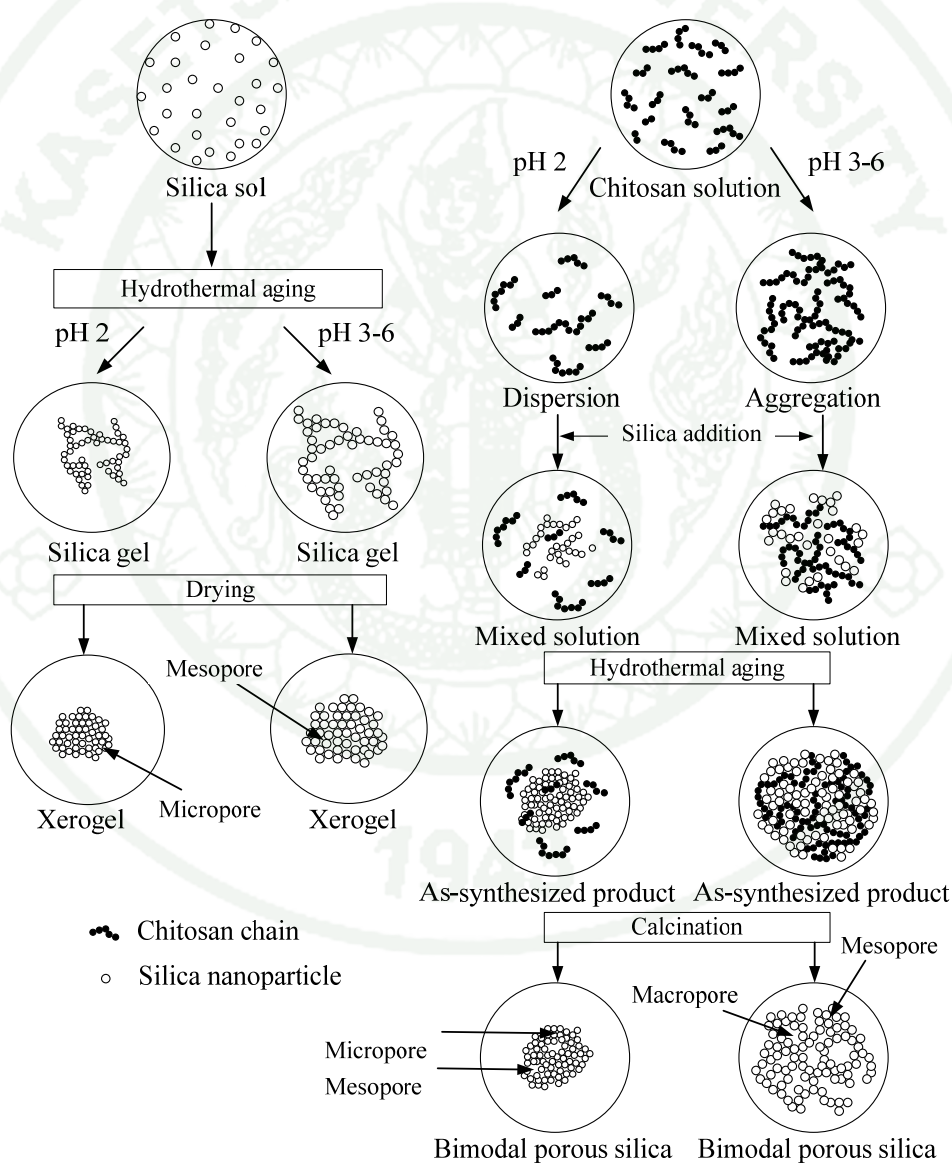
Figure 35 Schematic illustration of the formation of porous silica products synthesized without and with chitosan template at various pH values.

The results above showed that chitosan has significant potential as the template for the formation of silica macroporosity by incorporating into the silica framework. Moreover, chitosan could restrict the growth of the silica cluster. It can be clearly seen that the macropore could easily form at pH value of 6 due to the dense aggregates of chitosan chains and the strong interaction between positively charged NH_3^+ of chitosan chains and negatively charged of silica oligomers. However, at pH 6, the mesopore diameter was too large (12-17 nm) and the surface area was relatively low. Such material might not be suitable for applications as the catalyst support which required very high specific surface area. To overcome this limitation, the effect of chitosan/silica ratio and aging temperature were then carefully investigated at pH 6.

2. Effect of Chitosan/Silica Ratio and Aging Temperature

Figure 36 presents nitrogen adsorption-desorption isotherms of porous silica products synthesized at different chitosan/silica ratios and aging temperatures. Without chitosan template, the porous silica products exhibited type IV isotherm with H2 hysteresis loop, indicating that the products composed of mesopores with ink-bottle structure. In addition, it can be clearly observed that the hysteresis loop shifted to higher relative pressures when increasing the aging temperature, this was due to the increase of the mean pore diameter of silica products.

When chitosan template was applied, the characteristics of meso-macroporous materials of different chitosan/silica ratios and aging temperatures revealed type IV-II composite isotherms except that the only type IV isotherm was observed for CS1.6-40. Moreover, the isotherms of porous silica products synthesized with chitosan displayed H3 hysteresis loop, attributing to an aggregation of silica nanoparticles as the loosely silica cluster. Consequently, the porous silica products with slit-shaped pores were obtained, indicating the influence of chitosan template on the textural properties of the silica clusters aggregates.

The pore size distribution calculated from both adsorption and desorption branches of porous silica products synthesized at various conditions are shown in Figure 37. Without chitosan template, pore size distribution patterns of adsorption and desorption branches of CS0-40, CS0-60 and CS0-80 products were markedly different. The pore size distribution calculated from adsorption branches were much broader than those of desorption branches. It was due to the fact that the amount of nitrogen gas condensed and remained in the pores would give rise to the pore blocking (Gregg and Sing 1982). In contrast, insignificant difference of pore size distributions between adsorption and desorption branches of porous silica products synthesized with chitosan template was observed, this may be attributed to the shorter pore length resulting by smaller silica cluster sizes. This evidence will be confirmed later by TEM analysis.

The porous silica products synthesized without chitosan (Figure 37) showed a narrow pore size distribution. The mean BJH pore diameter was increased with increasing the aging temperature. With chitosan template, the porous silica products exhibited the pore size distribution in two different length scales including mesopore and macropore diameter regions (Figure 37). The mesopore diameter also increased with an increase of aging temperature which was similar to the products synthesized without chitosan. However, the lower intensity and broader pore size distribution were observed. This could be attributed to the dissimilarity of the growth of silica nanoparticles caused by the addition of chitosan template.

The interaction of amino-containing peptides with sodium silicate was investigated by Coradin et al.(2002). They found that the distribution of positively charged NH_3^+ along the peptide chain could bring negatively charged silica oligomers close enough for each other to form the condensation reaction. On the other hand, several literatures reported that polymers containing cationic charge were possibly entrapped in the colloidal silica matrix which could not only reduce number of available silanol groups but also prevent further condensation reaction (Demadis *et. al.*, 2009), resulting in the formation of smaller silica nanoparticles. According to our present work, the pore size of porous silica products synthesized with chitosan template were distributed at lower pore diameter region, implying that the latter should dominate to form smaller silica nanoparticles. The broader pore size distribution could be attributed to the growth of silica nanoparticles in different phases. This result will be explained through the phase separation phenomena and confirmed later by representative high resolution TEM images.
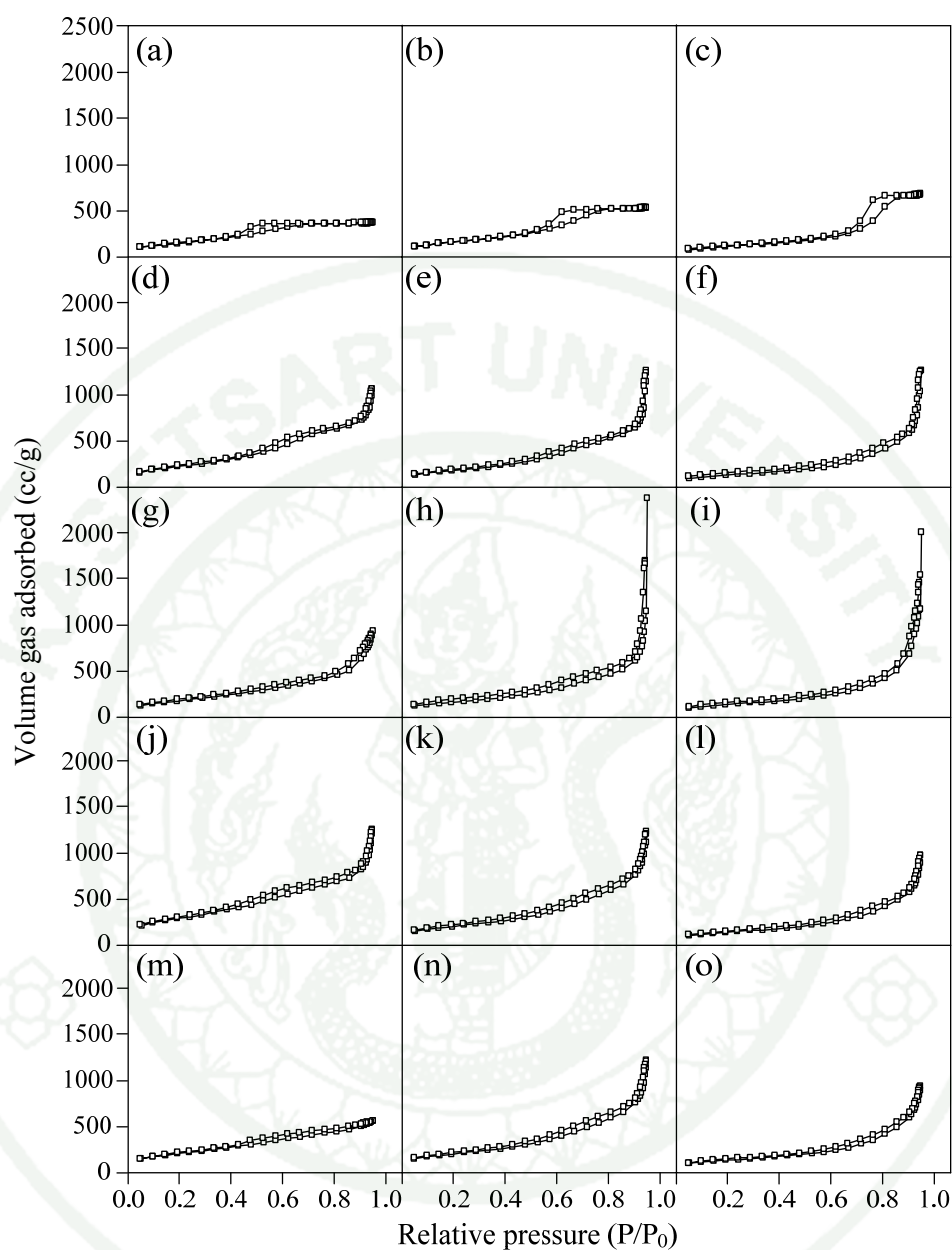
Figure 36 N_2 adsorption-desorption isotherms of porous silica products synthesized
at different chitosan/silica ratios and aging temperatures:
(a) CS0-40; (b) CS0-60; (c) CS0-80; (d) CS0.1-40; (e) CS0.1-60;
(f) CS0.1-80; (g) CS0.4-40; (h) CS0.4-60; (i) CS0.4-80; (j) CS0.8-40;
(k) CS0.8-60; (l) CS0.8-80; (m) CS1.6-40; (n) CS1.6-60; and (o) CS1.6-80.

Figure 37 Pore size distribution of porous silica products synthesized at different

chitosan/silica ratios and aging temperatures:

(a) CS0-40; (b) CS0-60; (c) CS0-80; (d) CS0.1-40; (e) CS0.1-60;

(f) CS0.1-80; (g) CS0.4-40; (h) CS0.4-60; (i) CS0.4-80; (j) CS0.8-40;

(k) CS0.8-60; (l) CS0.8-80; (m) CS1.6-40; (n) CS1.6-60; and (o) CS1.6-80.
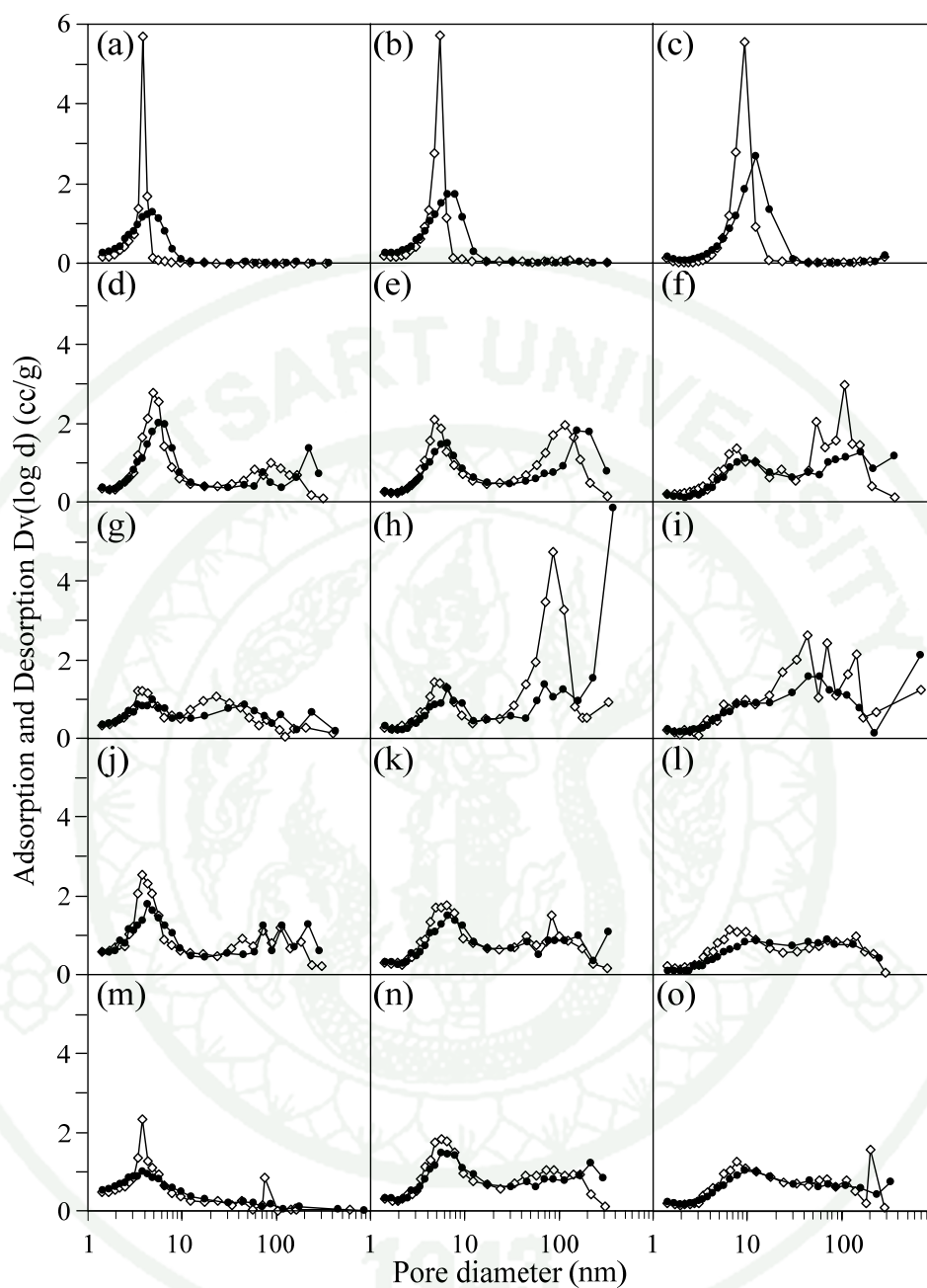
The BET surface area, mean BJH pore diameter and total pore volume of all porous silica products synthesized at different chitosan/silica ratios and aging temperatures are summarized in Table 6. It can be clearly seen that the BET surface area of all products was decreased with increasing the aging temperature. Also shown are the BET surface area and total pore volume of porous silica products synthesized with chitosan template, which were significantly larger than those synthesized without chitosan. The highest total pore volume of 3.69 cc/g was obtained with the chitosan/silica ratio of 0.4 at the aging temperature of 60 $^{\circ}$C.

Table 6 Physical properties of products synthesized under different chitosan/silica ratios and aging temperatures.

Sample ID	BET surface area (m^2/g)	Mean BJH pore diameter (nm)	Macropore diameter (nm)	Total pore volume (cc/g)
CS0-40	625	5.1	-	0.57
CS0-60	595	7.9	-	0.83
CS0-80	428	12.5	-	1.07
CS0.1-40	797	5.4	50-250	1.64
CS0.1-60	640	5.0	50-250	1.96
CS0.1-80	449	9.5	50-250	1.96
CS0.4-40	669	4.9	20-100	1.46
CS0.4-60	598	7.0	40-250	3.69
CS0.4-80	498	9.5	30-250	3.12
CS0.8-40	1054	4.3	60-250	1.96
CS0.8-60	727	7.0	40-250	1.93
CS0.8-80	349	12.5	40-250	1.41
CS1.6-40	760	5.8	-	0.89
CS1.6-60	727	5.5	40-250	1.92
CS1.6-80	480	9.5	40-250	1.48

The aggregated characteristics and morphologies of the porous silica products were investigated by TEM and SEM, and representative images are shown in Figures 38 and 39, respectively. Since the interrelated effect between chitosan/silica ratio and aging temperature on the aggregated and morphological characteristics of the porous silica products are clearly observed, therefore the effect of these parameters are discussed simultaneously. It was clearly seen that the porous silica product synthesized without chitosan template (Figure 38(a)) showed a highly dense and extremely large silica cluster built up from the aggregation of silica nanoparticles. In contrast to the porous silica synthesized without chitosan template, the porous silicas synthesized with chitosan template revealed loose aggregation (Figure 38(b-i)). These structures could potentially diminish the effect of pore blocking as mentioned in the pore size distribution results.

At the chitosan/silica ratio of 0.1 and the aging temperature of 40 ^{o}C (Figure 39(a)), the spherical porous silica product with high order of aggregation in submicron diameter range (100-200 nm) was synthesized. With increasing the aging temperature, the smaller spherical particles with lower degree of aggregation were observed (Figures 39(b-c)).

At the chitosan/silica ratio of 0.4, the highly aggregated spherical porous silica product of different submicron size ranges (<100 nm) could be observed at the aging temperature of 40 ^{o}C (Figure 39(d)). At higher temperature (Figure 39(e)), the self-agglomerate interconnected porous silica with uniform skeleton size was observed. The structure of the porous silica product obtained at 80 ^{o}C (Figure 39(f)) was composed of the interconnected silica clusters, the sub-micrometer spherical aggregates, and the isolated pores (observed by TEM).

At the chitosan/silica ratio of 0.8, the aggregation of large silica clusters ranged from 200-300 nm was observed at the aging temperature of 40 ^{o}C (Figure 39(g)). The silica cluster size was decreased with increasing the aging temperature (Figures 30(h-i)); however the cluster size was still larger when compared to the silica skeleton of porous silica products prepared at lower chitosan/silica ratio.

At the chitosan/silica ratio of 1.6, two different morphologies composed of the dense aggregation of silica nanoparticles, which was similar to that of template-free porous silica, and the aggregation of submicron silica product were observed at 40 ^{o}C (Figure 39(j)). At higher temperature (Figures 39(k-l)), the dense aggregation of silica nanoparticles disappeared and only the smaller silica clusters were found.

Figure 38 TEM micrographs of porous silica products synthesized at various chitosan/silica ratios and aging temperatures (low magnification): (a) CS0-60; (b) CS0.1-60; (c) CS0.4-60; (d) CS0.8-60; (e) CS0.8-80; (f) CS0.4-80; (g) CS0.4-80; and (h) CS1.6-80.
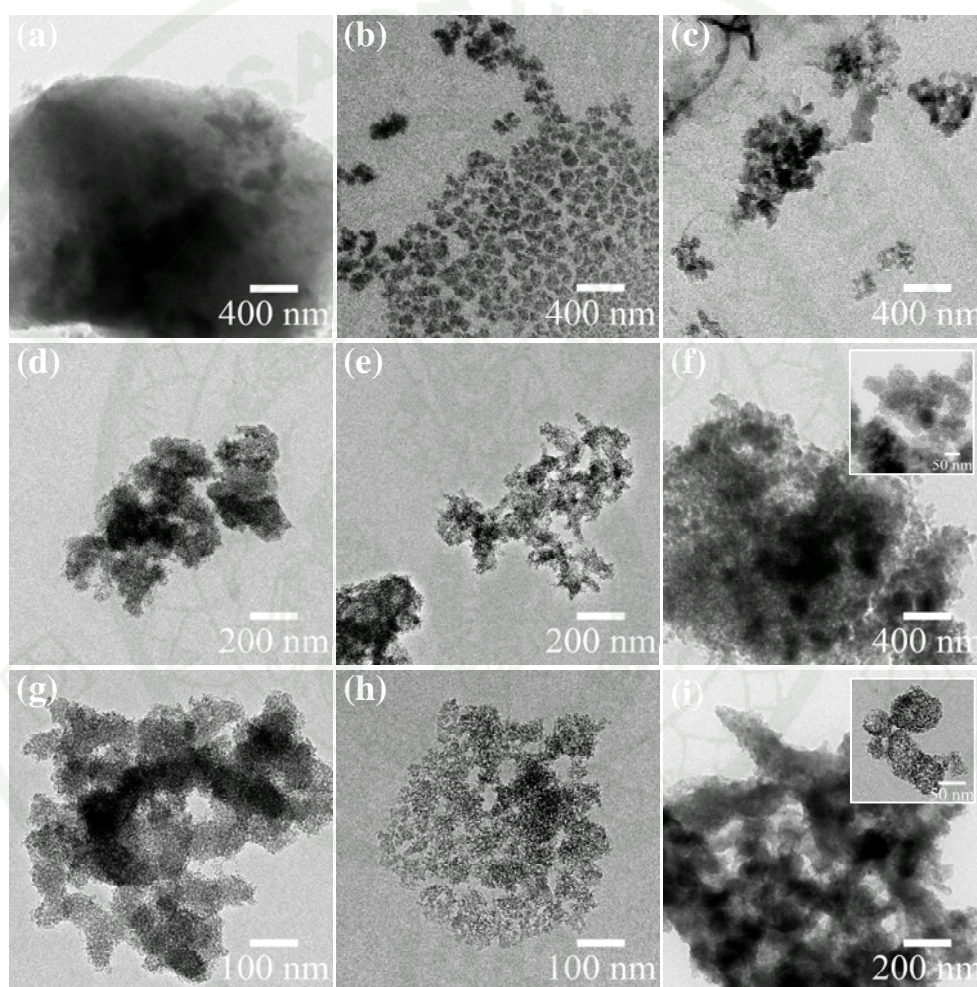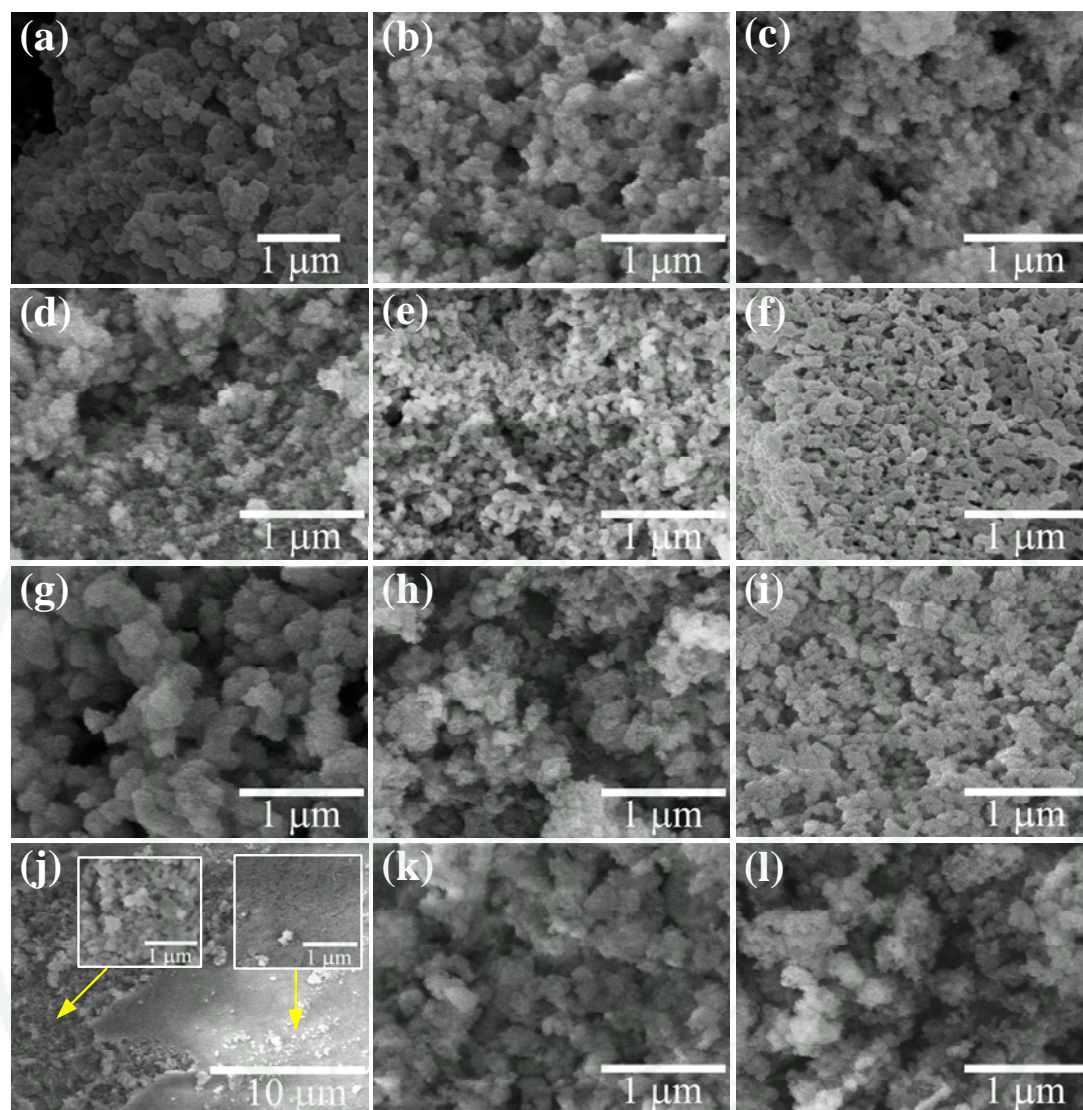
Figure 39 SEM micrographs of porous silica products synthesized at various chitosan/silica ratios and aging temperatures:
(a) CS0.1-40; (b) CS0.1-60; (c) CS0.1-80; (d) CS0.4-40; (e) CS0.4-60; (f) CS0.4-80; (g) CS0.8-40; (h) CS0.8-60; (i) CS0.8-80; (j) CS1.6-40; (k) CS1.6-60 and (l) CS1.6-80.

These variations in the surface morphology could be clearly explained by the phase separation phenomena elegantly described by Nakanishi (1997). These phenomena occurred by the interaction among silica, polymer and solvent, and were classified into two categories consisting of weak and strong attractive interactions between silica and polymer. In the former system, the separation took place in the silica-rich phase and the polymer-rich phase with the solvent being distributed in both phases. In the latter system, the strong interaction between polymer and silica through hydrogen bond could promote the formation of silica-polymer rich phase and solvent became a major component of the other phase. Once the phase separation occurred, the various transient structures of phase separation could be maintained as a metastable gel phase, depending on the time relation between the onset of phase separation and gel formation. It should be noted that all our products were prepared through the hydrolysis-condensation at low temperature (40 ^{o}C) for 24 h and followed by aging process at the temperatures between 40 ^{o}C and 80 ^{o}C for another 24 h. Therefore, the final product structure significantly depended on the obtained structure before aging process.

At the aging temperature of 40 ^{o}C and the chitosan/silica ratio of 0.1-0.4, phase separation performed as the result of the strong attractive interactions of hydrogen bonding and electrostatic interaction. Considering the time-consuming gelation process occurred at low reaction temperature, the transient structure was maintained in a relatively later stage of the phase separation process. As a result, the particle (silica cluster) aggregates were formed. The decrease of silica cluster size with increasing chitosan/silica ratio was caused by the distribution of silica in a highly dense chitosan network of which limiting the growth of silica cluster.

If the strong attractive interaction continuously controlled the occurrence of phase separation, the smaller silica cluster size would be formed at 40 ^{o}C with the chitosan/silica ratio of 0.8-1.6. However, it was clearly seen that the silica cluster size presented here was increased with the increase of chitosan concentration due to the fact that the amount of chitosan in the chitosan-silica rich phase was decreased at higher chitosan concentration. Since the amounts of water and acidic solution were

fixed in our experiment, the addition of large amount of chitosan molecules could reduce the free positively charge NH_3^+ that tended to decrease the interaction between positively charge NH_3^+ and silanol groups. After polymerization of silica oligomers, the silica-rich and chitosan-rich phases were formed. As a result, only small amount of chitosan incorporated into the silica-rich phase and therefore the large silica clusters were obtained.

The effect of the aging temperature could be mainly interpreted by the acceleration of gel formation. When the aging temperature was increased, the phase separation was suppressed, while the gel formation was in parallel accelerated. As mentioned above, the effect of phase separation has been encountered since the hydrolysis-condensation proceeded at 40 ^{o}C. However, the state of ultimate stability of the obtained structures was not achieved even after a prolonged coarsening process.

The increase of aging temperature could again change the metastable state by the increasing compatibility between these components. As a result, the obtained structure was changed from the cluster-aggregated structure to the inter-connected structure. Nevertheless, it was found that the cluster-aggregated structure obtained before the aging process still remained and was mixed with the inter-connected structure in the final products (Figure 38(h)). Moreover, the finer silica clusters were also obtained at higher chitosan/silica ratio when the aging temperature was increased due to the larger amount of chitosan incorporating into the silica matrix.

Figure 40 shows the morphology of silica nanoparticles and mesopore structure of the porous silica products observed by high resolution TEM. It was clearly seen that the size of silica nanoparticles was increased with increasing the aging temperature. This observation could be explained by the fact that at higher aging temperature the growth of silica nanoparticles was promoted by the simultaneous dissolution of unstable, smaller silica particles, and reformation of soluble silica on larger particles.

The TEM image of CS0.4-80 (Figure 40d) obviously revealed the silica nanoparticle of small and larger sizes; this could be attributed to the formation of silica nanoparticles in different phases practically occurred at any chitosan/silica concentrations. This observation evidently confirmed the results observed by N_2 sorption analysis (Figure 37) regarding the existence of silica nanoparticles with two different sizes, resulting in broader pore size distribution of the porous silica products synthesized with chitosan.
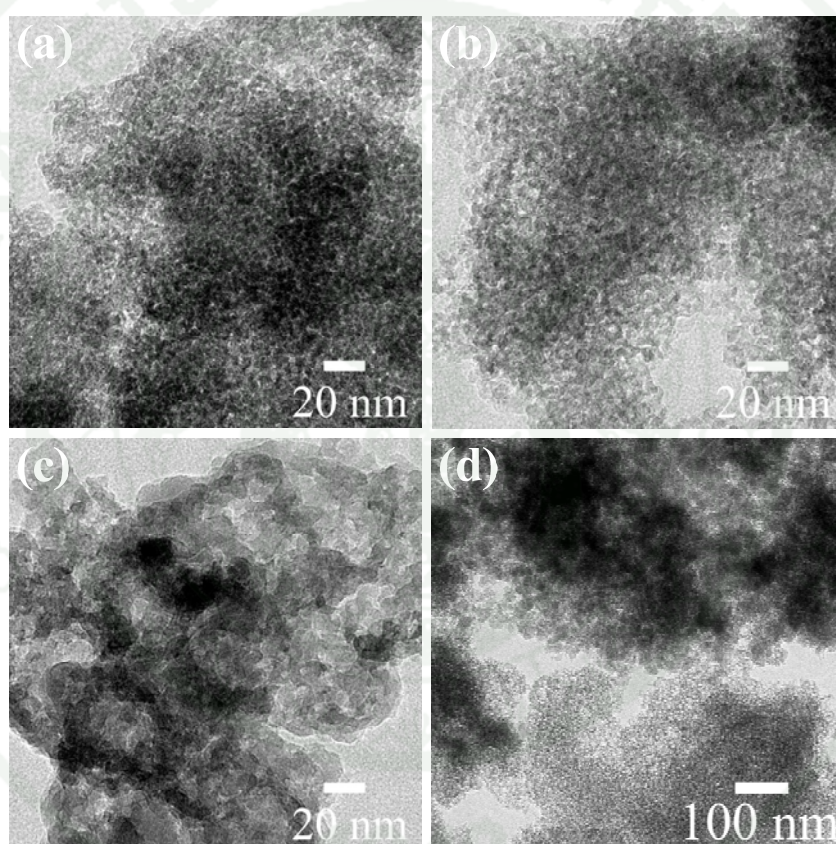

Figure 40 TEM micrographs of porous silica products synthesized at various chitosan/silica ratios and aging temperatures (high magnification): (a) CS0.4-40; (b) CS0.4-60; (c) CS0.4-80 and (d) CS0.4-80.

Synthesis of Gasoline via Fischer-Tropsch Synthesis Reaction

In this part, the characteristics of cobalt supported bimodal and monomodal porous silica catalysts denoted as Co/BS-X and CoMS-X catalysts, respectively and their catalytic performances on FTS reaction were reported. The physical and chemical properties of Co/BS-X and Co/MS-X catalysts were firstly investigated using TGA-DSC analysis, N_2-soprtion measurement, XRD analysis, TEM technique, and H_2-chemisorption measurement. After that, the activity and selectivity of different types of catalysts were discussed. Moreover, the spent Co/BS-2 and Co/MS-2 catalysts after 12 h on stream were examined for the deactivation of active metal phases and coke formation on the catalyst surfaces.

1. Physical and Chemical Properties of Catalysts

As shown in Figure 41, the TGA and DSC curves in air of impregnated Co/MS-X and Co/BS-X catalysts exhibited a two-step weight loss. The first step at the temperature below 150 ^{o}C was attributed to the evaporation of simultaneous residual moistures in the supports and water molecules in the cobalt hydrate shell. The second step at the temperature between 150 and 210 ^{o}C was the decomposition of cobalt nitrate. It should be noted that the same weight losses of each catalysts were observed at this stage, indicating that the equal amount of cobalt nitrate was decomposed. After 210 ^{o}C, the weight remained constant. This result confirmed that the calcination temperature at 400 ^{o}C was suitable to remove hydrate and bound waters, and counter ions presented in the catalysts.

The heat flow patterns revealed the endothermic decomposition of cobalt nitrate of all the supports (Figure 41(b)). The decomposition temperature of cobalt nitrate was decreased with increasing the mesopore diameter in each series of catalysts, indicating the decrease of interactions between cobalt nitrate and the supports. This can be attributed to the fact that the support with small pore diameter and high surface area consisted of larger amount of silanol group of which could react with nitrate ion and/or cobalt ion to form the compounds that decomposed at higher

temperature. Moreover, part of nitrate ions might be trapped within the silica micropore structure (Nissinen *et. al*., 2005) and therefore the existence of macropore could provide a new pathway that reduced the distance of heat transfer to supply the decomposition of cobalt nitrate entrapped into the pores.
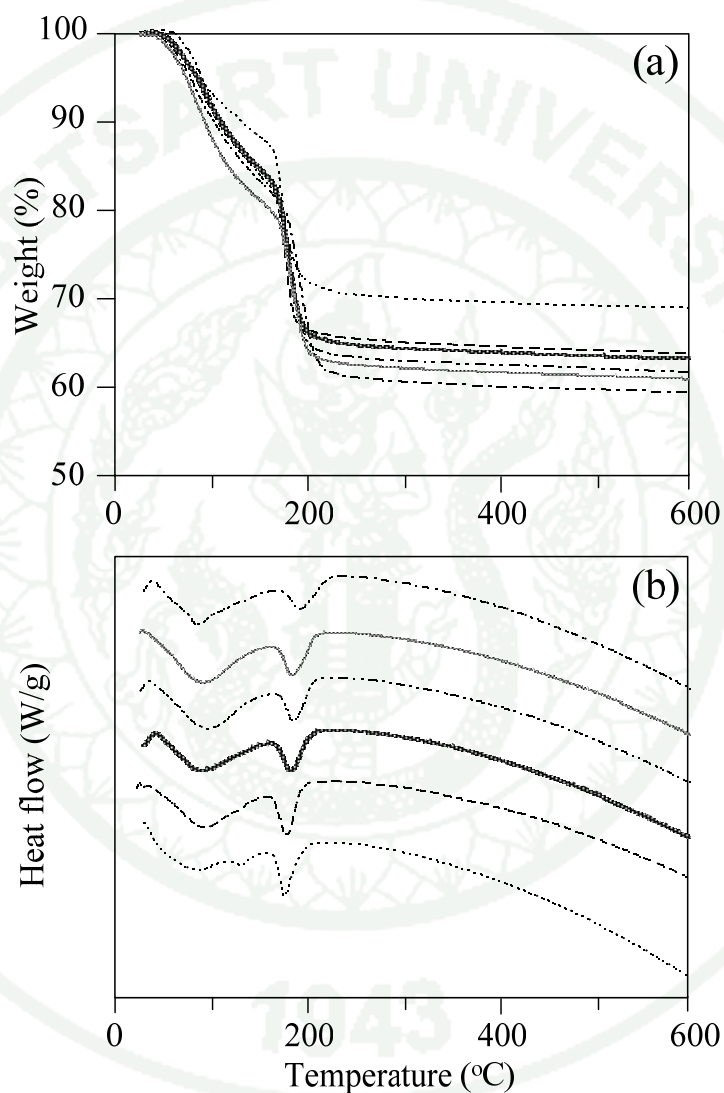
Figure 41 TGA (a) and DSC (b) curves of bimodal and monomodal porous silica
supported cobalt nitrate: Co/BS-1 ════ ; Co/BS-2 ▦ ;
Co/BS-3 ·····; Co/MS-1 ·▬·; Co/MS-2 ··▬; Co/MS-3 ▬▬▬.
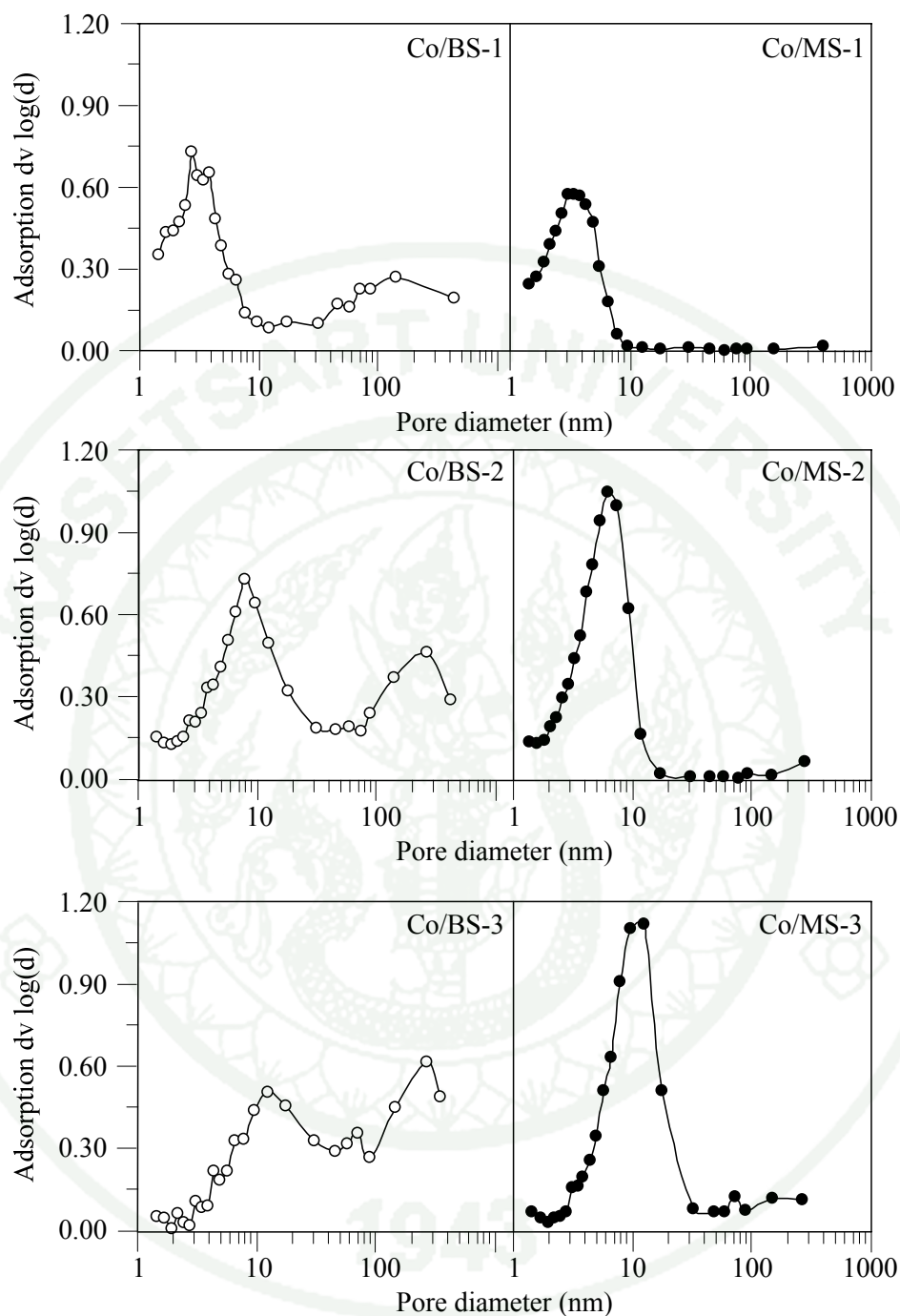
Figure 42 Pore size distribution of different types of catalysts.

After calcination process, the N_2-sorption technique was used to examine the pore structure of each catalyst. As shown in Figure 42, Co/BS-X catalysts showed the pore size distribution in two different length scales (mesopores and macropores). The

smaller pores had the mean pore diameters of 2.8, 7.7 and 12.1 nm, designated as Co/BS-1, Co/BS-2 and Co/BS-3 while the larger pores were in the range of 50-300 nm. The Co/MS-X catalysts with the same mesopore diameter of the Co/BS-X catalysts were used to investigate the effect of macropore. The sharp and narrow pore size distribution of both catalysts indicated their uniform pore structure of which can clearly indicate the relationship between the pore diameter and physicochemical properties of cobalt as the catalyst in FTS reaction.

The physical properties of the supports (BS-X and MS-X) and the cobalt catalysts (Co/BS-X and Co/MS-X) are listed in Table 4. It can be clearly seen that BET surface area of the supports was decreased with increasing mesopore diameter. After cobalt loading, the mesopore diameter was slightly decreased while the BET surface area and the pore volume were significantly decreased.

X-ray diffraction analysis was performed to investigate the types of cobalt species and average Co_3O_4 crystallite size. As shown in Figure 43, all catalysts mainly composed of Co_3O_4 spinel phase with 2θ values of 31.3, 36.9, 44.8, 59.4 and 65.3. The crystallite sizes of Co_3O_4 calculated using Scherrer equation were listed in Table 7. It was found that the Co_3O_4 crystallite size was increased with increasing the mesopore diameter. Similar trend was also reported by Song *et al.* (2006). However, the Co_3O_4 crystallite size of Co/BS-X catalysts was larger than that of Co/MS-X catalysts when compared at the same mesopore diameter. This could be due to broader pore size distribution and lower surface area of the BS-X supports (Figure 32, Figure 37, and Table 4).
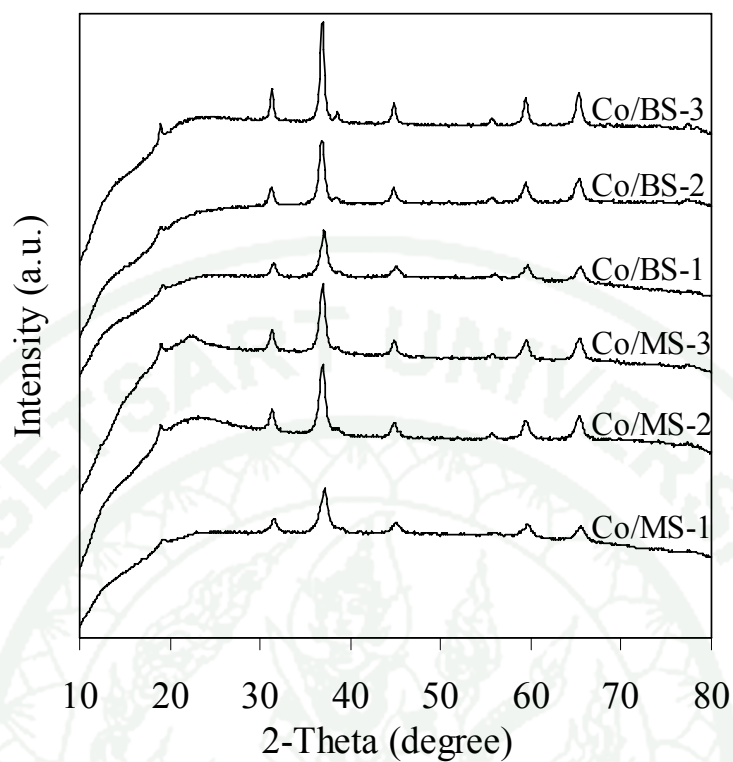
Figure 43 XRD patterns of calcined catalysts.

Table 7 Average Co_3O_4 crystallite diameter, and H_2 chemisorption of different catalysts

Catalysts	Co_3O_4 crystallite diameter [a] (nm)	H_2 adsorbed [b] (μmol/g)
Co/MS-1	8.7	122.2
Co/MS-2	13.4	151.0
Co/MS-3	14.9	130.7
Co/BS-1	9.5	108.6
Co/BS-2	14.6	132.4
Co/BS-3	20.6	88.2

[a] Mean diameter of Co_3O_4 crystallite determined by XRD (Scherrer equation).

[b] H_2 adsorbed determined by H_2 chemisorption technique.

TEM analysis was performed to investigate the shape and morphology of supports and the aggregates of Co_3O_4 crystal on supports. As shown in Figure 44, the darker spots (arrow 1) on the catalyst granules represented the areas of high concentration of Co_3O_4, whereas the other parts (arrow 2) indicated the silica support with minimal or no Co_3O_4 presented. It can be clearly seen that the structures of MS-X supports (Figures 44(a), (c), and (e)) and BS-X supports (Figures 44(b), (d) and (f)) were of great different. TEM images of MS-X supports represented isolated particles caused by the dense aggregation of silica nanoparticles, and therefore no macropores was observed. On the other hand, TEM images of BS-X supports exhibited the aggregation of silica clusters together with the open macropores (arrow 3). For all catalysts, Co_3O_4 aggregated in the form of semi-spherical clusters. The higher magnification images (Figure 44 (inset)) indicated that the Co_3O_4 crystallite size was increased with increasing the mesopore diameter.
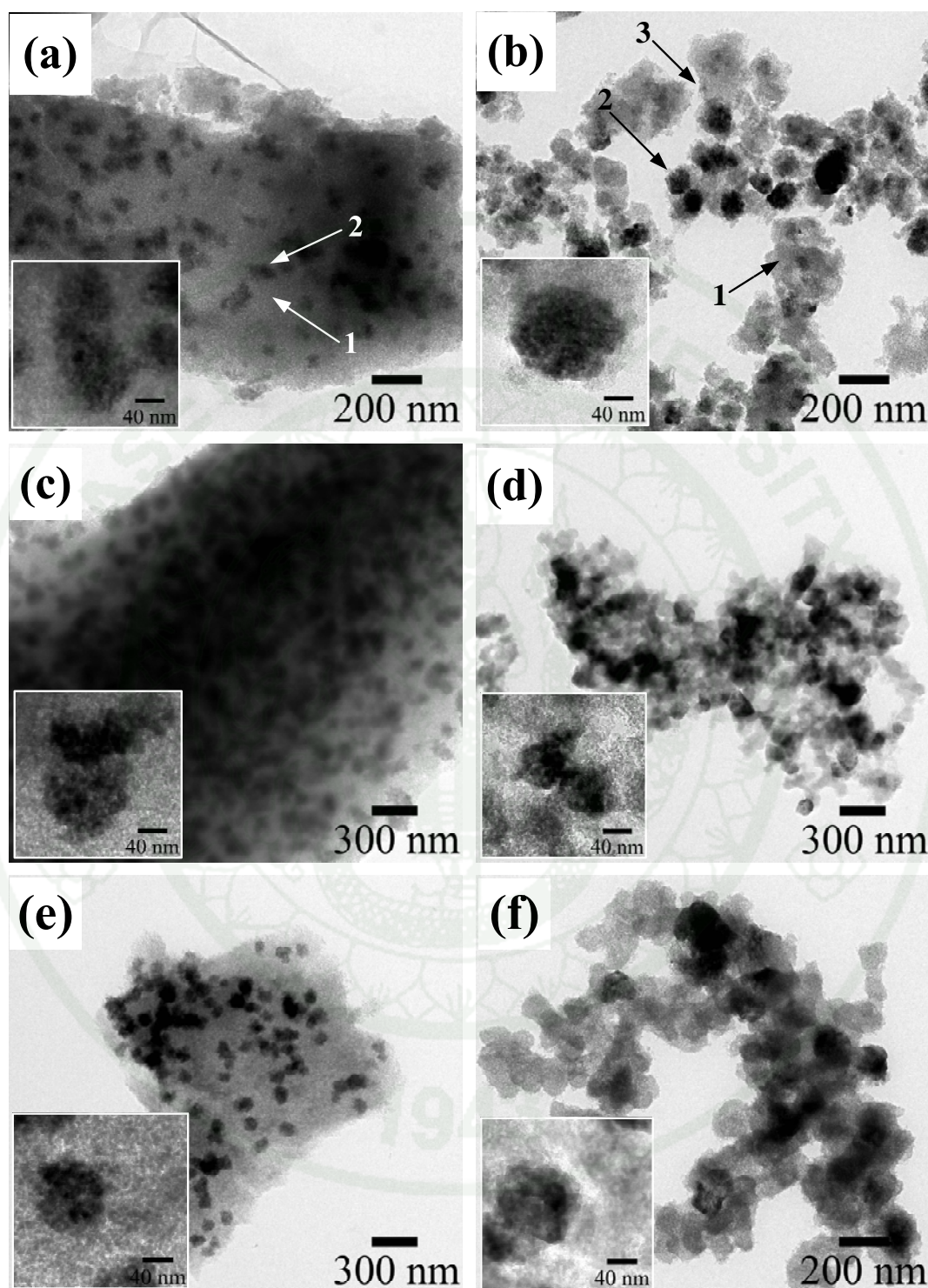
Figure 44 TEM micrographs of calcined catalysts: (a) CoMS-1; (b) CoBS-1; (c) CoMS-2; (d) CoBS-2; (e) CoMS-3; (f) CoBS-3.

As the active form of cobalt catalysts in FTS is cobalt metal (Co^0) (Steen *et. al.,* 1996), the reduction of cobalt oxide species obtained after calcination is essentially performed to obtain the active cobalt metal atom. It should be noted that the amount of H_2 adsorbed is related to the overall activity of the catalyst during carbon monoxide hydrogenation. The H_2 chemisorption results of all catalysts are shown in Table 7. When considering each series of catalysts, the catalysts with small mesopore diameter and large surface area (Co/MS-1 and Co/BS-1) showed the medium amount of H_2 adsorbed. In contrast, the catalysts with medium (Co/MS-2 and Co/BS-2) and large (Co/MS-3 and Co/BS-3) mesopore diameters displayed the highest and the lowest amount of H_2 adsorbed. These results could be explained that the addition of cobalt into mesoporous silica supports might cause the pore blocking. The cobalt species entrapped in the pore were not easily reducible, thus the amount of H_2 adsorbed of catalysts with small pore was lower than that of catalysts with medium pore. However, the lowest amount of H_2 adsorbed of catalysts with the large pore was due to the lowest number of cobalt active sites on surface of the catalysts. This was consistent with the results reported by Lapszewicz *et. al.* (1993) and Song *et al.* (2006). When compared between different series of catalysts at the same mesopore diameters, all Co/MS-X catalysts showed higher amount of chemisorbed H_2. This could be attributed to the higher surface area of MS-X supports (Table 4).

2. Fischer-Tropsch Synthesis (FTS) Reaction

Figure 45 shows the catalytic activity and C_{5+} selectivity as a function of time obtained from different types of cobalt-loaded catalysts. The activity and selectivity after 12 h of all catalysts are summarized in Table 8. The Co/MS-X catalysts (Figure 45(a)) shows high CO conversion within 8 h time on stream. After 8 h, the CO conversion was dramatically decreased, indicating the deactivation of catalysts. Similar trend was also observed with the C_{5+} selectivity (Figure 45(c)). The Co/MS-2 catalyst gave the highest CO conversion that might be attributed to the highest amount of cobalt active sites confirmed by the result of H_2 chemisorption. The low amount of C_{5+} selectivity indicated the evidence of hot spots formation on the catalysts surface. Comparing to the Co/MS-X catalysts, the Co/BS-X catalysts gave lower CO

conversion, however the conversion was almost constant over 12 h. Moreover, the C_{5+} selectivity obtained by Co/BS-X catalysts was quite high, indicating a well control of heat transfer during reaction.
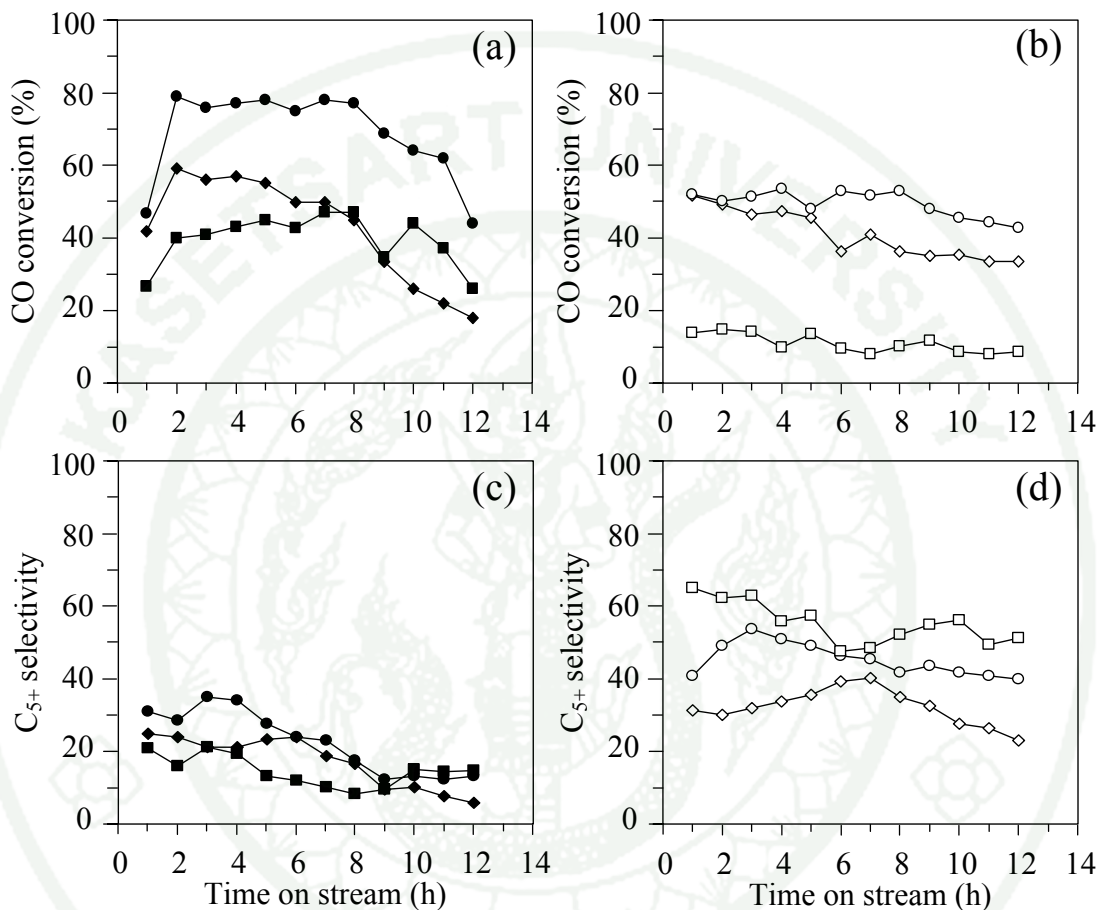

Figure 45 CO conversion (a and b) and C_{5+} selectivity (c and d) of different catalysts. (Co/MS-1: ◆; Co/MS-2: ●; Co/MS-3: ■; Co/BS-1: ◇; Co/BS-2: ○; Co/BS-3: □)

Table 8 The activity and selectivity after 12 h on stream of catalysts on Fischer-
Tropsch synthesis

Catalysts	CO conversion	CO_2 selectivity	Hydrocarbon selectivity (wt%)		
	(%)	(%)	CH_4	C_2-C_4	C_{5+}
Co/MS-1	26.2	17.1	69.0	24.5	6.5
Co/MS-2	44.5	9.2	48.9	36.5	14.6
Co/MS-3	18.3	4.4	47.1	36.9	16.0
Co/BS-1	36.6	3.4	40.6	34.0	25.4
Co/BS-2	47.4	1.4	18.4	37.6	44.0
Co/BS-3	9.6	0	13.3	30.5	56.2

The XRD patterns of the spent Co/MS-2 and Co/BS-2 catalysts, after 12 h
time on stream, are compared as shown in Figure 46. The XRD profile of Co/MS-2
catalyst exhibited the sharp diffraction at 2θ of 21.6 which was attributed to the
deposition of carbonaceous materials (Ohtsuka *et. al.*, 2004). The weak peak of CoO
which might be caused by the oxidation of Co metal to CoO after testing FTS was
also observed. In contrast, the peaks indicating the existence of carbonaceous
materials and CoO phase were not found for Co/BS-2 catalyst. The deposition of
carbonaceous materials was further investigated by TGA-DTA technique.
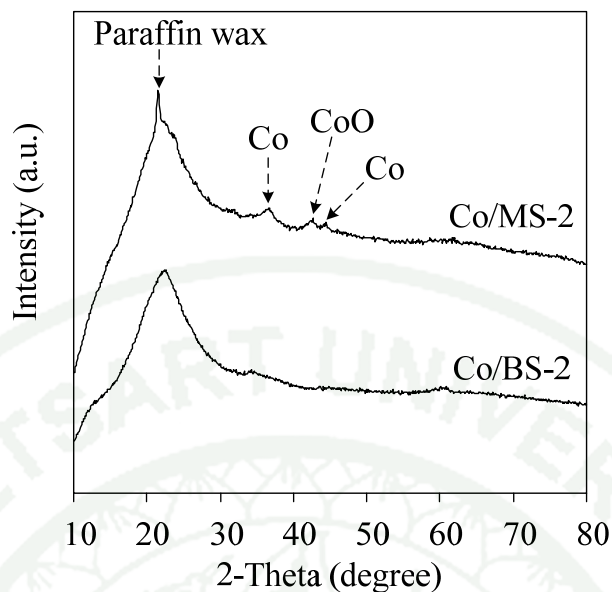
Figure 46 XRD patterns of the spent catalysts.

As shown in Figure 47(a), the spent catalysts displayed two steps of weight loss. The first step at the temperature below 150 ^{o}C was attributed to the evaporation of water molecules. The second step at the temperature above 150 ^{o}C was due to the combustion of carbonaceous materials confirmed by the exothermic peaks as shown in Figure 47(b). It can be clearly seen that the amount of carbon deposition of Co/MS-2 catalyst was higher than that of Co/BS-2 catalyst. This result was in good agreement with the XRD analysis as mentioned above.

Figure 47 TGA (a) and DTA (b) curves of the spent catalysts.

Once the heavy hydrocarbons and water formed in the pores of the catalyst, they should diffuse out from the pores to the bulk fluid and then the Co metal sites cou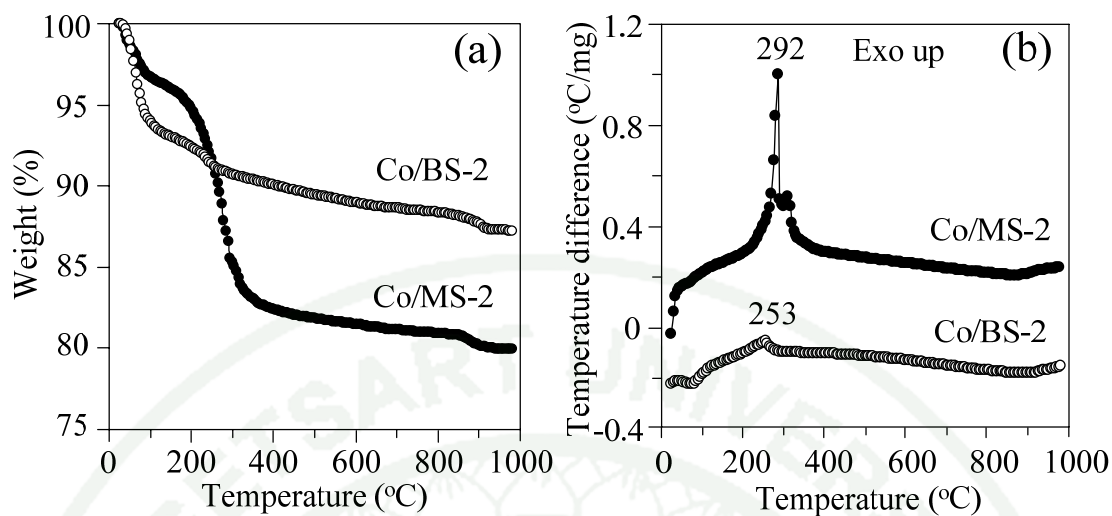ld be regenerated. However, the TEM images clearly indicated that the pore length of Co/MS-2 catalyst was quite long, and therefore the heavy hydrocarbons hardly removed and accumulated inside the pores of the catalysts. The pore blocking of heavy hydrocarbon not only reduced the available active surface but also hindered the activation by H_2 molecules. Moreover, the existence of water in the pores could cause the oxidation of cobalt metal to CoO phase observed by XRD spectroscopy (Figure 46). Compared to Co/MS-2 catalyst, the pore length of Co/BS-2 catalyst was significantly shorter, and therefore the heavy hydrocarbon and water could be easily diffuse from of the pores of the catalyst. As a result, the stability of CO conversion, the lower methane selectivity and the higher C_{5+} selectivity could be substantially obtained with Co/BS-2 catalyst.

CONCLUSION AND RECOMMENDATION

Conclusion

This research studied the synthesis of bimodal (meso-macro) porous silica using rice husk ash as the silica source and chitosan as the template. The studied variables were the pH of mixture, chitosan/silica ratio, and aging temperature. After that, the cobalt-loaded bimodal porous silica catalysts were prepared by the wetness impregnation method. The physicochemical characteristics and the catalytic properties for the Fischer-Tropsch synthesis (FTS) reaction were investigated. The obtained results were compared with the cobalt loaded monomodal porous silica catalysts. The results can be concluded as follows:

1. Bimodal porous silica can be successfully synthesized using rice husk ash as the low-cost silica source and chitosan as the template. The structure of bimodal porous silica composed of wormhole-like mesopore formed by the aggregate of primary silica nanoparticles and macropore obtained from the removal of chitosan template.

2. The mesopore diameter can be modified by tuning the pH of mixture and aging temperature. The variation of chitosan/silica ratio did not significantly affect the mesopore size. The chitosan macromolecules could control the size of silica clusters through the phase separation phenomena.

3. It was found that Co/MS-X catalysts were much more active than Co/BS-X catalysts but only within time limit due to the faster coke deposition caused by the longer pore length of monomodal porous silica supports. Moreover, water formation inside Co/MS-2 catalyst could possibly oxidize the cobalt catalyst from the active Co^0 to the inactive CoO.

Recommendation

Even though the results from this research have indicated new findings, the other issues related to this study should be further studied in detail. The recommendations regarding the further studies are given as follows:

1.   The phase separation phenomenon of chitosan-silica-water is firstly reported in this study, however, the obtained products structure were powders which were not suitable for some applications such as the column packing in HPLC or GC. Until now, many researchers have attempted to fabricate the monolith with meso-macro porosity using various kinds of expensive and considerably toxic organic compounds, therefore it is of great interest to synthesize the meso-macro porous silica monolith using chitosan as the template.

2.   The catalyst stability and selectivity for longer chain hydrocarbons were obtained by using novel bimodal porous silica as the support. However, only the effect of pore diameter has been studied. A large number of parameter affecting the activity and selectivity of Fischer-Tropsch synthesis reaction should be further investigated. Moreover, in order to prove that the utilization of the bimodal porous silica can improve the mass transfer limitations, the experiment should be performed to clarify the effect of bimodal porous material on these limitations.

3.   Due to the wide variety of beneficial property of bimodal porous silica including very high total pore volume and surface area, other potential applications should be considered and investigated.

LITERATURE CITED

Anal, A.K., A. Tobiassen, J. Flanagan and H. Singh. 2008. Preparation and characterization of nanoparticles formed by chitosan-caseinate interactions. **Colloids surf. B** 64: 104-110.

Ayers, M.R. and A.J. Hunt. 2001. Synthesis and properties of chitosan-silica hybrid aerogels. **J. Non-Cryst. Solids** 285: 123-127.

Berger, J., J.M. Mayer, O. Felt, N.A. Peppas and R. Gurny. 2004. Structure and interactions in covalently and ionically crosslinked chitosan hydrogels for biomedical applications. **Eur. J. Pharm. Biopharm**. 57: 19-34.

Brinker, C.J. and G.W. Scherer. 1990. **Sol-gel Science**. London, Academic press 581: 108-109.

Chanenchuk, C.A., I.C. Yates and C.N. Satterfield. 1991. The Fischer-Tropsch synthesis with a mechanical mixture of a cobalt catalyst and a copper-based water gas shift catalyst. **Energy and Fuels** 5: 847-855.

Chareonpanich, M., T. Namto, P. Kongkachuichay and J. Limtrakul. 2004. Synthesis of ZSM-5 zeolite from lignite fly ash and rice husk ash. **Fuel Proc. Tech.** 85: 1623-1634.

_____, A. Nanta-ngern and J. Limtrakul. 2007. Short-period synthesis of ordered mesoporous silica SBA-15 using ultrasonic technique. **Mater. Lett.** 61: 5153-5156.

Chin, R.L. and D.M. Hercules. 1982. Surface spectroscopic characterization of cobalt-alumina catalysts. **J. Phy. Chem.** 86: 360-367.

Coradin, T., O. Durupthy and J. Livage. 2002. Interactions of amino-containing
peptides with sodium silicate and colloidal silica: A biomimetic approach of
silicification. **Langmuir** 18: 2331-2336.

Davis, B.H. 2001. Fischer-Tropsch synthesis: current mechanism and futuristic
needs. **Fuel Proc. Tech.** 71: 157-166.

Della, V.P., I. Kuhn and D. Hotza. 2002. Rice husk ash as an alternate source for
active silica production. **Mater. Lett.** 57: 818-821.

Demadis, K.D., K. Pachis, A. Ketsetzi and A. Stathoulopoulou. 2009. Bioinspired
control of colloidal silica in vitro by dual polymeric assemblies of zwitterionic
phosphomethylated chitosan and polycations or polyanions. **Adv. Colloid
Interface Sci.** 151: 33-48.

Dry, M.E. 1990. The fischer-tropsch process - commercial aspects. **Catal. Today**
6: 183-206.

Ernst, B., S. Libs, P. Chaumette and A. Kiennemann. 1999. Preparation and
characterization of Fischer-Tropsch active Co/SiO2 catalysts. **Appl. Catal. A:
General**. 186: 145–168.

Flory, P.J. 1942. Themodynamics of high polymer solutions. **J. Chem. Phys.** 10:
51-61.

Gaube, J. and H.F. Klein. 2008. Studies on the reaction mechanism of the Fischer-
Tropsch synthesis on iron and cobalt. **J. Mol. Catal. A: Chem.** 283: 60-68.

Gregg, S.J. and K.S.W. Sing. 1982. **Adsorption, Surface Area and Porosity**, 2nd ed.
Academic Press, London.

Huggins, M.L. 1942. Some properties of solutions of long-chain compounds. **J. Phys. Chem**. 46: 151-158.

Hu, X., K. Littrel, S. Ji, D.G. Pickles and W.M. Jr Risen. 2001. Characterization of silica-polymer aerogel composites by small-angle neutron scattering and transmission electron microscopy. **J. Non-Cryst. Solids** 288: 184-190.

Kamiya, K., A. Oka, H. Nasu and T. Hashumoto. 2000. Comparative study of structure of silica gels from different sources. **J. Sol-Gel Sci. Technol.** 19: 495-499.

Kamath, S.R. and A. Proctor. 1998. Silica gel from rice hull ash: preparation and characterization. **Cereal Chem.** 75: 484-487.

Kim, Y.S., X.F. Guo and G.J. Kim. 2009. Asymmetric ring opening reaction of catalyst immobilized on silica monolith with bimodal meso/macroscopic pore structure. **Top. Catal.** 52: 197-204.

Lapszewicz, J.A., H.J. Loch and J.R. Chipperfield, 1993 The effect of catalyst porosity on methane selectivity in the Fischer-Tropsch reaction. **J. Chem. Soc., Chem. Commun.** 11: 913-914.

Luo, M. and B.H. Davis. 2003. Fischer–Tropsch synthesis: activation of low-alpha potassium promoted iron catalysts. **Fuel Proc. Tech.** 83 (1-3): 49-65.

Iglesia, E. 1997. Design, synthesis, and use of cobalt-based Fischer-Tropsch synthesis catalysts. **Appl. Catal. A: General** 161: 59-78.

Iler, R.K. 1979. **The Chemistry of Silica**. New York, Wiley.

Maitlis, P.M. 1989. A new view of the Fischer-Tropsch polymerization reaction.
    Pure & Appl. Chem. 61: 1747-1754.

Mansaray, K.G. and A.E. Ghaly. 1999. Determination of kinetic parameters of rice
    husks in oxygen using thermogravimetric analysis. **Biomass Bioenerg.** 17:
    19-31.

Nakanishi, K. 1997. Pore structure control of silica gels based on phase separation.
    J. Porous Mater. 4: 67-112.

_____. 2006. Sol-gel process of oxides accompanied by phase separation. **Bull.
    Chem. Soc. Japan.** 79: 673-691.

Nissinen, T., M. Leskelä, M. Gasik and J. Lamminen. 2005. Decomposition of mixed
    Mn and Co nitrates supported on carbon. **Thermochim. Acta** 427: 155-161.

Ohtsuka, Y., Y. Takahashi, M. Noguchi, T. Arai, S. Takasaki, N. Tsubouchi and Y.
    Wang. 2004. Novel utilization of mesoporous molecular sieves as supports of
    cobalt catalysts in Fischer-Tropsch synthesis. **Catal. Today** 89: 419-429.

Pedroni, V., P.C. Schulz, M.E. Gschaider de Ferreira and M.A. Morini. 2000. A
    chitosan-templated monolithic siliceous mesoporous-macroporous material.
    Colloid Polym. Sci. 278: 964-971.

Reuel, R.C. and C.H. Bartholomew. 1984. The Stoichiometries of H_2 and CO
    Adsorption on cobalt: Effect of Support and Preparation. **J. Catal.** 85: 63-77.

Retuert, J. R. Quijada, V. Arias and M.Y. Pedram. 2003. Porous silica derived from
    chitosan containing hybrid composites. **J. Mater. Res**. 18: 487-494.

Saib, A.M., M. Claeys and E.V. Steen. 2002. Silica supported cobalt Fischer-Tropsch
    catalysts: effect of pore diameter of support. **Catal. Today** 71: 395-402.

Song, D. and J. Li. 2006. Effect of catalyst pore size on the catalytic performance of silica supported cobalt Fischer-Tropsch catalysts. **J. Mol. Catal. A: Chem.** 247: 206- 212.

Stauffer, D., A. Conglio and M. Adam. 1982. **Advance in Polymer Science.** Heidelberg, Springer Verlag. 44: 139.

Steen, E.V., G.S. Sewell, R.A. Makhothe, C. Micklethwaite, H. Manstein, M. de Lange and C.T. O'Connor. 1996. TPR study on the preparation of impregnated Co/SiO$_2$ catalysts. **J. Catal.** 162: 220-229.

Takahashi, R., S. Sato, S. Tomiyama, T. Ohashi and N. Nakamura. 2007. Pore structure control in Ni/SiO$_2$ catalysts with both macropores and mesopores. **Micropor. Mesopor. Mater.** 98: 107-114.

Takeshita, T. and K. Yamaji. 2008. Important roles of Fischer-Tropsch synfuels in the global energy future. **Energy Policy** 36: 2773– 2784.

Tavasoli, A., M.G. Ahangari, C. Soni and A.K. Dalai. 2008. Cobalt supported on carbon nanotubes-A promising novel Fischer-Tropsch synthesis catalyst. **Fuel Proc. Tech.** 89: 491-498.

Tsubaki, N., Y. Zhang, S. Sun, H. Mori, Y. Yoneyama, X. Li and K. Fujimoto. 2001. A new method of bimodal support preparation and its application in Fischer-Tropsch synthesis. **Catal. Commun.** 2: 311.

Van Der Laan, G.P. and A. A. C. M. Beenackers. 1999. Kinetics and selectivity of the Fischer-Tropsch synthesis: A literature review. **Catal. Reviews** 41: 255– 318.

Vannice, M.A. 1977. The catalytic synthesis of hydrocarbons from H_2/CO mixtures
over the Group VIII metals V. The catalytic behavior of silica-supported
metals. **J. Catal.** 50: 228-236.

Wikipedia. 2007. **Polystyrene sulfonate**. Available Source:
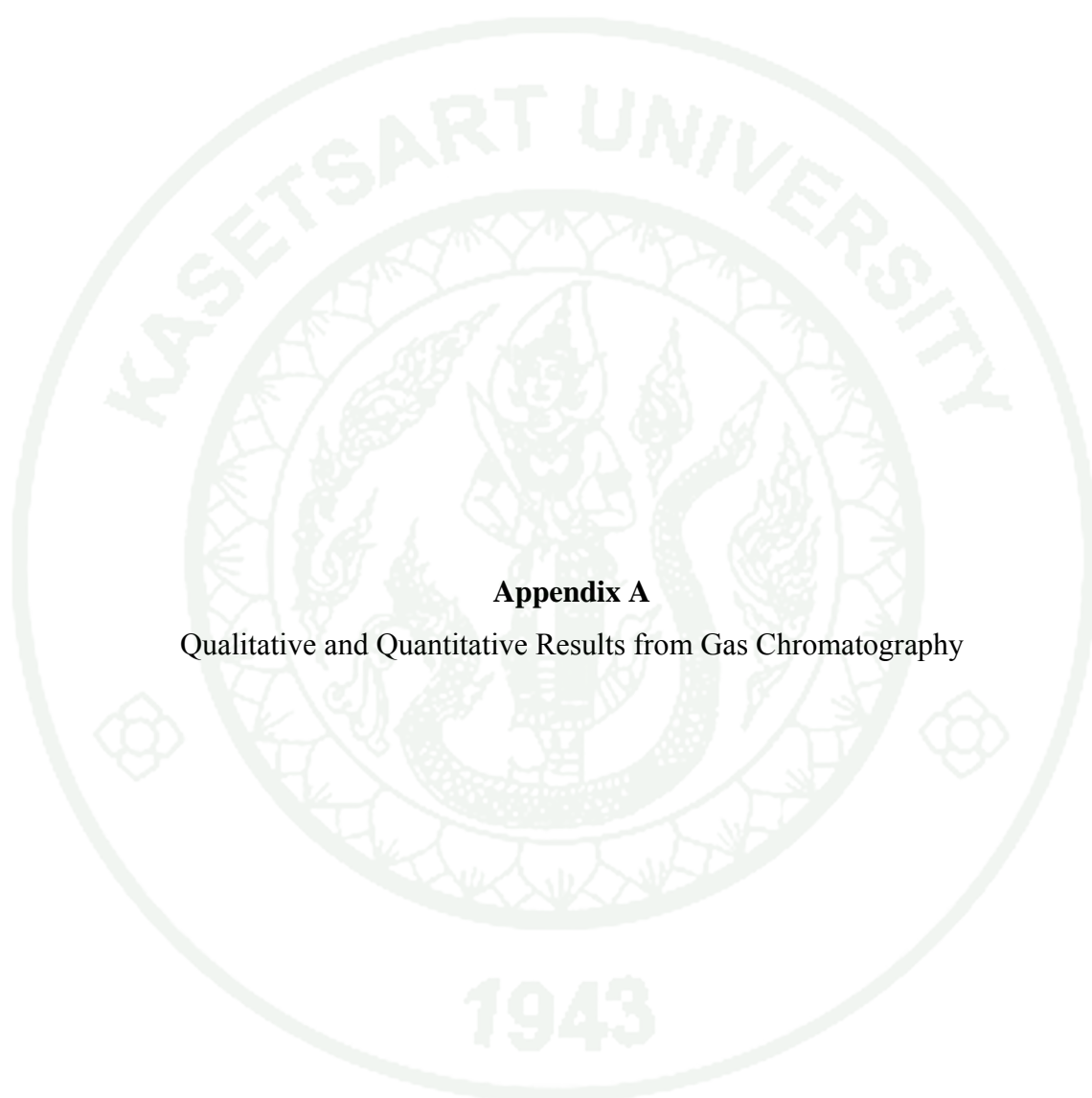http://en.wikipedia.org/wiki/File:Polystyrene_sulfonate.png, January 24, 2007.

_____. 2008. **Acrylic acid**. Available Source:
http://en.wikipedia.org/wiki/File:Acrylic-acid-2D-skeletal.png, November 12,
2008.

Zhang, C.H., Y. Yang, B.T. Teng, T.Z. Li, H.Y. Zheng, H.W. Xiang and Y.W. Li.
2006. Study of an iron-manganese Fischer–Tropsch synthesis catalyst
promoted with copper. **J. Catal.** 237: 405-415.

APPENDICES

Appendix A

Qualitative and Quantitative Results from Gas Chromatography

**Quantitative and Qualitative Results from Gas Chromatography**

Gas chromatography was performed in a specially designed instrument. The major instrumental components consisted of a flowing mobile phase, an injector port, a separation column containing the stationary phase, a detector, and a data recording system as shown in Appendix Figure A1. Certain amount of gaseous mixture, 0.5 mL in this research, was injected into gas chromatograph at the injector port and was volatilized in a hot injection chamber before it was transported to the head of the chromatic column. Then, a flow of inert carrier gas (as a mobile phase) swept the injected mixture through a heated column which contained the stationary phase. The gaseous sample moved along the packing column whereas its component gas moved with different flow rates and thus separated into pure component. Before each component exited the instrument, it passed through a detector. The detector sent an electronic signal to the recorder and the analyzed results were printed out.
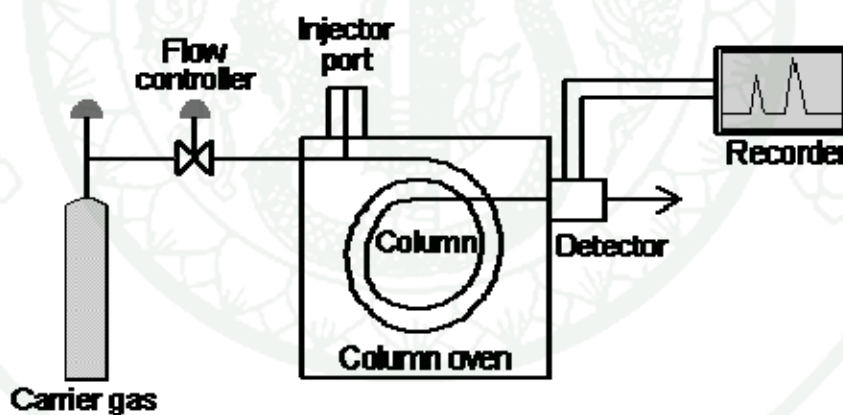

Appendix Figure A1 Schematic diagram of gas chromatograph.

In this work, the quantitative and qualitative data of product composition was obtained from 2 types of gas chromatography including TCD-GC and FID-GC as mention in the experimental chapter. Before analysis, the condition of operation was set and kept on running for about an hour to stabilize the based line. Certain volume of sample mixture (0.5 mL in this case) was injected into the injection port by gas syringe. After the mixture of sample gas was analyzed, the qualitative and

quantitative data were interpreted from the peak area obtained from the recorder. The component of injected gas mixture can be identified by using the value of retention time data compared with the retention time received from injected standard gas. The chromatogram of standard gases and liquids used in this research were shown as following figures:
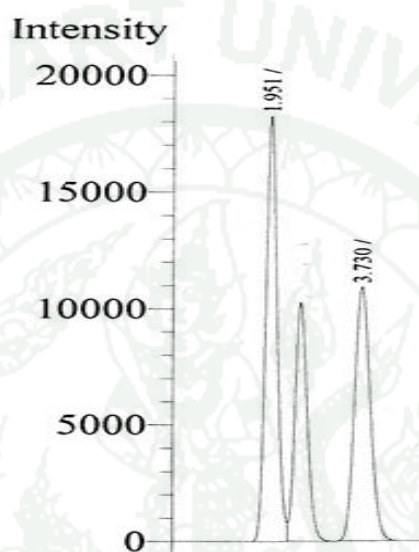
Appendix Figure A2 Chromatogram of standard gases for CO and CO_2.
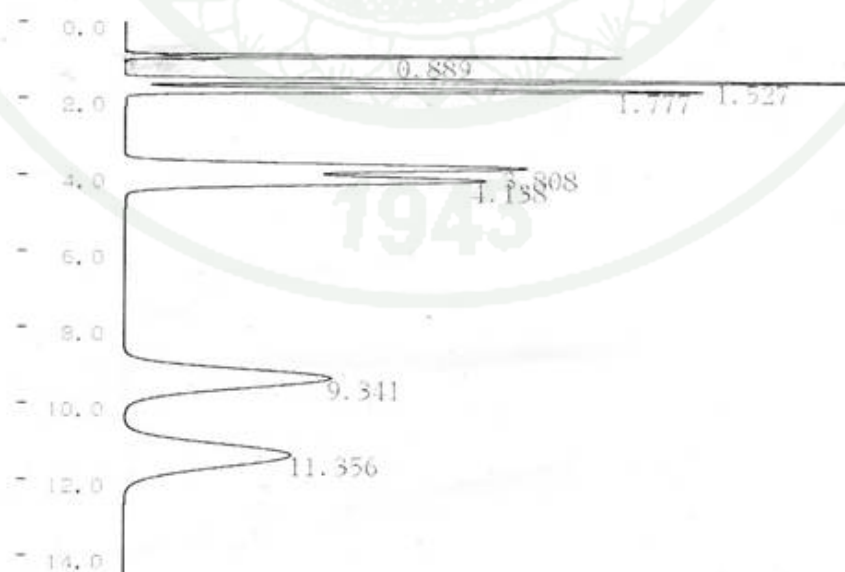
Appendix Figure A3 Chromatogram of standard gases for C_1-C_4 hydrocarbons.
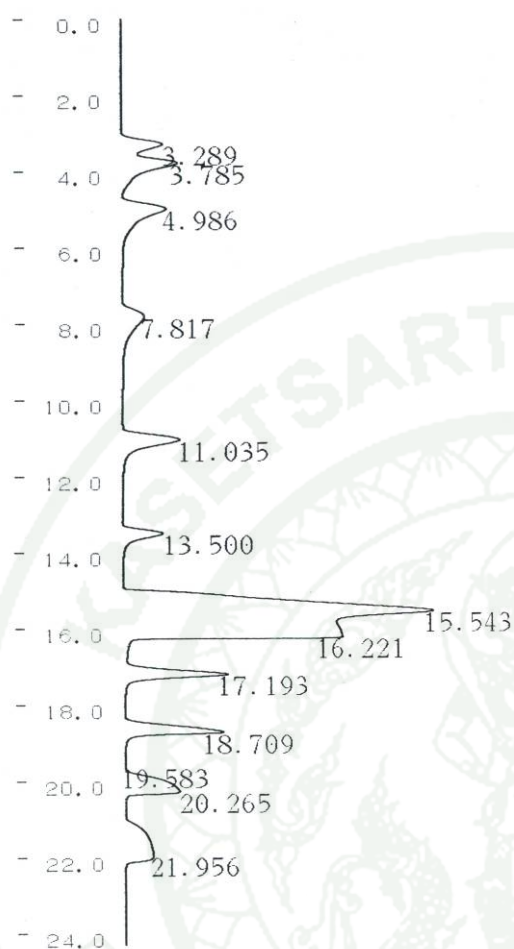
Appendix Figure A4 Chromatogram of standard liquids for C_5-C_{15} hydrocarbons.

The quantitative analysis of gas and liquid samples were obtained from the calibration curves where the correlation between the amount of injected gas or liquid sample (mole) and the peak area of gas chromatograms were proposed. The correlation between these parameters (mole and area) was analyzed by a linear regression equation. All the calibration curves for each single standard gas and liquid used in this research were shown in Appendix Table A1.

Appendix Table A1 Equation of calibration curves for standard gas and liquid

Substance	Equation	R^2
CO	mol = 4.46x 10^{-11} x area	0.999
CO_2	mol = 4.38 10^{-11} x area	0.999
CH_4	mol = 2.0x 10^{-12} x area	0.999
C_2H_4	mol = 6.75 x 10^{-13} x area	0.996
C_2H_6	mol = 6.78 x 10^{-13} x area	0.998
C_3H_6	mol = 4.43 x 10^{-13} x area	0.999
C_3H_8	mol = 4.34 x 10^{-13} x area	0.998
C_4H_{10}	mol = 3.08 x 10^{-13} x area	0.999
C_5H_{12}	mol = 3.05 x 10^{-13} x area	0.997
C_6H_{14}	mol = 1.39 x 10^{-13} x area	0.997
C_7H_{16}	mol = 1.39 x 10^{-13} x area	0.997
C_8H_{18}	mol = 1.97 x 10^{-13} x area	0.997
C_9H_{20}	mol = 1.13 x 10^{-13} x area	0.997
$C_{10}H_{22}$	mol = 1.97 x 10^{-13} x area	0.988
$C_{11}H_{24}$	mol = 7.36 x 10^{-14} x area	0.995
$C_{12}H_{26}$	mol = 6.85 x 10^{-14} x area	0.996
$C_{13}H_{28}$	mol = 6.67 x 10^{-14} x area	0.997
$C_{14}H_{30}$	mol = 6.15 x 10^{-14} x area	0.992
$C_{15}H_{32}$	mol = 6.25 x 10^{-14} x area	0.993

The calculation for the amount of each component in a standard-gas mixture can be calculated as follows:

$$\text{Amount of component}_i \text{ (mol)} = \frac{V_i \times T}{100 \times 22,400} \quad (A1)$$

where V_i = % volume of component$_i$ (cm^3/cm^3)

T = volume of standard gases mixture (mL)

The calculation for the amount of each component in a standard liquids mixture that can be calculated as follows:

$$\text{Amount of component}_i \text{ (mol)} = \frac{V_i \times T \times D \times P \times 10^{-3}}{MW} \qquad \text{(A2)}$$
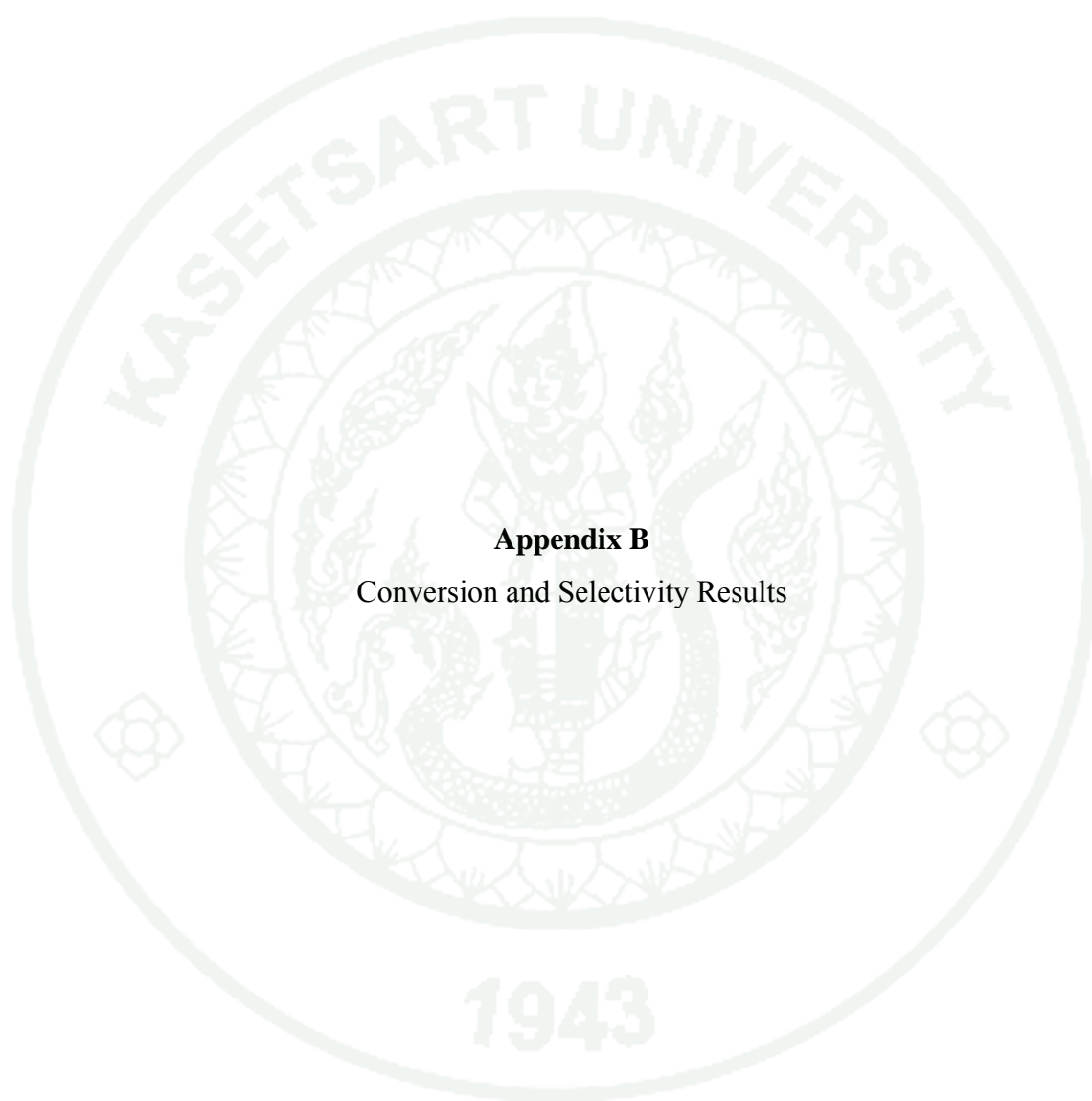
where V = % volume of component$_i$ (cm^3/cm^3)

T = volume of liquid mixture (μL)

D = density (g/cm^3)

P = purity (%)

MW = molecular weight (g/mol)

Appendix B

Conversion and Selectivity Results

Conversion and Selectivity Results

The calculation for the conversion of carbon monoxide to hydrocarbon products in Fischer-Tropsch synthesis (FTS) reaction are shown as follows:

Percent of CO conversion:

$$CO \text{ conversion } (\%) = (CO_{in} - CO_{out})/CO_{in} \times 100$$

Percent of effluent composition for FTS products:

$$\text{Effluent composition of product}_i (\%) = \frac{\text{Moles of product}_i \times 100}{\sum \text{Moles of FTS products}}$$

Percent of hydrocarbon selectivity for hydrocarbon products:

$$\text{Selectivity of hydrocarbon}_i (\%) = \frac{\text{Moles of hydrocarbon}_i \times 100 \times n_i}{(\sum \text{Moles of hydrocarbon products})}$$

where CO_{in} is a mole number of inlet carbon monoxide

CO_{out} is a mole number of outlet carbon monoxide

n_i is a number of carbon atoms in hydrocarbon$_i$

CIRRICULUM VITAE

NAME: Mr. Thongthai Witoon

DATE OF BIRTH: May 25, 1983

BIRTH PLACE: Chachoengsao, Thailand

EDUCATION:

YEAR	INSTITUTE	DEGREE
2005	Kasetsart Univ.	B.Eng. (Chemical Eng.) 1st Class honor
2010	Kasetsart Univ.	D.Eng. (Chemical Eng.)

AWARDS AND SCHOLARSHIPS

- October 2009 — The best presentation award from "the 19th Thai Institute of Chemical Engineering and Applied Chemistry"

- October 2007 — The best presentation award from "the 17th Thai Institute of Chemical Engineering and Applied Chemistry"

- July 2007 — The best presentation award from "the 2nd Workshop on the Utilization of Rice Husk and Rice Husk Silica"

- June 2005-Presnt — Royal Golden Jubilee Ph.D. Scholarship from Thailand Research Fund (TRF)

- June 2005-Presnt — The National Center of Excellence for Petroleum, Petrochemicals, and Advanced Materials, Kasetsart University.

INTERNATIONAL PUBLICATIONS

1.) **T. Witoon**, M. Chareonpanich, J. Limtrakul, *Synthesis of bimodal porous silica from rice husk ash via sol-gel process using chitosan as template*, Mater. Lett. 62 (2008) 1476.

2.) **T. Witoon**, M. Chareonpanich, J. Limtrakul, *Effect of acidity on the formation of silica-chitosan hybrid materials and thermal conductive property*, J. Sol-Gel Sci. Technol. 51 (2009) 146.

3.) O. Jullapan, **T. Witoon**, M. Chareonpanich, *Synthesis of mixed phase uniformly unfiltrated SBA-3-like in SBA-15 bimodal mesoporous silica from rice husk ash*, Mater. Lett. 63 (2009) 1303.

4.) **T. Witoon**, M. Chareonpanich, J. Limtrakul, *Effect of chitosan/silica ratio and aging temperature on pore structure of bimodal porous silica and fractal geometry*, in preparation.

5.) B. Chamnankid, **T. Witoon**, M. Chareonpanich, P. Kongkachuichay, J. Limtrakul, *Selective preparation of self-assembled core-shell and uniformly infiltrated mesoporous silica-aluminosilicate composites by using CTAB-chitosan templates,* in preparation.

6.) **T. Witoon**, M. Chareonpanich, J. Limtrakul, *Hierarchical macro-mesoporous silica as support for cobalt-based Fischer Tropsch synthesis*, in preparation.

INTERNATIONAL PROCEEDING

1.) **T. Witoon**, M. Chareonpanich, *Synthesis of mesoporous silica from rice husk ash using chitosan as template,* the 6th Asia Pacific Conference on Sustainable Energy and Environmental Technology (APCEET 2007), May 7-11, 2007.

2.) **T. Witoon**, M. Chareonpanich and J. Limtrakul, *Effect of pH on structural properties of mesoporous silica synthesized using chitosan as template*, the 2nd Workshop on the utilization of rice husk and rice husk silica, July 18, 2007.

3.) **T. Witoon**, M. Chareonpanich and J. Limtrakul, *Fabrication of bimodal porous silica with controllable pore size and structure using chitosan template*, the 6th Asian Aerosol Conference, November 24-27, 2009.